UNIVERSITY OF CALIFORNIA
RIVERSIDE

Magnesium-Based Bioresorbable Medical Implants: Improvement to Standardization

A Dissertation submitted in partial satisfaction
of the requirements for the degree of

Doctor of Philosophy

in

Bioengineering

by

Qiaomu Tian

March 2017

Dissertation Committee:
Dr. Huinan Liu, Chairperson
Dr. Masaru Rao
Dr. Yadong Yin

The Dissertation of Qiaomu Tian is approved:

_____

_____

_____

Committee Chairperson

University of California, Riverside

ACKNOWLEDGEMENTS

I would like to thank Dr. Liu and Liu lab for all these years of advice and support. I acknowledge the significant contributions from the talent and dedicated undergrad researchers (Michael Deo, Laura Rivera-Castaneda, Zachary Dunn, Amit Tsanhani, Neema Masoudipour, Alexis Rodriguez, Jose Mendez, and Rebekah Pittman). I would like to thank the Central Facility for Advanced Microscopy and Microanalysis for the use of SEM and EDS at the UC-Riverside. I acknowledge Dr. Ilkeun Lee and a U.S. National Science Foundation grant (DMR-0958796) for the XPS characterization, Winston Chung Global Energy Center for the use of XRD, Dr. Dan Borchardt at Analytical Chemistry Instrumentation Facility (ACIF) for the use of FTIR.

I would also thank our funding agencies: U.S.A. NSF BRIGE award (CBET 1125801), Burroughs Wellcome Fund (1011235), Hellman Faculty Fellowship, National Institutes of Health /National Institute of Dental and Craniofacial Research (R43DE023287-02), U.S. National Science Foundation (NSF award CBET 1512764), UC-Riverside Graduate Dean's Dissertation Research Grant, UC Leadership Excellence through Advanced Degrees Program, UC-Riverside Mentoring Summer Research Internship Program, UC-Riverside Research in Science and Engineering Program, and Hispanic Serving Institution Undergraduate Research Program (P031C110131) for financial support.

I would thank the American Chemical Society, World Scientific Publishing, and Institute of Physics Journals for the permission of reprinting my previous publications. Specifically, reprinted with permission from {Tian, Q.; Deo, M.; Rivera-Castaneda, L.; Liu, H., Cytocompatibility of Magnesium Alloys with Human Urothelial Cells: A Comparison of

Three Culture Methodologies}. Copyright {2016} American Chemical Society." Reprinted with permission from {Tian, Q.; Rivera-Castaneda, L.; Dunn, Z. S.; Liu, H., Bioceramics for Orthopaedic Device Applications: Hydroxyapatite}. Copyright {2017} World Scientific Publishing." Reprinted with permission from {Tian, Q.; Liu, H., Electrophoretic deposition and characterization of nanocomposites and nanoparticles on magnesium substrates}. Copyright {2015} IOP Publishing."

ABSTRACT OF THE DISSERTATION

Magnesium-Based Bioresorbable Medical Implants: Improvement to Standardization

by

Qiaomu Tian

Doctor of Philosophy, Graduate Program in Bioengineering
University of California, Riverside, March 2017
Dr. Huinan Liu, Chairperson

Medical implants are devices that are often placed inside the human body to provide support to organs and tissues. Magnesium (Mg) shows great potentials as bioresorbable medical implants. Specifically, Mg is cytocompatible with many human cells *in vitro* and *in vivo*. Mg naturally degrades in the human body, which eliminates the secondary removal procedure of the implant. The primary degradation product, Mg ions, is an essential element which participates in over 300 enzymatic metabolisms. As a light metal, Mg possesses an adequate mechanical strength, even for the load-bearing condition in orthopedic device applications.

We conducted concentration-dependent tests of Mg degradation products, i.e., Mg ions, OH^- ions, MgO and $Mg(OH)_2$, with representative cell models. For human urothelial cells, pH of 8.6 showed cytotoxicity, and Mg ions of 10 mM showed a decrease in cell proliferation rate. We investigated three major strategies to improve Mg, that is, surface-coating, alloying and composite. A bioactive, protective surface coating will control degradation rate, and possibly induce a positive tissue response to Mg. Alloying of Mg with other metal elements can potentially result in alloys with improved corrosion

resistance and mechanical strength. Sintering Mg powders with calcium phosphates could result in Mg composite with lower degradation rate.

In an attempt to establish the consensus standard of the testing Mg-based implant, we design three different *in vitro* culture methodologies to mimic different *in vivo* cell-biomaterial interactions. Direct culture is suitable *in vitro* method when it is important to evaluate direct cell attachment on the biomaterial surfaces. Direct exposure culture is desirable *in vitro* method for investigating the response of well-established cells in the body with newly implanted biomaterials. Exposure culture method is appropriate for evaluating cell-biomaterial interactions in the same environment, where they are not in direct contact. Due to the continuous degradation of Mg, cells that were direct contact or indirect contact with Mg substrates, both responded differently to different culture methodologies. A loading apparatus that we designed indicated that Mg under load had a significantly faster degradation rate. Thus, future evaluation of Mg should also take specific loads of different applications into account.

Table of contents

Figures

Table

Chapter 1 Potentials and Risk of Magnesium for Medical Implant Applications

Magnesium (Mg) shows attractive biodegradability as temporary medical implants for urological, musculoskeletal, and dental device applications[1-5]. In urological device applications, a ureteral stent is often used to open up the ureter for relieving the obstruction between the bladder and kidneys, which caused by diseases include kidney stones and malignancies[6-8]. Current commercial available materials for ureteral stents are non-degradable polymers or metals, such as polyurethane and chromium cobalt, which are relative inert to the physiological environment[8]. Unfortunately, urinary tract infection caused by bacterial adhesion and blockage caused by encrustation remain as problems associated with these permanent materials[9-10]. Additionally for non-biodegradable stents, a secondary procedure is typically required to remove a ureteral stent after the treatment. With encrustation and infection, the increased difficulties in stent removal can add extra cost and morbidity to the patient. Therefore, to overcome these limitations, attempts have been made to develop biodegradable ureteral stents[11]. For example, biodegradable polyesters, such as poly (lactic-co-glycolic acid), have been investigated for ureteral stent applications[12]. However, poly (lactic) and poly (glycolic) based stents did not show any advantages in preventing bacterial adhesion comparing with the current material[13]. Bacterial attachment and biofilm formation on the surface of these stents can still cause major problems for the patients.

Therefore, an ideal material for ureteral stents can be proposed: the material should be able to reduce bacterial infection while being safely biodegradable in the physiological

environment. The degradability of Mg in aqueous physiological environment is promising for urological device applications, such as urological stents and catheters. The main degradation product of Mg, i.e. magnesium ions (Mg^{2+})[14-15], is an essential and abundant element in human body, which participates in over 300 enzymatic metabolisms. More importantly, Mg and its alloys also demonstrated antibacterial properties[16-17]. Lock *et al.* demonstrated the antibacterial property of Mg alloys in artificial urine solution, supporting Mg alloys as promising materials for ureteral stent applications[16].

In musculoskeletal application, fixation devices, such as plates, screws, and pins, are widely used for stabilizing bone fractures and are currently made out of permanent metals, such as titanium-based alloys. However, these fixation devices are only needed temporarily in the body, and permanent metals often require surgical removal after bone heals[18]. Mg is promising for temporary implant applications as aforementioned. Moreover, Mg-based metallic materials provide similar elastic modulus and yield strength, i.e., 40 GPa and 126 MPa respectively, as those of natural cortical bone (3–20 GPa and 104.9–114.3 MPa respectively)[19]. Thusly, Mg-based implants reduce the detrimental effects of stress-shielding while providing necessary strength for bearing load[20]. As a matter of fact, Mg^{2+} ion concentration in cartilage and bone tissue is high at the initial stage of osteogenesis. Mg^{2+} ions are important for bone cell functions and inducing new bone formation[21].

Unfortunately, rapid degradation rate of Mg-based implants in a physiological environment still limit them from broadening applications[22]. Rapid degradation of Mg causes pH increase in the local environment and produces excess H_2 gas, which has

unfavorable effects on local cell and tissue functions. Moreover, rapid degradation of Mg may cause implant failure if the implants lose their mechanical stability before the tissue heals. Therefore, it is essential to fully evaluate the degradation products and degradation behavior of Mg *in vitro* before bring it to future animal study and clinical trials. It is also critical to develop efficient strategies to control Mg degradation (or corrosion) rate for medical device applications[23-25].

Chapter 2 Cytotoxicity of Soluble Magnesium Degradation Products

1. Introduction

For ureteral stent applications, human urothelial cells (HUCs) are highly relevant as an *in vitro* cell model for studying cytocompatibility of Mg degradation products. HUCs grow on the inner surface of the ureter, which is the place for implantation of the ureteral stent in the human urological system. They maintain impermeability to urinary solutes to protect underlying tissues and cells from the caustic effects of urine. They also serve as a barrier to prevent adhesion of pathogenic bacteria or fungi[6, 26]. We cultured HUCs in the media with different initial pH, i.e., different OH^- ion concentration, and different initial Mg^{2+} ion concentration, to investigate the cytotoxicity of the main soluble degradation products of Mg.

2. Materials and Methods

2.1 The Effects of Alkaline pH on the HUCs

To evaluate the effects of elevated pH on HUCs, the initial pH of the culture media was adjusted to 7.7, 8.0, 8.3, 8.6, 9.0, 9.5 and 10.0 by adding the respective amount of sterilized sodium hydroxide (NaOH) solution. Specifically, HUCs were first cultured in the normal HUC media with a pH of 7.4 until a cell layer was well established. Afterwards, the normal HUC media was replaced with the media with adjusted pH of 7.7, 8.0, 8.3, 8.6, 9.0, 9.5 and 10.0, respectively, and then incubated for 24 hours under the standard cell culture condition. After 24 hours of culture in the media with adjusted initial pH, HUCs were fixed and stained for fluorescence imaging. HUC adhesion density and morphology were then characterized using the same method as described previously. As a reference,

HUCs were also cultured in the normal media with a pH of 7.4, i.e., the standard pH of the culture media, which was referred to as “Cells”.

2.2 The Effects of Mg^{2+} Ion Concentration on the HUCs

To investigate the effects of elevated Mg^{2+} ion concentration on HUCs, the Mg^{2+} ion concentration in the culture media was adjusted to 2 mM, 5 mM, 10 mM, 15 mM, 20 mM, 30 mM and 40 mM, respectively, by adding the respective amount of sterilized stock magnesium chloride ($MgCl_2$) solution. Specifically, a $MgCl_2$ stock solution was prepared with DI water to reach a concentration of 100 mM. The respective amount of $MgCl_2$ stock solution was mixed with the normal HUC media to produce the desired media with Mg^{2+} ion concentrations of 2 mM, 5 mM, 10 mM, 15 mM, 20 mM, 30 mM and 40 mM. HUCs were first cultured in the normal HUC media with a Mg^{2+} ion concentration of 0.6 mM, i.e., the standard Mg^{2+} ion concentration of the HUC media, until a cell layer was well established. Afterwards, the normal HUC media was replaced with the media with adjusted Mg^{2+} ion concentrations at 2-40 mM, respectively, and then incubated for 24 hours under the standard cell culture condition. After 24 hours of culture in the media with adjusted initial Mg^{2+} ion concentrations, HUCs were fixed and stained for fluorescence imaging. HUC adhesion density and morphology were then characterized using the same method as described previously. As a reference, HUCs were also cultured in the normal media with a Mg^{2+} ion concentration of 0.6 mM, which was referred to as “Cells”.

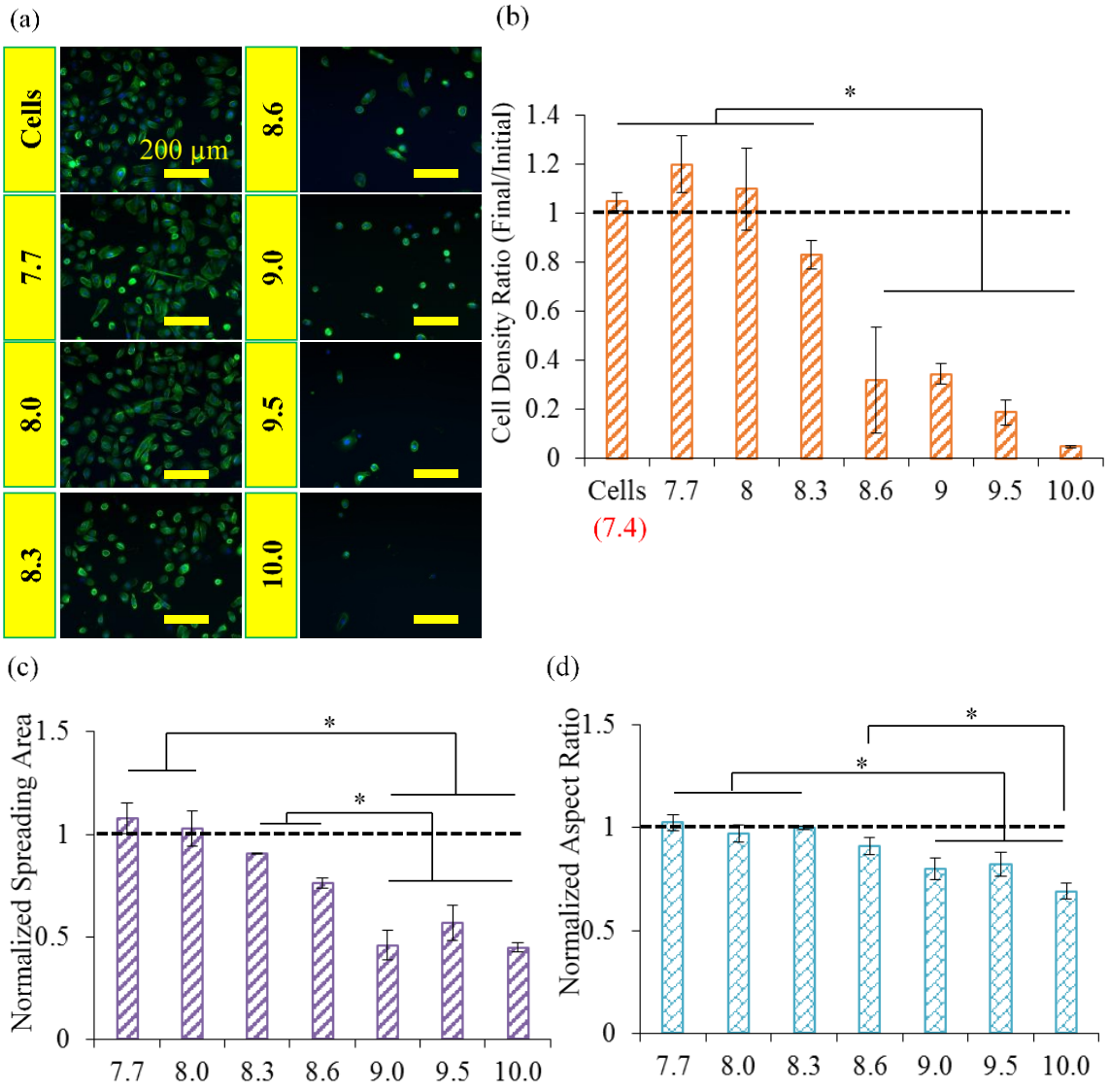

Figure 1: HUC behaviors after 24 hours of incubation in media with initial pH values adjusted to be at 7.7 - 10. (a) Representative fluorescence images of HUCs. Blue color indicates DAPI-stained nuclei and green color indicates Alexa Fluor® 488-stained F-actin (cytoskeleton). Scale bar = 200 µm for all images. Original magnification: 100×. (b) Average density ratio of adhered HUCs on culture plates. (c) Normalized spreading area of adhered HUCs. Average spreading area of adhered HUCs in the cultures with adjusted initial pH was normalized by the cells only control group. (d) Normalized aspect ratio (Dmax/Dmin) of adhered HUCs. Average aspect ratio of adhered HUCs in the cultures with adjusted initial pH was normalized by the cells only control group. Data are mean ± standard deviation (N=3); *p<0.05.

3. Results

3.1 Effects of Alkaline pH on the HUC Adhesion Density and Morphology

The HUCs cultured in the media with an initial pH of 7.4 (cells control), 7.7 and 8.0 showed healthy morphology after 24 hours; and starting from the pH of 8.3, the HUCs appeared to be unhealthy with a round morphology, as shown in Figure 1a. The cell density ratio (Final/Initial) showed statistically significant difference when HUCs were cultured for 24 hours in the media with the initial pH adjusted to be at 7.4 (cells control), and 7.7-10.0 [$F(7,16)=47.97$, $p<0.05$], as shown in Figure 1b. The average cell density ratio started to decrease to be less than 1 in the media with an initial pH of 8.3, but not statistically significant; when the initial pH of media increased to 8.6, the cell density significantly reduced. The average cell density ratios after cultured in the media with an initial pH of 7.4, 7.7, 8.0 and 8.3 were statistically greater than those of 8.6, 9.0, 9.5 and 10.0.

The normalized spreading area of HUCs showed statistically significant difference after being cultured in the media with adjusted initial pH values [$F(6,14)=41.31$, $p<0.0001$], as shown in Figure 1c. The spreading areas of HUCs cultured in the media with an initial pH adjusted to 7.7 and 8.0 were found to be statistically greater than that of 9.0, 9.5 and 10.0. Starting at the pH of 8.3, the average spreading area of HUCs started to decrease, but not statistically significant until the pH was adjusted to 9.0 and above. Statistically significant difference was also detected between the pH groups of 8.3, 8.6 and the groups of 9.0, 9.5, and 10.0. The normalized aspect ratio of HUCs showed statistically significant difference after being cultured in the media with adjusted initial pH values [$F(6,14)=23.14$, $p<0.0001$], as indicated in Figure 1d. The aspect ratio of HUCs cultured in the media with

an initial pH adjusted to 7.7, 8.0 and 8.3 were found to be statistically higher than that of 9.0, 9.5 and 10.0. Starting at the pH of 8.6, the average aspect ratio of HUCs started to decrease, but not statistically significant until the pH was adjusted to 9.0 and above. Statistically significant difference was also detected between the pH groups of 8.6 and 10.0.

3.2 Effects of Mg^{2+} Ion Concentration on the HUC Adhesion Density and Morphology

The HUCs cultured in the media with increasing concentrations of Mg^{2+} ions showed larger spreading area but no significant change in shape, as shown in Figure 2a. The cell density ratios showed statistically significant difference when HUCs were cultured for 24 hours in the media with the initial concentrations of Mg^{2+} ions adjusted to be at 2 mM to 40 mM [$F(7,16)=10.77$, $p<0.0001$], as shown in Figure 2b. The cell density increased for the groups of cells only control (0.6 mM), 2 mM, and 5 mM, while the rest of the groups showed similar cell density as the initial. HUC density in the groups of cells only control and 2 mM was found to be statistically significant higher than the groups of 10 mM, 15 mM, 20 mM, 30 mM and 40 mM after 24 hours of culture.

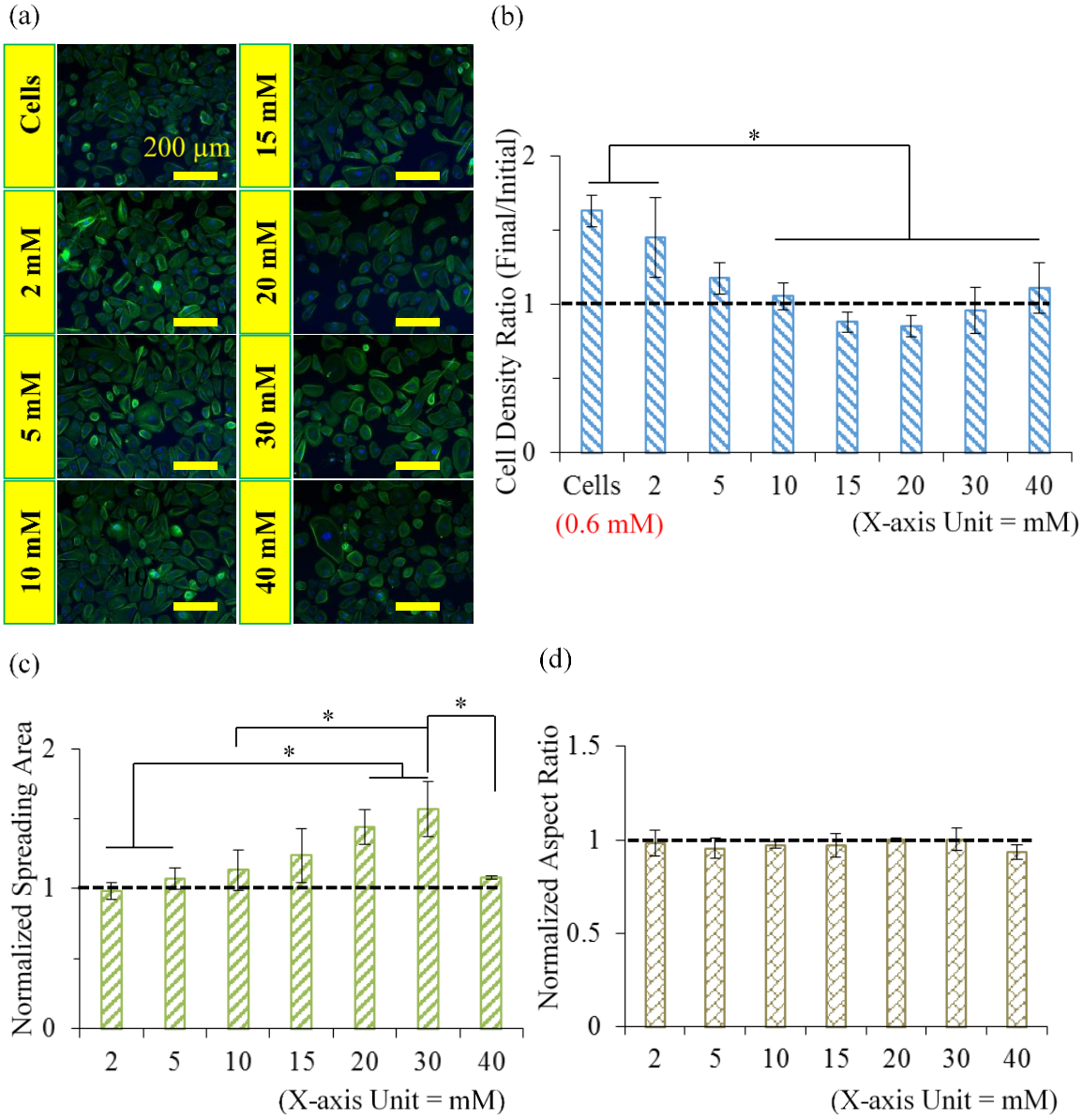

Figure 2: HUC behaviors after 24 hours of incubation in media with initial Mg^{2+} ion concentration adjusted to be at 2 mM to 40 mM. (a) Representative fluorescence images of HUCs. Blue color indicates DAPI-stained nuclei and green color indicates Alexa Fluor® 488-stained F-actin (cytoskeleton). Scale bar = 200 μm for all images. Original magnification: 100×. (b) Average density ratio of adhered HUCs on culture plates. (c) Normalized spreading area of adhered HUCs. Average spreading area of adhered HUCs in the cultures with adjusted initial Mg^{2+} ion concentration was normalized by the cells only control group. (d) Normalized aspect ratio (D_{max}/D_{min}) of adhered HUCs. Average aspect ratio of adhered HUCs in the cultures with adjusted initial Mg^{2+} ion concentration was normalized by the cells only control group. Data are mean ± standard deviation (N=3); *p<0.05.

The normalized spreading area of HUCs showed statistically significant difference after being cultured in the media with adjusted initial Mg^{2+} ion concentrations

[F(6,14)=8.04, p=0.0002], as shown in Figure 2c. The spreading areas of HUCs cultured in the adjusted media groups of 20 mM and 30 mM were found to be statistically larger than the groups of 2 mM and 5 mM; and the spreading area of HUCs cultured in the adjusted media group of 30 mM was greater than the groups of 10 mM and 40 mM. The normalized aspect ratio of HUCs showed no statistically significant difference after being cultured in the media with adjusted initial Mg^{2+} ion concentrations, as shown in Figure 2d. Although not statistically significant, the HUCs cultured in the adjusted media group of 40 mM showed a lower aspect ratio in average than the other groups after 24 hours of culture.

4. Discussion

We found that the average HUC density decreased to 80% of initial density at pH of 8.3. As the pH increased to be 8.6 and above, the average HUC density decreased to about 40% or less (Figure 1). In terms of HUC morphology, the average spreading area and aspect ratio of HUCs decreased as the pH increased, and showed statistically significant reduction when the pH was 9.0 and above. The reduced cell spreading area, and the round-shape of cells indicated that HUCs were unhealthy. In contrast, the average HUC density increased as compared to the initial density after exposure to the media with increased Mg^{2+} ion concentration of 2-10 mM (Figure 2). When the concentration of Mg^{2+} ions increased to be greater than 10 mM, the HUC density were similar as the initial density, indicating lack of cell proliferation after 24 hours of culture. Excessive Mg^{2+} ions can elicit depolarization of cell membrane. Significant effects of Mg^{2+} ions were observed on smooth muscle cells at 8 mM, and endothelial placental vessel cells at 6 mM[27]. Knedler et al. reported that the optimal concentration of Mg^{2+} ions for human microvascular endothelial

cells was from 8 mM to 10 mM, and the cell growth decreased when the Mg^{2+} ion concentration was over 10 mM[28].

In a summary, soluble degradation products of Mg-based materials reduced HUC density significantly when the pH increased to 8.6 and above or the Mg^{2+} ion concentration reached 10 mM and above.

Chapter 3 Cytotoxicity of Insoluble Magnesium Degradation Products

1. Introduction

When Mg degrades, nanostructured MgO and $Mg(OH)_2$ form on the surface of Mg from the chemical reactions between the Mg and the surrounding fluid[29-30]. Although the dissociation of MgO and $Mg(OH)_2$ from the Mg substrate are limited reported, the surrounding tissue and cells are still in direct contact with them *in vivo*. We cultured HUCs in the media with different initial MgO and $Mg(OH)_2$ concentration to investigate the cytotoxicity of the main insoluble degradation products of Mg.

2. Materials and Methods

The effect of different concentrations of magnesium oxide (MgO) particles and magnesium hydroxide [$Mg(OH)_2$] particles on HUCs was examined. Before the study, the MgO particles were baked at 200 ºC, while the $Mg(OH)_2$ particles were baked at 120 ºC for 2 hours to remove water or moisture. Different masses of MgO and $Mg(OH)_2$ were weighed and stored in a 0.6 mL conical tube, and then 4 mL of media was used to wash them out and added into the well plate to obtain concentration of 0.2 mg/mL, 0.3 mg/mL, 0.5 mg/mL, 0.7 mg/mL, 1 mg/mL, 1.2 mg/mL, 1.6 mg/mL and 2 mg/mL of either particle. HUCs were cultured with MgO and $Mg(OH)_2$ particles of different concentration for 24 hours. The cell reference consisted of media with no particles was referred to as “Cells”. Blank media with no cells and particles was also included as “Media”. The fluorescence images of adhered HUCs, pH values and Mg^{2+} ion concentration of the media was collected as described previously. Then, the concentrations of which cells showed viability, were selected and cultured for 48 hours to investigate possible adverse effect under a longer

exposure. For 48 hours study of particles, the fluorescence images as well as pH values and the Mg^{2+} ion concentration were recorded as well.

The dissociation of MgO and $Mg(OH)_2$ particles into Mg^{2+} ions in 24-hour culture, was calculated based on the obtained Mg^{2+} ion concentration. Specifically, the Mg^{2+} ion concentration in the Media group ($C_{i,\ media}$), i.e., the baseline Mg^{2+} ion concentration, was subtracted from the Mg^{2+} ion concentration measured in the MgO and $Mg(OH)_2$ groups ($C_{i,\ particle}$) to obtain the actual concentration of Mg^{2+} ions dissociated from the MgO and $Mg(OH)_2$ nanoparticles ($C_{f,\ dis}$), i.e., $C_{f,\ dis}=C_{i,\ particle}-C_{i,\ media}$. At each initial concentration (C_0), the dissociation of MgO and $Mg(OH)_2$ particles into Mg^{2+} ions (D) in HUC culture was calculated as $D= (C_{f,\ dis})/(C_0)$.

3. Results

3.1 HUC Behaviors after a 24-hour Culture with MgO or $Mg(OH)_2$ Particles

After culture with different concentrations of MgO or $Mg(OH)_2$ nanoparticles for 24 hours, HUCs showed normal cell morphology with 0.2 mg/mL and 0.3 mg/mL of MgO or $Mg(OH)_2$ when compared to the cells only reference as indicated in Figure 3a. From 0.5 mg/mL, the size of HUCs started to reduce, and more cells showed bright round morphology. Cell numbers decreased at 0.5 mg/mL and 0.7 mg/mL, and no viable cells were observed at 1.0 mg/mL, 1.2 mg/mL, 1.6 mg/mL and 2.0 mg/mL.

Statistically significant differences in HUC density were found after cultured with MgO [$F(8,18)=40.68$, $p<0.05$] and $Mg(OH)_2$ [$F(8,18)=114.7$, $p<0.05$] for 24 hours respectively, as indicated in Figure 4a. For the 24-hour culture with MgO, HUC density at 0.2 mg/mL was the highest in average among all. No significant differences were found

comparing the 0.2 and 0.3 mg/mL groups to the cells only control. Start with 0.5 mg/mL and above, all cell density of HUC were statistically lower than that of the cells only control. For the 24-hour culture with $Mg(OH)_2$, HUC density at 0.2 mg/mL was also the highest in average among all, and it was found to be statistically higher than the cells only control. The cell density of HUCs reduced significantly after cultured with $Mg(OH)_2$ of the concentration of 0.5 mg/mL and above as compared with cells only.

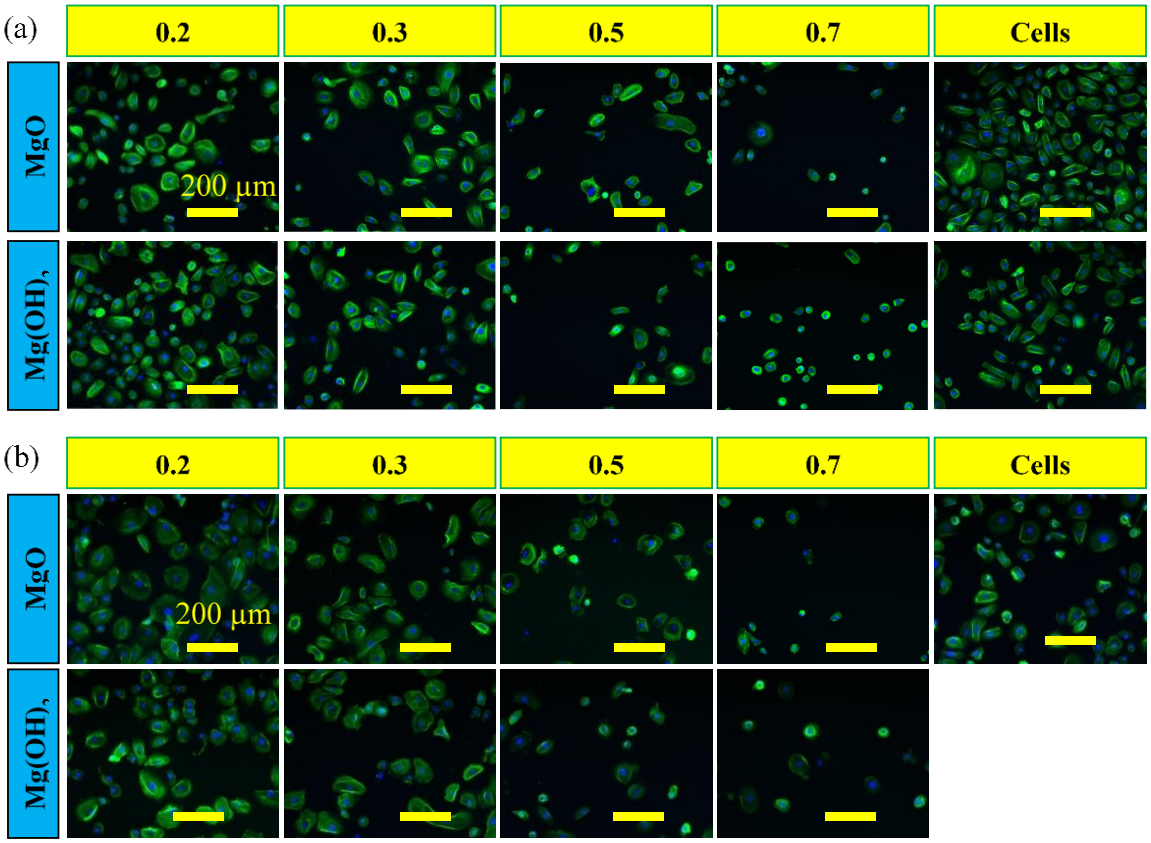

Figure 3. Representative fluorescence images of HUCs on the well plates after cultured with different concentrations of MgO and Mg(OH)2 nanoparticles from (a) 0.2 mg/mL to 2 mg/mL for 24 hours, and (b) from 0.2 mg/mL to 0.7 mg/mL for 48 hours respectively. Blue color indicates DAPI-stained nuclei and green color indicates Alexa Fluor® 488-stained F-actin (cytoskeleton). Scale bar = 200 µm for all images. Original magnification: 100×.

Statistically significant differences in normalized HUC spreading area were found with $Mg(OH)_2$ [$F(3,8)=3.937$, $p=0.047$], but not for MgO after a 24-hours culture, as

indicated in Figure 4b. The spreading area of HUCs after cultured with MgO showed a decreasing trend as the concentration of MgO increased, with the 0.2 mg/mL being the highest and the 0.7 mg/mL being the lowest in average. The spreading area of HUCs after cultured with $Mg(OH)_2$ also showed a decreasing trend, and the 0.2 mg/mL was statistically higher than that of 0.7 mg/mL. Similarly, statistically significant differences of normalized aspect ratio were found with $Mg(OH)_2$ [$F(3,8)=12.28$, $p=0.0017$], but not for MgO after cultured for 24 hours, as indicated in Figure 4c. For MgO, the aspect ratio of 0.7 mg/mL was the lowest in average, and no statistical difference was found. For HUCs cultured with $Mg(OH)_2$, 0.3 mg/mL showed a statistically higher aspect ratio than that of 0.7 mg/mL.

3.2 HUC Behaviors after a 48-hour Culture with MgO and $Mg(OH)_2$ Particles

After culture with different concentrations of MgO or $Mg(OH)_2$ nanoparticles for 48 hours, HUCs showed healthy cell morphology with 0.2 mg/mL and 0.3 mg/mL of MgO or $Mg(OH)_2$, as indicated in Figure 3b. The HUC numbers reduced at 0.5 mg/mL and 0.7 mg/mL of MgO or $Mg(OH)_2$ after culture for 48 hours.

Statistically significant differences in HUC density were found after cultured with MgO [$F(3,8)=12.12$, $p<0.05$] and $Mg(OH)_2$ [$F(3,8)=59.64$, $p<0.05$] for 48 hours, as indicated in Figure 10a. For the 48-hour culture of MgO, HUC density at 0.2 mg/mL maintained the highest in average among all, and it was significantly greater than that of 0.5 and 0.7 mg/mL. At a concentration of 0.5 and 0.7 mg/mL, the HUC density was statistically lower than cells only control. For the 48-hour culture of $Mg(OH)_2$, it was found that the highest cell density at 0.2 mg/mL in average. The concentration of 0.7 mg/mL had

the lowest cell density after culture, which was statistically lower than that of 0.2 mg/mL and cells only control.

Statistically significant differences of normalized HUC spreading area were found with MgO [$F(3,8)=7.737$, $p=0.0042$] and $Mg(OH)_2$ [$F(3,8)=18.08$, $p=0.0006$] after culture for 48 hours, as indicated in Figure 10b. In the 48-hour culture of MgO, the spreading area of HUC showed a decreasing trend with the increase of MgO concentrations. The 0.2 mg/mL had the highest spreading area in average, which was statistically greater than that of 0.5 mg/mL and 0.7 mg/mL. The 0.7 mg/mL had the lowest spreading area in average, which was also statistically lower than that of 0.3 mg/mL. A similar trend showed for the 48-hour culture of $Mg(OH)_2$, with 0.2 mg/mL being the highest and 0.7 mg/mL being the lowest in average, and 0.2 mg/mL was found to be statistically higher than all other groups. Statistically significant differences in normalized aspect ratio were not found after cultured with MgO or $Mg(OH)_2$ for 48 hours, as indicated in Figure 10c. For MgO or $Mg(OH)_2$, a decreasing trend in aspect ratio was observed in average, with the 0.2 mg/mL being the highest and the 0.7 mg/mL being the lowest.

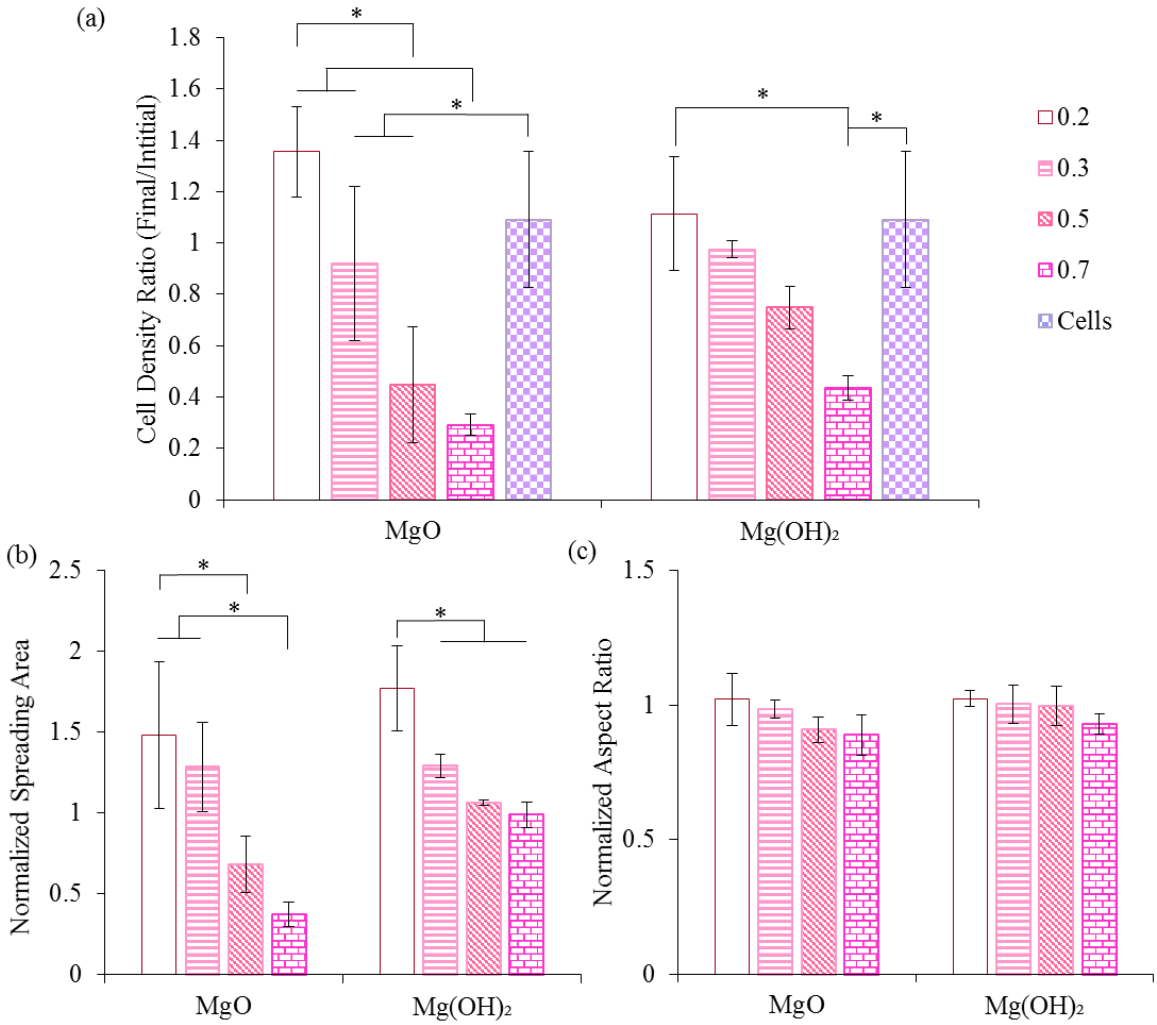

Figure 4. HUC behaviors after 24 hours of incubation with concentrations of MgO and $Mg(OH)_2$ nanoparticles from 0.2 mg/mL to 2 mg/mL. (a) Average density ratio of adhered HUCs on culture plates. (b) Normalized spreading area of adhered HUCs. Average spreading area of adhered HUCs in the culture with different concentrations of MgO and $Mg(OH)_2$ nanoparticles was normalized by the cells only control group. (c) Normalized aspect ratio (Dmax/Dmin) of adhered HUCs. Average aspect ratio of adhered HUCs in the culture with different concentrations of MgO and $Mg(OH)_2$ nanoparticles was normalized by the cells only control group. Data are mean ± standard deviation (N=3); *p<0.05.

3.3 Media Analysis after cultured with MgO and $Mg(OH)_2$ Particles for 24 and 48 hours

In Figure 5a, statistically significant differences were found between the pH values of the collected media for 24-hour culture with MgO [$F(9,20)=153.3$, $p<0.05$], and for 24 hours with $Mg(OH)_2$ [$F(9,20)=77.55$, $p<0.05$] respectively. It was observed that as the

concentration of either MgO or $Mg(OH)_2$ increase, so did the pH. At a concentration of 2.0 mg/mL, both MgO and $Mg(OH)_2$ resulted in the highest pH, where the difference between that particular pH was statistically higher when compared to that of other groups. The cells only and media reference had similar pH, and no significant difference was found when compared them to the groups with a concentration of 0.2 and 0.3 mg/mL of MgO or $Mg(OH)_2$. For culturing 48 hours with MgO [$F(5,12)=94.99$, $p<0.05$] and for 48 hours with $Mg(OH)_2$ [$F(5,12)=89.53$, $p<0.05$], statistically significant differences in pH were found as indicated in Figure 5b. After culture, a concentration of 0.7 mg/mL of MgO or $Mg(OH)_2$ had the highest pH, and the differences with all other groups were found to be statistically significant, expect with 0.5 mg/mL MgO for a culture of 48 hours.

There were statistically significant differences in the Mg^{2+} ion concentrations for 24 hours with MgO [$F(9,20)=110.4$, $p<0.05$] and $Mg(OH)_2$ [$F(9,20)=27.7$, $p<0.05$] respectively, as indicated in Figure 6a. For MgO and $Mg(OH)_2$, the highest Mg^{2+} ion concentration was for a concentration of 2 mg/mL, which was statistically higher than other groups of MgO or $Mg(OH)_2$. It was observed that as the concentration of either MgO or $Mg(OH)_2$ increase, so did the Mg^{2+} ion concentration. The cells only and media reference had similar Mg^{2+} ion concentration, and no significant difference was found when compared them to the groups with a concentration of 0.2 and 0.3 mg/mL of MgO or $Mg(OH)_2$. For the 24-hour culture, the Mg^{2+} ion concentrations were higher for all concentrations of MgO than those with the same concentrations of $Mg(OH)_2$. For the 48-hour culture, statistically significant differences were also found with MgO [$F(5,12)=11.34$, $p<0.05$] and $Mg(OH)_2$ [$F(5,12)=89.53$, $p<0.05$] respectively. For the 48 hours period, the

highest Mg^{2+} ion concentration for both MgO and $Mg(OH)_2$ was 0.7 mg/mL. The Mg^{2+} ion concentrations of the media cultured with different MgO was also higher than those of their counterparts in $Mg(OH)_2$.

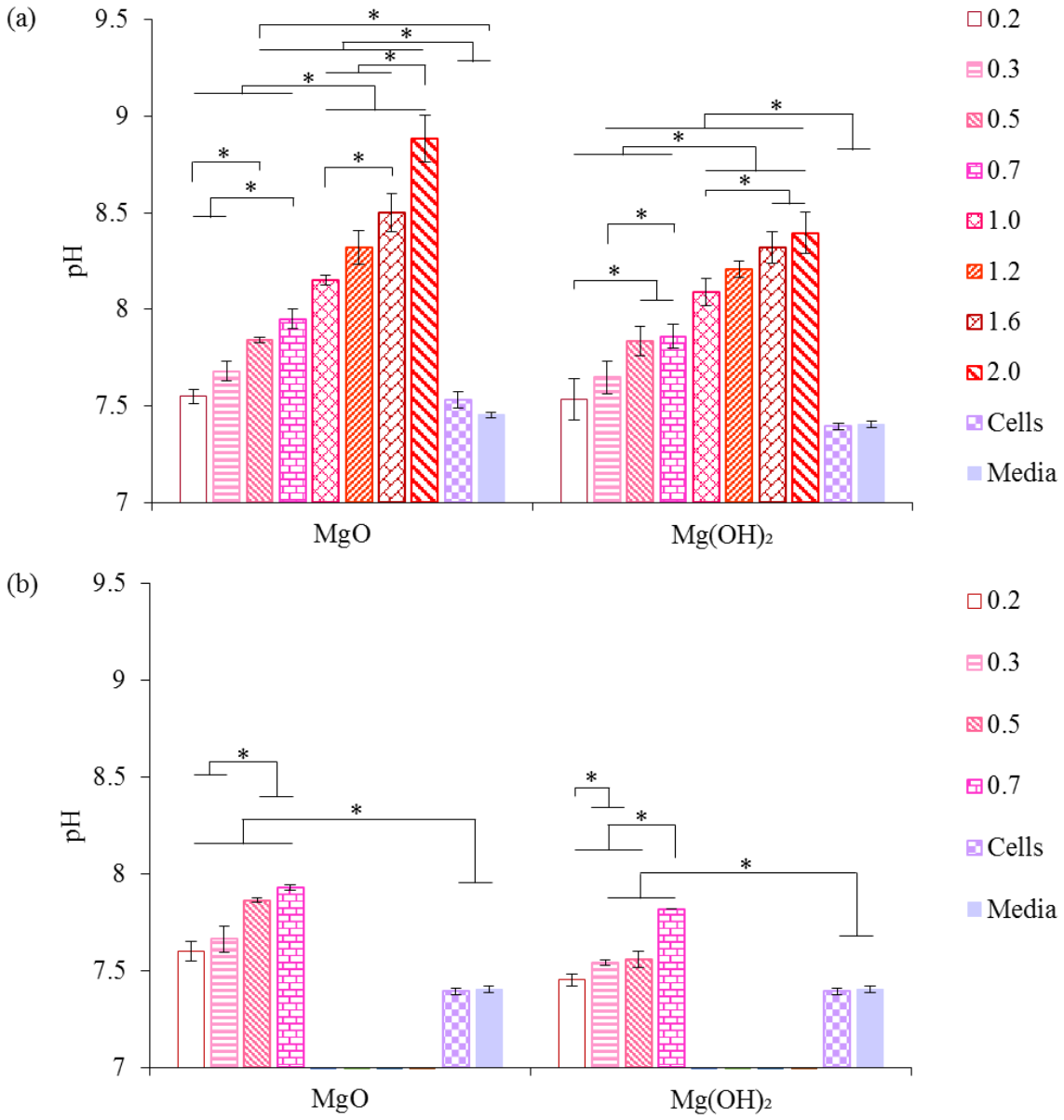

Figure 5. The pH value of collected media after cultured with different concentrations of MgO and $Mg(OH)_2$ nanoparticles from (a) 0.2 mg/mL to 2 mg/mL for 24 hours, and (b) from 0.2 mg/mL to 0.7 mg/mL for 48 hours respectively. Data are mean ± standard deviation (N=3). *$p<0.05$.

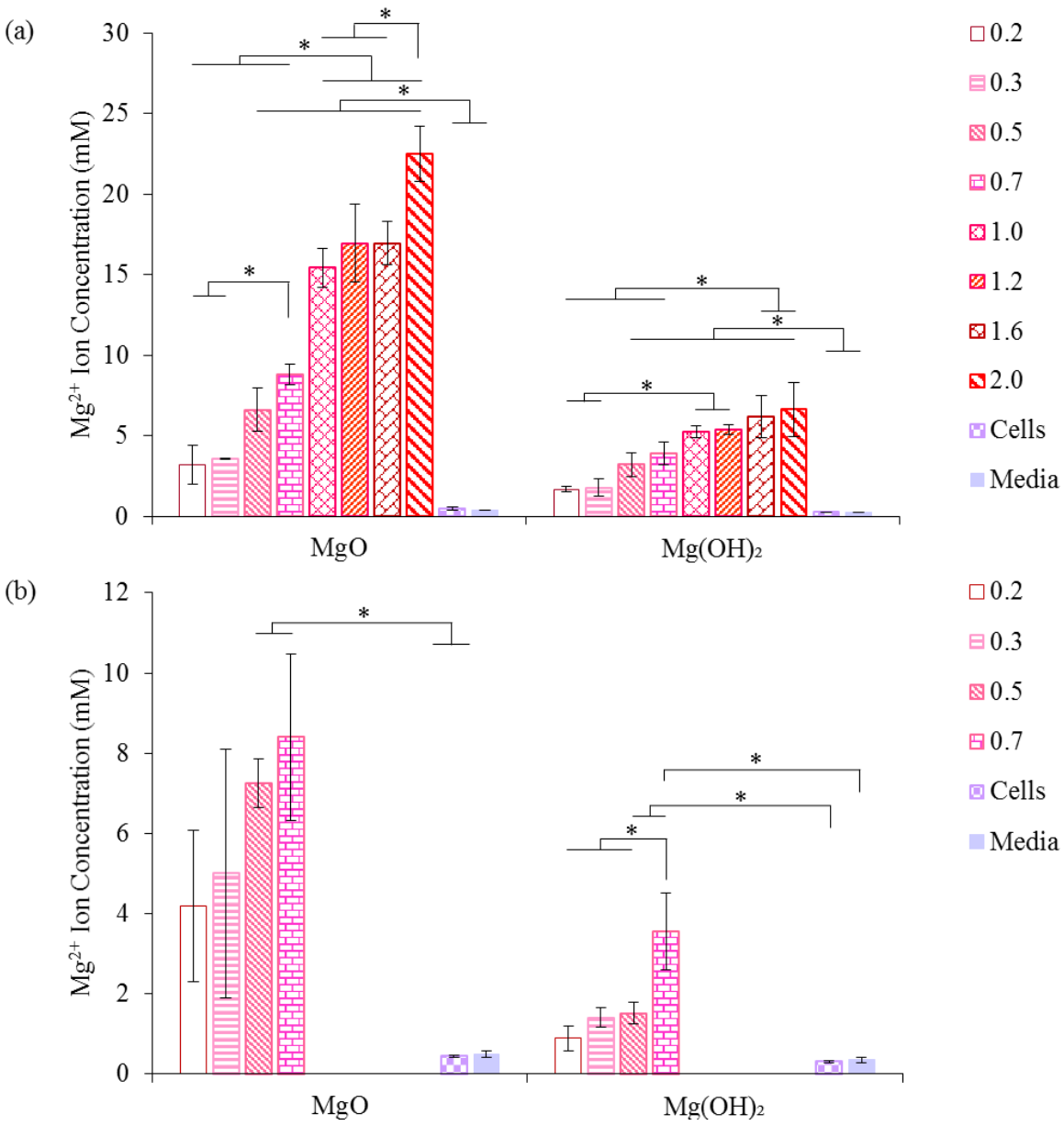

Figure 6. Mg^{2+} ion concentration of collected media after cultured with different concentrations of MgO and $Mg(OH)_2$ nanoparticles from (a) 0.2 mg/mL to 2 mg/mL for 24 hours, and (b) from 0.2 mg/mL to 0.7 mg/mL for 48 hours respectively. Data are mean ± standard deviation (N=3). *$p<0.05$.

4. Discussion

In this study, MgO and $Mg(OH)_2$ nanoparticles were cultured with HUCs using direct exposure culture method, where the nanoparticles and the established HUC layer were in direct contact. The MgO and $Mg(OH)_2$ have a density of 3.6 mg/cm^3 and 2.34

mg/cm^3 respectively[31], which are higher than the density of the HUC media. During the culture, MgO and $Mg(OH)_2$ particles rapidly settled to the bottom of the well, and they would be directly on top of the established HUC layer. Sawai et.al suggested the contact between MgO and bacterial cells resulted significant cell death[32]. Dong et.al reported the cell membranes/walls of the bacterial cells were disrupted by direct contact with nano $Mg(OH)_2$ particles[33].

Many literatures categorized MgO and $Mg(OH)_2$ particles as stable nanoparticles due to their stable crystal structures and low solubility in water (0.062 mg/mL and 0.009 mg/mL respectively at 18 °C[31]). Based on this study, however, it is suggested that both the MgO and the $Mg(OH)_2$ nanoparticles underwent complex dissociation processes during the HUC culture. The Mg^{2+} ions and the hydroxide ions were the final products of the dissociation following the overall equation 1 and 2[34-35]:

$$MgO\,(s) + H_2O\,(l) \longrightarrow Mg^{2+}\,(aq) + 2OH^-\,(aq) \quad (1)$$

$$Mg(OH)_2\,(s) \rightleftharpoons Mg^{2+}\,(aq) + 2OH^-\,(aq) \quad (2)$$

At 25 °C in water, the Gibb's free energy for the overall Eqt.1 and Eqt.2 were 62.12 kJ/mol and 63.09 kJ/mol respectively. Thusly, the dissociation of MgO and $Mg(OH)_2$ nanoparticles were thermodynamically unfavorable in water at 25 °C. During the HUC culture, however, the buffer system of the HUC media, which is composed of 4-(2-hydroxyethyl)-1-piperazineethanesulfonic acid (HEPES) and bicarbonate, will balance the dissociated hydroxide ions and drive the further dissociation of MgO and $Mg(OH)_2$ nanoparticles. Specifically, the concentration of Mg^{2+} ions were found three orders of magnitude higher than that of resulting hydroxide ions, due to the balance from the buffer

system. As indicated in Figure 7, 40 % to 60 % of MgO and 20 % to 30 % of $Mg(OH)_2$ particles dissociated into Mg^{2+} ions during the 24-hour culture.

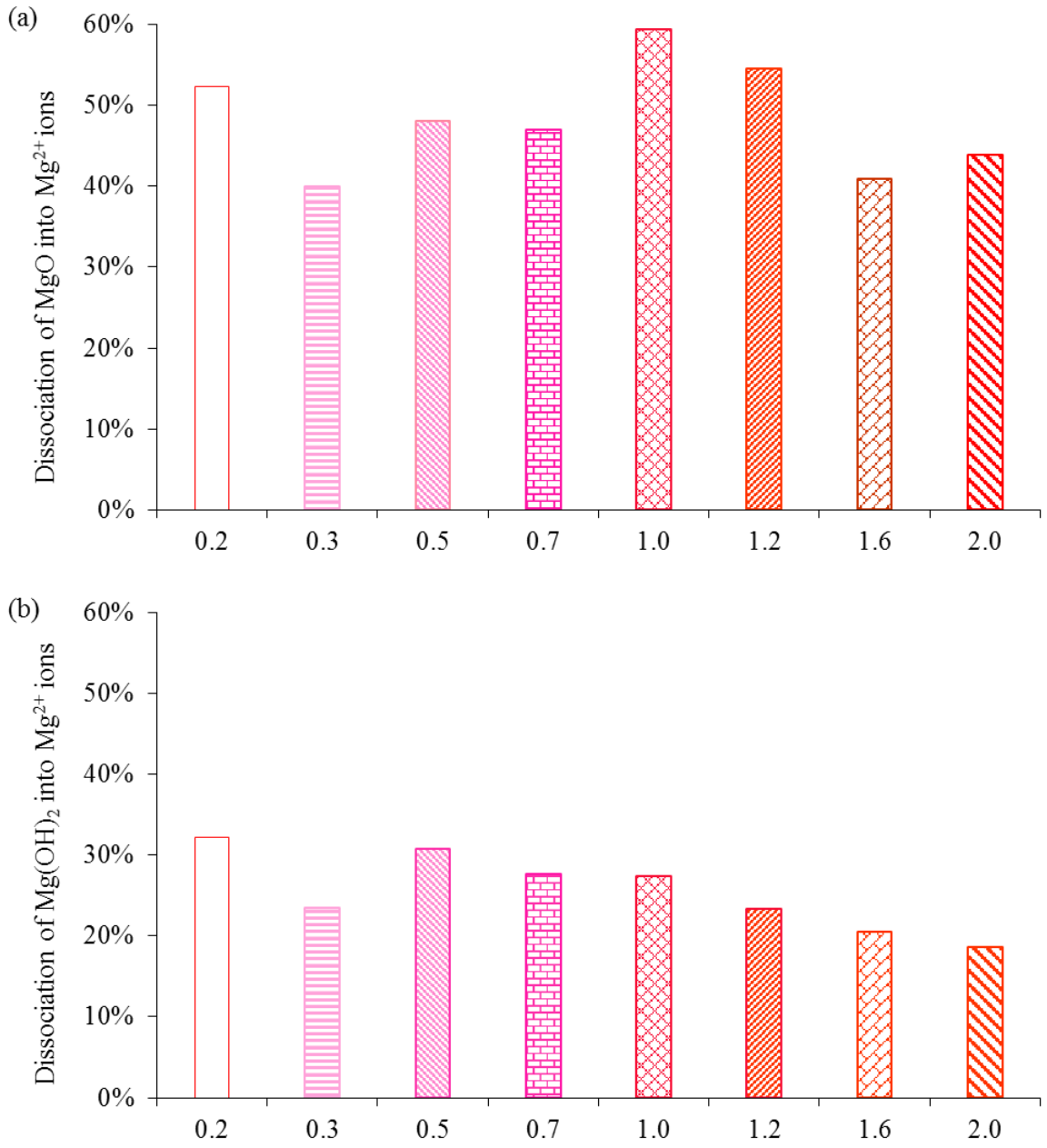

Figure 7. Dissociation percentage of (a) MgO and (b) $Mg(OH)_2$ nanoparticles into Mg^{2+} ions after HUC culture for 24 hours with different initial concentration from 0.2 mg/mL to 2.0 mg/mL.

Considering the presence of abundant CO_2 and bicarbonate during the cell culture, $MgCO_3$ may also be an intermediate product during the dissociation of MgO and $Mg(OH)_2$ nanoparticles[36] (Eqt.3). In addition, $Mg(OH)_2$ should be an intermediate product during the dissociation of MgO[37] (Eqt.4).

$$Mg^{2+}\,(aq) + H_2O\,(l) + CO_2\,(aq) \leftrightharpoons MgCO_3\,(s) + 2H^{+}\,(aq) \quad (3)$$

$$MgO\,(s) + H_2O\,(l) \leftrightharpoons Mg(OH)_2\,(s) \quad (4)$$

Consequently, the dissociation of MgO and $Mg(OH)_2$ nanoparticles might be higher than the calculated percentages in Figure 13, i.e., 40 % to 60 % for MgO and 20 % to 30 % for $Mg(OH)_2$.

According to this study, the HUC density was inhibited if the MgO and $Mg(OH)_2$ concentrations exceeded 0.5 mg/ml. Interestingly, the pH value and the Mg^{2+} ion concentration from the dissociation at 0.5 mg/ml did not exceed the critical dosage, i.e., 8.6 and 10 mM respectively[5]. In a fact, the pH exceeded the critical dosage at 1.6 mg/ml for MgO, and the pH of $Mg(OH)_2$ was found lower than 8.6 even after culturing with a concentration of 2 mg/mL. Similarly, the Mg^{2+} ion concentration exceeded the critical dosage at 1.0 mg/ml for MgO, and the Mg^{2+} ion concentration of $Mg(OH)_2$ was found lower than 10 mM even after culturing with a concentration of 2 mg/mL. As aforementioned, MgO and $Mg(OH)_2$ nanoparticles were in direct contact with HUCs during the culture. It is possible that the HUCs were exposed to a locally higher pH and Mg^{2+} ion concentration during the dissociation of MgO and $Mg(OH)_2$ particles, which resulted in significant reduction of HUC density.

In a summary, the concentration of MgO and $Mg(OH)_2$ particles at 0.5 mg/ml and above showed a significant decrease of HUC density after 24-hour and 48-hour culture. The concentration of MgO and $Mg(OH)_2$ at 1.0 mg/ml and above showed no viable cells after 24-hour culture.

Chapter 4 Improvement of Magnesium using Alloying for Urological Device Application

1. Introduction

In previous studies, it has been shown that adding zinc (Zn) and strontium (Sr) to Mg resulted in alloys with improved mechanical and corrosion properties as compared with pure Mg[38]. Additionally, Zn and Sr have both shown biocompatible properties, particularly where Zn is an essential element in the body and participates in the syntheses of enzymes, and Sr showed improvement of osteoblast proliferation *in vitro*[39-40]. Thus, Mg alloys, particularly Mg–4Zn–xSr, are promising as a biodegradable material for the urological device applications. Thus, we investigated the cytocompatibility of Mg–4Zn–xSr alloys with HUCs using exposure culture method for urological device applications. These results will provide information about the possible adverse effects of Mg–4Zn–xSr alloy and the degradation behavior of Mg–4Zn–xSr alloy in the early stage, offering a representative model and a reduction of potential risk to future animal and clinical studies.

2. Materials and Methods

2.1Sample Preparation

Four types of Mg–4Zn–xSr alloys were prepared by a standard metallurgical process of melting, casting, rolling and heat treatment as described previously[38]. Specifically, these four alloys had 4 wt% Zn in all and 0.15 wt% Sr in ZSr41_A, 0.5 wt% Sr in ZSr41_B, 1.0 wt% Sr in ZSr41_C and 1.5 wt% Sr in ZSr41_D. Pure magnesium (Mg, as cast, Alfa Aesar) served as the control, while titanium (Ti, Alfa Aesar) provided a non-degradable metallic reference for the study. The Mg–4Zn–xSr, Mg, and Ti substrates were polished using silicon carbide abrasive papers (SiC, Ted Pella Inc., Redding, CA, USA) in

the sequence of 600, 800 and 1200 grit respectively. The resulting polished substrates were placed in an ultrasonic bath (Model 97043-936, VWR) for 15 min to clean and remove the debris. As a representative of the current commercially available materials for ureteral stents, polyurethane stents (PU; Cook Medical, Bloomington, IN, USA) were included as a control and prepared as previously described. Premium microscope glass slides (Fisher Scientific, Hampton, NH, USA) were used as another control for cell culturing.

For all studies, the dimensions and shape of the substrates used were 5x5x1 mm squares. The Mg–4Zn–xSr, Mg, and Ti substrates were cut using a Notcher (NO.100, Whitney Metal Tool CO.), and the PU samples were using scissors and the glass samples were cut with a glass cutter. Before the cell culture, all the substrates underwent a cleaning process that consisted of first being immersed in acetone (Sigma Aldrich, St Louis, MO, USA) and then 200 proof ethanol (Sigma Aldrich, St Louis, MO, USA) with ultrasonic for 60 min each at room temperature. These clean samples were disinfected by exposing each side of the substrates to ultraviolet (UV) radiation for an hour.

2.2 Preparation of Human Urothelial Cell Culture

The culture media of HUCs (Sciencell, Carlsbad, CA, USA) was prepared by supplemented basal urothelial cell media (UCM; Sciencell, Carlsbad, CA, USA) with 1% urothelial cell growth supplement (UCGS; Sciencell, Carlsbad, CA, USA) and 1% penicillin/streptomycin (P/S; Sciencell, Carlsbad, CA, USA). To enhance the attachment of HUCs, T-75 flasks were coated with 2 μg/cm^2 of poly-L-lysine (PLL; Sciencell, Carlsbad, CA, USA). Specifically, 15 μl of 10 mg/mL PLL were added to a T-75 flask containing 25 mL of distilled (DI) water. The flask was then placed in an incubator (MCO-

19AIC, SANYON Electric CO. Ltd., JP) for at least 2 hours then washed with DI water twice to remove the non-adhered PLL residual. Using 25 mL of UCM, the HUCs were cultured in coated T-75 flask. The media in the flask was consistently changed every other day until 90 to 100% confluence.

2.3 Exposure Culture of HUCs with Mg-4Zn-xSr Alloy

The exposure culture was adopted as the culture methodology in this study. The HUCs were cultured in the PLL-coated 12-well plates for one day before the sample introducing. After cell layer had established, 5 phase images were taken of each well using an optical microscope (Eclipse Ti and NIS software, Nikon, Melville, NY, USA). An ImageJ analysis tool was used to count the total number of cells of each image. The initial cell density (C_o, cells/cm^2) of each well can be calculated by dividing the cell number by the image surface area.

The substrates were introduced into each well by placing them in Transwell® insert (BD Falcon™) which has a membrane of 0.4 μm pore size. Also, the cell reference, consisting of HUCs cultured in wells without any substrate present, was referred to as "Cells". Likewise, the media reference, 4 mL of blank media with no cells or substrates, was labeled "Media". All the groups were cultured for 24 hours and 48 hours. When groups were cultured for 48 hours, the media was changed during the first 24-hour interval. Each group, for all studies, was prepared in triplicate. All the well-plates in two studies were cultured in a sterile, 5% CO_2/95% air, humidified environment, thus a standard cell culture condition.

2.4 Characterization of Viability and Morphology of HUCs

When reached the prescribed culture time, HUCs were fixed and stained to observe the morphology of the cells and obtain the cell density based on the fluorescence images of HUCs. First, 1 mL of phosphate buffered saline (PBS) was used to wash away non-adhered cell. Then, 1 mL of 4% paraformaldehyde (VWR, Radnor, PA, USA) was added to the wells for 20 min for fixation of cells and followed by three washing of PBS. The cells were then stained by adding Alexa Fluor® 488 (Invitrogen) for 20 min and 4', 6-diamidino-2-phenylindole (DAPI; Invitrogen) for 5 min. After the appropriate time for each dye, the cells were washed twice using 1 mL PBS. A fluorescence microscope (Eclipse Ti and NIS software, Nikon, Melville, NY, USA) was used to collect the desired images. Based on 15 fluorescence images per well, the final cell density (C_i, cells/cm^2) were calculated. The change in cell density was determined by dividing the final cell density (C_i) by the initial cell density (C_o).

2.5 Sample Characterization before and after HUC Culture

The mass of each sample was recorded using an analytical balance (Ms104S, Mettler Toledo, Columbus, OH, USA). Specifically, the mass before cell culture was referred as the initial mass (M_o). After the cell culture, the samples were removed from their respective well plates and left out to air-dry at room temperature for 12 hours and the mass of each sample was recorded as the final mass (M_f). The mass change ratio was obtained be dividing the final mass (M_f) by the initial mass (M_o) for each sample.

Both before and after culture, samples were mounted on a flat SEM holder (Ted Pella Inc., Redding, CA, USA) using double-sided copper tape. A sputter coater (Model

108, Cressington Scientific Instruments Ltd., Watford, UK) was then used to sputter coat the mounted samples with platinum/palladium at 20 mA for 60 seconds. A scanning electron microscope (SEM; Nova NanoSEM 450, FEI Inc. Hillsboro, OR, USA) with the Concentric Backscattered detector was used to collect SEM images of all the samples under an acceleration voltage of 10 kV and a spot size of 4. Also, the attached energy dispersive x-ray spectroscopy (EDS; Aztec, Oxford Instruments, Abingdon, UK) was used to determine the surface elemental compositions of the substrates.

2.6 Media Analysis after In Vitro Degradation of Mg–4Zn–xSr Alloys in HUC Culture

After each culture, the remaining media was collected and examined to find the pH and Mg^{2+}, Zn^{2+}, and Sr^{2+} ion concentrations. In the case of the pH measurements, a pH meter (SB70Pm, SympHony) was used. To obtain the Mg^{2+}, Zn^{2+}, and Sr^{2+} ion concentrations, inductive coupled plasma-optical emission spectrometry (ICP-OES; Optima 8000, Perkin Elmer, Waltham, MA, USA) was used. Specifically, dilutions of the collected media to a factor of 1:100 were made with DI water so that the total volume turned out to be 10 mL. Using the Mg standard (Perkin Elmer) diluted ranges of 0.5, 1, 2 and 5 mg/L respectively, a calibration curve was created, and the Mg^{2+} ion concentrations could be determined. Similarly, using the Zn and Sr standard (Perkin Elmer) diluted ranges of 0.7 and 1 mg/L respectively, the Zn^{2+} and Sr^{2+} ion concentration could be determined by the standard calibration curves.

2.7 Statistical Analysis

For each quantitative data type in all studies, statistical analysis was conducted. The averages and standard deviations of the triplicate data were calculated and plotted in graphs. To examine the statistical differences between the different groups, one-way analysis of variance (ANOVA) was used, followed by using Tukey *post-hoc* test for obtaining comparisons between pairs of the different groups. For data to be considered statistically significant, $p < 0.05$.

3. Results

3.1 HUCs Morphology and Adhesion after Cultured with Mg–4Zn–xSr Alloys

After exposure culture of 24 hours and 48 hours, the HUCs underneath the Mg–4Zn–xSr alloys, AZ31, and Mg substrates had similar cell morphology when compared to the cells underneath the Ti, PU and glass control, as well as cells only reference as indicated in Figure 8.

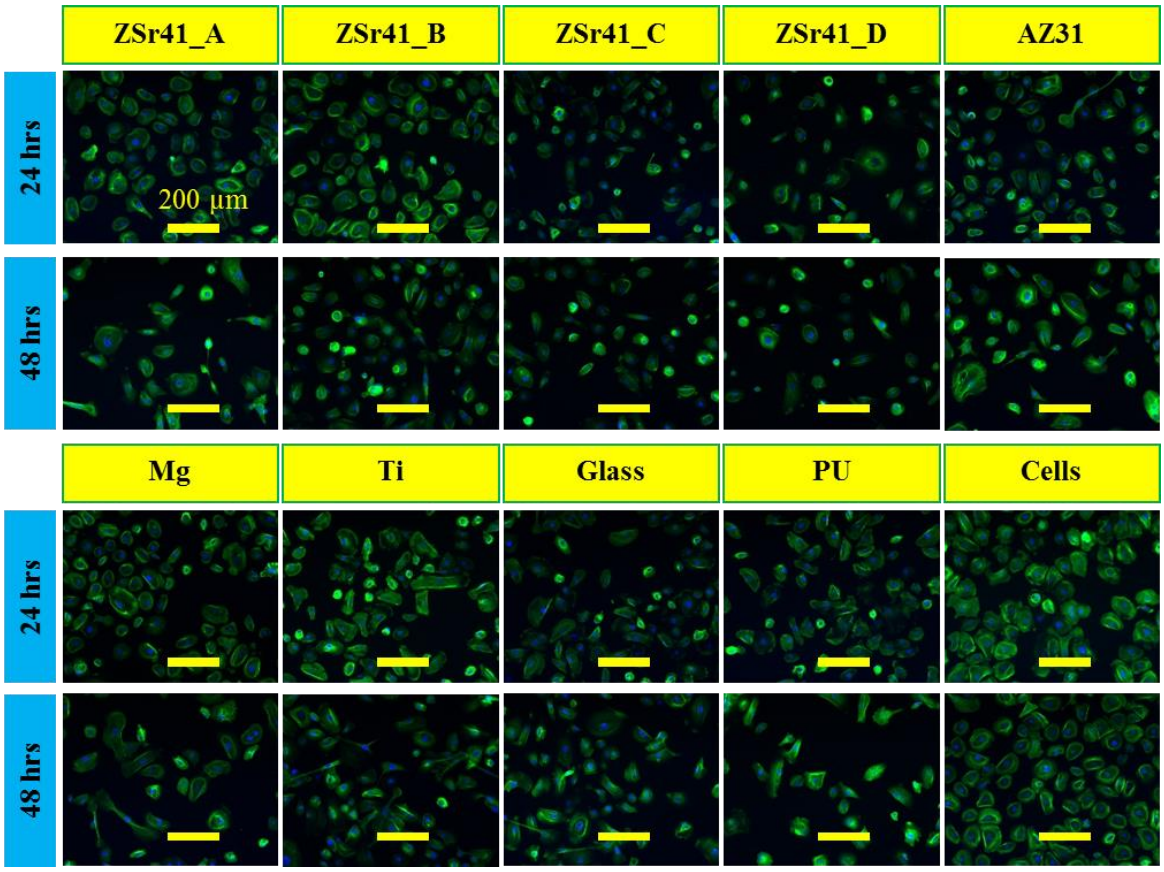

Figure 8. Representative fluorescence images of HUCs on the well plates after cultured with different materials of interest for 24 hours and 48 hours. Blue color indicates DAPI-stained nuclei and green color indicates Alexa Fluor® 488-stained F-actin (cytoskeleton). Scale bar = 200 µm for all images. Original magnification: 100×.

The cell density ratio (final/initial) quantified based on the fluorescence images and phase images (not shown) were summarized and plotted in Figure 9. There were statistically significant differences among the groups in the 24 hours [$F(9,20)=3.107$, $p<0.05$] and the 48 hours [$F(9,20)=5.527$, $p<0.05$] culture respectively. For the exposure culture of 24 hours, the ZSr41_B resulted in the highest cell density, and the ZSr41_D had the lowest cell density ratio in average among the Mg–4Zn–xSr, AZ31, and Mg. The cell density of ZSr41_D was statistically lower than that of the cell only reference, where ZSr41_D. Ti, PU, and glass showed similar results with cells reference. In regards to the

48-hour exposure culture, ZSr41_B showed the highest cell density ratio in average among the Mg–4Zn–xSr. Cell density ratio of ZSr41_A and ZSr41_D showed statistically lower than that of cells control. No statistically significant was found when compared ZSr41_B, ZSr41_C, AZ31, and Mg to the cells only reference. Ti, PU, and glass showed similar results with cells reference in 48-hour culture.

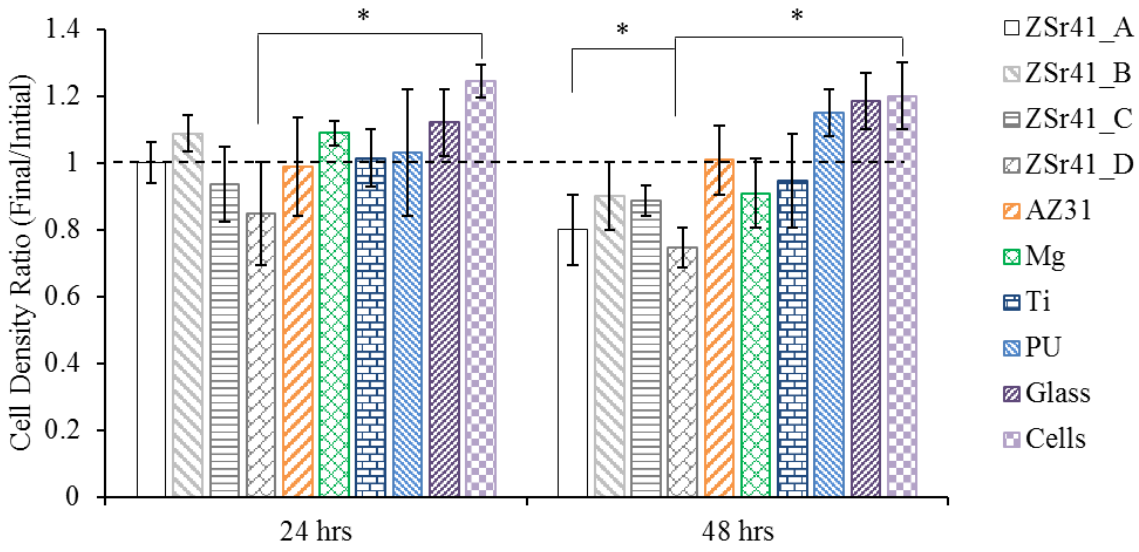

Figure 9: HUC density ratio (final/initial cell density) after cultured with different materials of interest for 24 hours and 48 hours under exposure culture. Data are mean ± standard deviation (N=3); *p<0.05

3.2 Surface Morphology and Elemental Compositions of the Samples

Before exposure culture, SEM images of the Mg–4Zn–xSr, AZ31, Mg, and Ti substrates showed flat surfaces with scratch marks in Figure 10 (0 hr row). These scratch marks originated from the polishing process using the SiC abrasive papers. Random bright precipitates were observed on ZSr41_B, ZSr41_C, and Mg, which most likely to be oxides or hydroxides. Glass showed flat and smooth without any outstanding marks or scratches. After the exposure culture of 24 hours, the Mg–4Zn–xSr, AZ31, and Mg substrates showed localized corrosion and deep cracks at the surface in Figure 10 (24 hrs row). Specifically,

ZSr41_A, ZSr41_B, and AZ31 showed smaller cracks than that of ZSr41_C, ZSr41_D, and Mg. Ti and glass showed no degradation but salts deposition on the surface. After a 48-hour culture, cracks on the ZSr41_B and AZ31deepened as the exposure time increased, where ZSr41_A remained similar morphology as 24 hours. The ZSr41_C, ZSr41_D, and Mg showed a more aggressive degradation morphology than other Mg-based substrates. Ti and glass showed similar surface morphology with no degradation compared with 24 hours.

From the EDS results in Figure 11a, the Mg-based substrates were composed of Mg and oxygen (O) that was not removed from the polishing substrates before the culture. Zn and Sr were found in ZSr41 samples. AZ31 possessed aluminum (Al) and Zn with a high percentage of Mg. Ti and O dominated in Ti substrates, where Si and O dominated in glass substrates. After HUC exposure culture of 24 hours (Figure 11b), a significant increase of O was found in all the Mg-based substrates. Zn was found in ZSr41 samples, but no Sr, which might due to low quantity after degradation. The carbon (C), sodium (Na), chloride (Cl), phosphorus (P), and calcium (Ca) was found on all the Mg-based substrates, which indicated salt deposition from the media. Ti and glass still possessed a high weight percentage of Ti and Si respectively after culture, with no significant change of O. C and Na were found on the surface of Ti and glass, which also indicated salt deposition from the media. After a 48-hour exposure culture, the elemental composition of each sample was similar to the 24 hours culture with no significant change as indicated in Figure 11c.

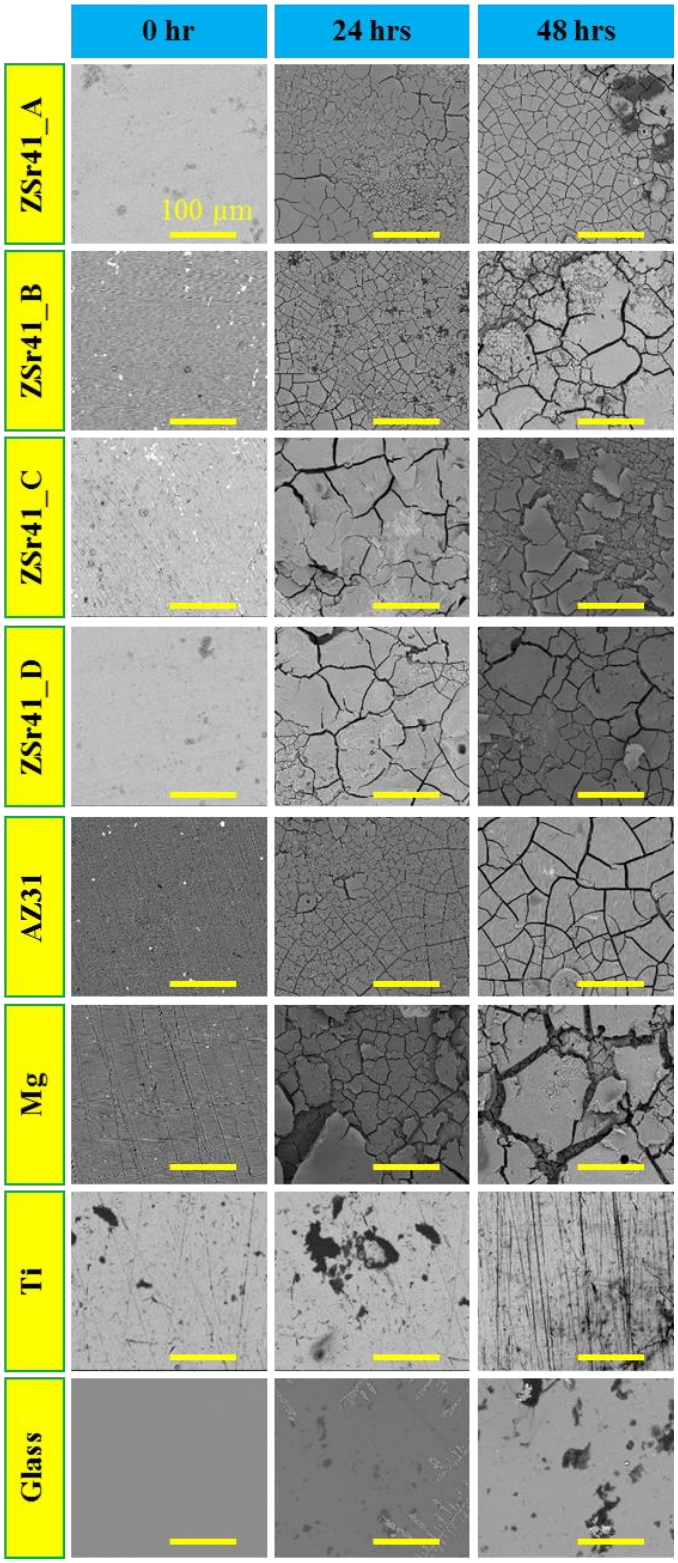

Figure 10: Representative SEM images of materials before (0 hour) and after cultured with HUCs under exposure culture for 24 hours and 48 hours. Scale bar = 100 µm for all images. Original magnification: 500x.

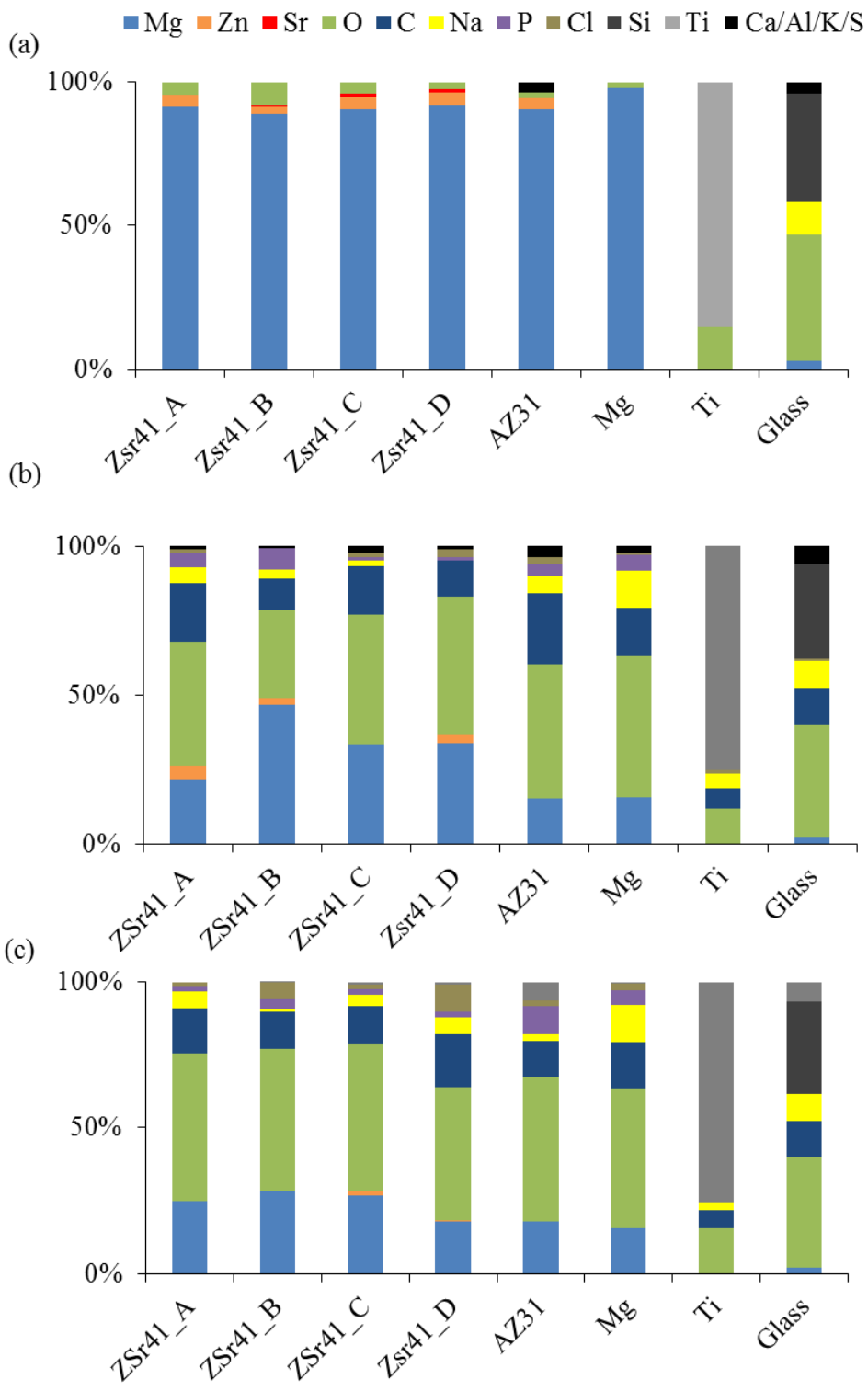

Figure 11: Surface elemental compositions of different substrates before and after cultured with HUCs using exposure culture method. (a) Before the samples were cultured with HUCs. (b) After the samples were cultured with HUCs for 24 hours. (c) After the samples were cultured with HUCs for 48 hours

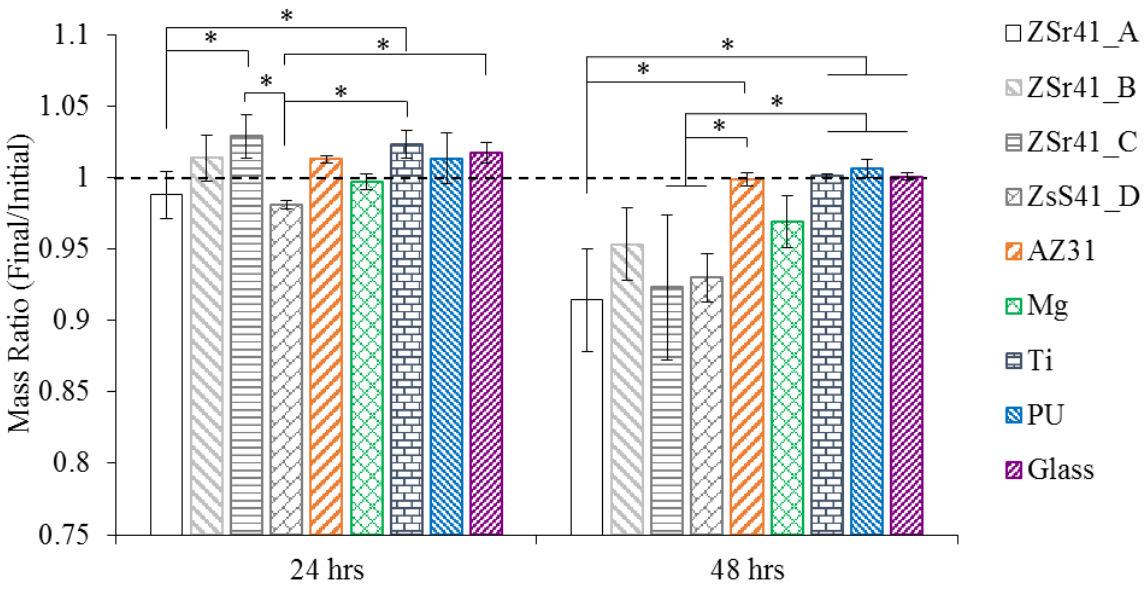

Figure 12. Mass ratio (final/initial mass) of the samples after cultured with the HUCs for 24 hours and 48 hours under exposure culture. Data are mean ± standard deviation (N=3); *p<0.05.

3.3 Mass Change of the Samples after the HUC culture

The mass ratio (final/initial) of the substrates after exposure culture of 24 hours and 48 hours is summarized in Figure 12. Statistically significant differences were found among the groups in 24 hours exposure [$F(8,18)=5.689$, $p<0.05$] and 48 hours exposure [$F(8,18)=7.242$, $p<0.05$]. After a culture of 24 hours, ZSr41_A and ZSr41_D had a lower mass ratio in average among Mg–4Zn–xSr, AZ31, and Mg. ZSr41_A was found to have statistically significant lower mass ratio than that of ZSr41_C and Ti substrate. Similarly, ZSr41_D showed more mass loss than that of ZSr41_C and Ti substrates as well as the glass, which was also statistically significant. No statistically significant was found when compared to ZSr41_B, ZSr41_C, AZ31 and Mg as well as Ti, PU and glass. After a 48-hour culture, Mg-based substrates had a decrease of mass except for AZ31 which remained stable mass. The mass ratio of ZSr41_A, ZSr41_C and ZSr41_D was also found to be

statistically lower than that of AZ31 and Ti substrates as well as the PU and glass controls. The Ti, PU, and Glass had no obvious mass change during the 24 and 48 hours culture.

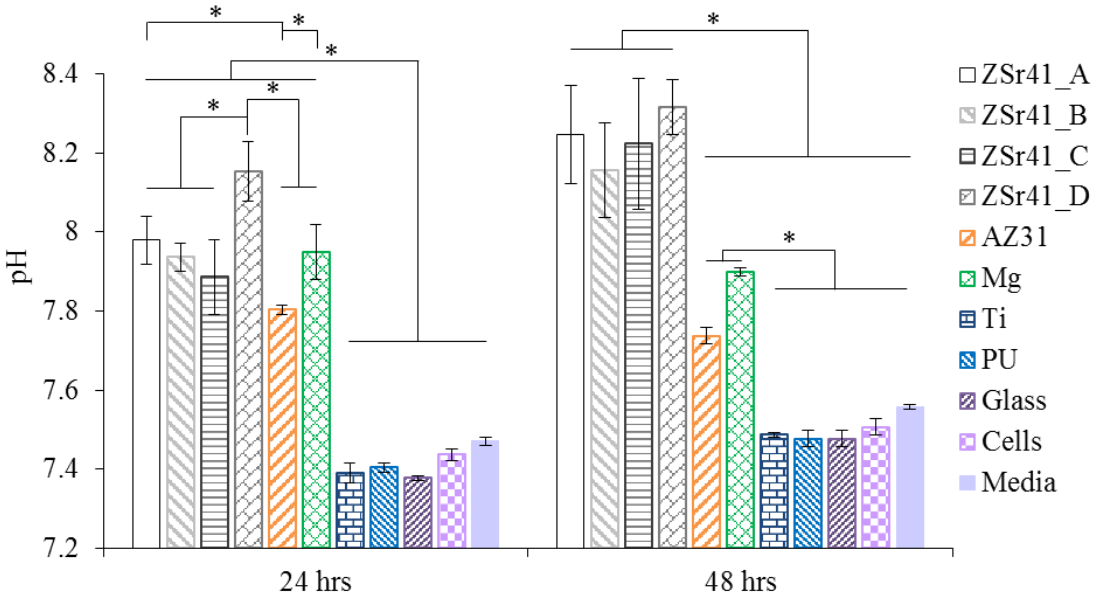

Figure 13. The pH of collected media after cultured with the materials of interest under HUC exposure culture for 24 hours and 48 hours. Data are mean ± standard deviation (N=3); *p<0.05.

3.4 The pH analysis of the Collected Media

After a 24-hour and 48-hour exposure culture, the pH of media increased after culturing with Mg-based substrates as indicated in Figure 13. Statistically significant difference was found in 24 hours [$F(10,22)=109.6$, $p<0.05$]and 48 hours [$F(10,22)=63.4$, $p<0.05$]. ZSr41_D had the highest pH after 24 hours culture, which was also statistically higher than all other Mg-based substrates. ZSr41_A and Mg had a higher pH compared with AZ31 as well, which was statistically significant. All the Mg-based substrates had a statistically significant higher pH compared with Ti, PU, glass, cells and media. No significant difference was found among the Ti, PU, glass, cells and media. After exposure culture of 48 hours, ZSr41 substrates all increased in pH, which was higher than all other

samples in average and was statistically higher than the control groups. Among ZSr41 substrates, ZSr41_D also had the highest pH in average, but no statistical difference was found as compared to other ZSr41 samples. AZ31 and Mg substrates had an increase of pH which was statistically higher than Ti, PU, glass, cells, and media. No significant difference was found among the Ti, PU, glass, cells and media.

3.5 Ion Concentrations of the Collected Media

The Mg^{2+}, Zn^{2+}, and Sr^{2+} ion concentrations of collected media after culturing with 24 hours and 48 hours are summarized in Figure 14. There were statistically significant differences found in the Mg^{2+} ion concentrations for 24 hours [$F(10,22)=45.66$, $p<0.05$] and 48 hours [$F(10,22)=34.64$, $p<0.05$]. ZSr41_D had the highest Mg^{2+} ion concentration after 24 hours and had statistically significant difference with all other Mg-based substrates. Mg-based substrates showed higher Mg^{2+} ion concentration than Ti, PU, glass, cells and media, which was also statistically significant. After 48 hours culture, Mg–4Zn–xSr substrates had an increase of Mg^{2+} ion concentration, while AZ31 and Mg substrates showed a decrease in average. Mg–4Zn–xSr showed the statistical difference with AZ31. In addition, ZSr41_A and ZSr41_D were statistically higher of Mg^{2+} ion concentration than Mg as well. It was shown that after 48 hours culture, Ti, PU, Glass, cells and media had relatively similar Mg^{2+} ion concentrations, and was shown to be statistically lower than Mg-based substrates.

The Zn^{2+} ion concentrations were found also to be statistically significant differences for 24 hours [$F(10,22)=7.28$, $p<0.05$] and 48 hours [$F(10,22)=10.32$, $p<0.05$], as indicated in Figure 14b. Mg–4Zn–xSr substrates all resulted in an increase of Zn^{2+} ion

concentrations that were higher than other samples in average, only ZSr41_A and ZSr41_D showed statistically significant differences with Mg, Ti, PU, glass, cells, and media. AZ31 showed an increase in Zn^{2+} ion concentration as well, but no statistically significant difference was found. After 48 hours, Zn^{2+} ion concentrations of ZSr41_A, ZSr41_B, ZSr41_C, and ZSr41_D were shown to be statistically higher than those of AZ31, Mg, Ti, PU, glass, cells, and media.

The Sr^{2+} ion concentrations also showed statistically significant differences for 24 hours [$F(10,22)=29.63$, $p<0.05$] and 48 hours [$F(10,22)=2.4$, $p<0.05$], as indicated in Figure 14c. After 24 hours culturing, ZSr41_D had the highest Sr^{2+} ion concentration in average, which was statistically significant difference with all other samples. After 48 hours, although the ZSr41 substrates are shown to have the higher Sr^{2+} ion concentrations when compared to other samples in average, there were no statistically significant differences found.

4. Discussion

4.1 The degradation behavior of Mg–4Zn–xSr Alloys

In the exposure culture of 24 hours, ZSr41_D had a fast degradation rate by having a lower mass ratio in average, a statistically higher pH value, and a statistically higher Mg^{2+} ion concentration than all other Mg-based samples, as indicated in Figure 5-7. ZSr41_C had a lower degradation rate by having a higher mass ratio, a lower pH value, and a lower Mg^{2+} ion concentration than all other Mg–4Zn–xSr alloys, although not statistically significant. During the 24-hour interval, the degradation rate of Mg-based samples followed ZSr41_D > ZSr41_A > ZSr41_B, ZSr41_C, Mg> AZ31 from fast to slow. During

the 48-hour interval, Mg–4Zn–xSr alloys showed a more rapid degradation compared to their counterparts in 24 hours, based on the significant mass loss and significant elevation of pH and Mg^{2+} ion concentration. Mg–4Zn–xSr alloys were found to be faster-degrading samples compared to AZ31 and Mg in HUC culture of 48 hours. Mg–4Zn–xSr alloys had a higher degradation rate in 48 hours compared to their counterparts in 24 hours. AZ31 and Mg, however, had a decreasing trend in degradation rate compared to their counterparts in 24 hours. Although Mg control showed less in degradation regarding mass ratio, pH value, and Mg^{2+} ion concentration, it had a significant loss in surface integrity during the 48 hours of incubation, as compared to other Mg-based substrates (Fig.3). The deep cracks on the surface of Mg control indicated that it might have a higher chance of a mechanical failure as implants, compared to other alloys in this study. During the 48-hour interval, the degradation rate of Mg-based samples followed ZSr41_D, ZSr41_A >ZSr41_B, ZSr41_C > Mg > AZ31 from fast to slow.

In a summary, ZSr41_B had the lowest degradation rate compared to other ZSr41 samples, which is a more promising Mg-based material for future *in vivo* study and clinical trials.

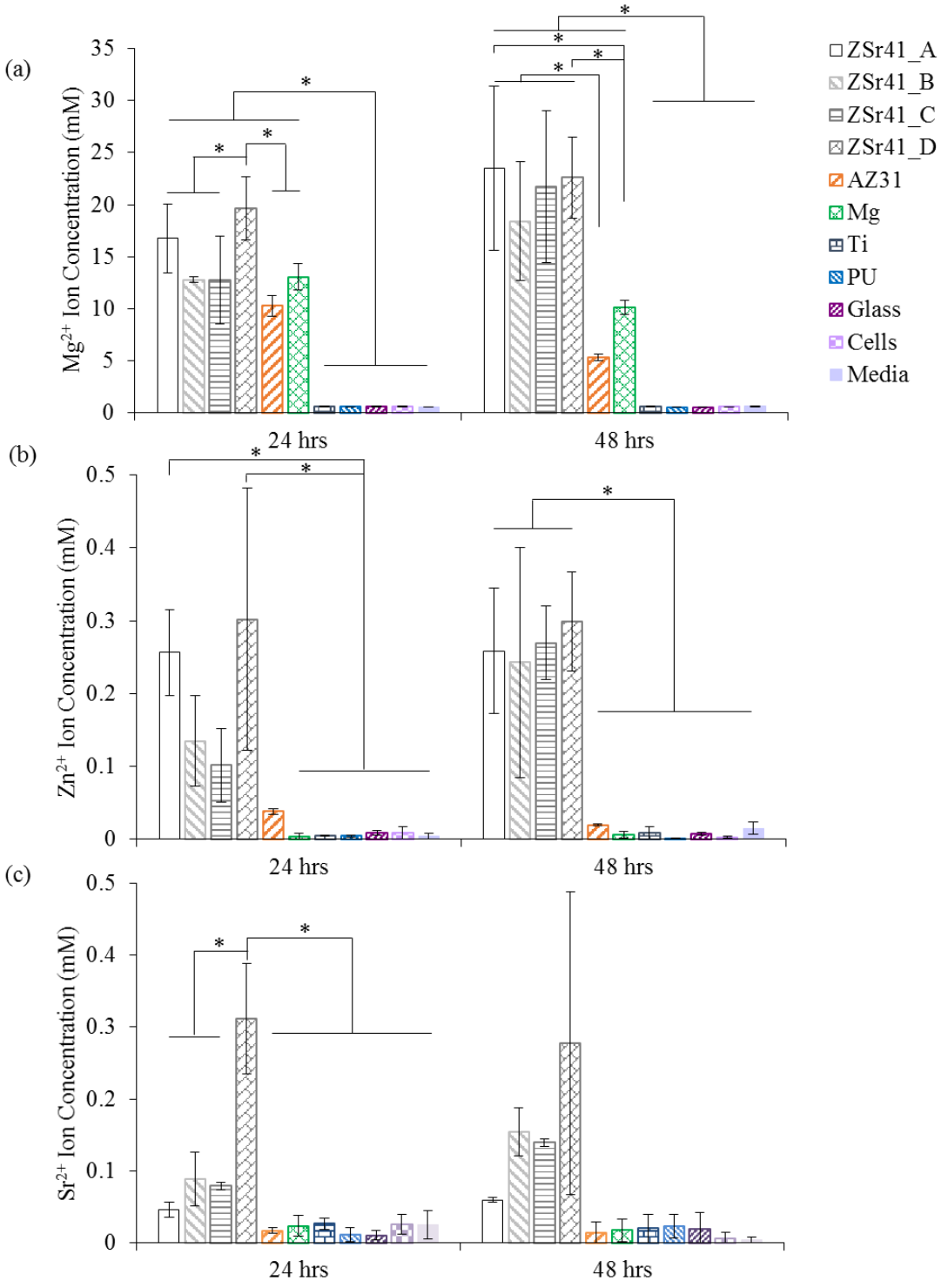

Figure 14. Ion concentrations of collected media after culture with different material of interest under HUC exposure culture for 24 hours and 48 hours. (a) Mg^{2+}, (b) Zn^{2+} and (c) Sr^{2+} ion concentration of the collected media. Data are mean ± standard deviation (N=3); *p<0.05.

4.2 Cytocompatibility of Mg Alloys with HUCs

When Mg degrades, it reacts with water and consistently releases hydroxide and Mg^{2+} ions to the local environment. Our previous study indicated that a decrease of HUC density was observed at pH of 8.3, and HUC density reduced significantly at pH of 8.6 and above[5]. In this study, ZSr41_D showed the highest pH of 8.1 at the 24-hour culture and the highest pH of 8.3 at the 48-hour culture. Thus, the high pH of ZSr41_D contributed to the resulting of less HUC density compared to other samples. In addition, the average pH values of the Mg–4Zn–xSr alloys, except ZSr41_D, were at around 8.2 during the 48-hour culture, which were significantly higher than all other samples. Thus, the relatively high pH might also contribute to the reducing of HUC density at 48 hours. Our previous study also indicated that the proliferation of HUC reduced at Mg^{2+} ion concentration of 10 mM and above, although HUCs remained stable cell numbers[5]. In this study, the highest Mg^{2+} ion concentration of 22 mM was found in ZSr41_A in the 48-hour exposure culture. All Mg-4Zn-xSr alloys exceeded 10 mM of Mg^{2+} ion concentration at both 24 hours and 48 hours culture. Consequently, the average cell density of Mg-4Zn-xSr alloys was lower than cell only controls. Both hydroxide and Mg^{2+} ions played a major role regarding the resulting cytocompatibility of Mg-4Zn-xSr alloys, and the releasing Mg^{2+} ions might be a more dominated factor. Mg–4Zn–xSr alloys also released the Zn and Sr ions during degradation, with the maximum concentration of 0.3 mM found in ZSr41_D at the 24-hour culture. None of them exceeded the lethal dosage, which reported from previous literature.

Chapter 5 Bioresoarble Hydroxyapatite as Coating Materials on Magnesium for Musculoskeletal Applications

1. Introduction

Human musculoskeletal system is made up of bones, muscles, tendons, ligaments and connective tissues, which provide support and mobility to the body[41]. Musculoskeletal injuries include fractures, dislocations, sprains, strains and traumatic amputations of neck, spine, pelvis and extremities[42]. These conditions are the number one cause of disabilities in the United States, where the bone tissue is one of the most commonly injured type of all musculoskeletal tissues[42]. When bone tissue damages occur, reconstructive orthopedic surgery is the preferred treatment to help the patients, including replacing the defective bone tissues with functional alternatives, or fixing and stabilizing defective bone tissues with bioactive implants. Autografts and allografts are often used for these surgeries[43-44]. However, the limitations of autografts and allografts restrict them from broader applications. For example, harvesting an autograft will damage the surrounding tissue and using an allograft will cause possible immunogenic response from the patient body[45].

Synthetic bio-ceramics, such as hydroxyapatite (HA), have shown great potentials to serve as functional materials for orthopedic device applications[46]. As an inorganic phase, HA accounts for 70% of dry weight of natural human cortical bones[47]. It deposits parallel to collagen fibers and provides stiffness to the bone[47]. Synthetic HA have also shown excellent biocompatibility, bioactivity, and osteoconductivity both *in vitro* and *in vivo*[48-50]. Researchers developed HA-based scaffolds, and HA-based coatings on metallic substrates for orthopedic device applications for few decades. This chapter will summarize different

processes of synthesizing HA particles, biological properties of HA, as well as current and potential applications of HA in orthopedic devices.

2. Synthesis of HA particles

Both in laboratory and industry, HA particles can be produced in different processes, as indicated in the tree diagram of Figure 15.

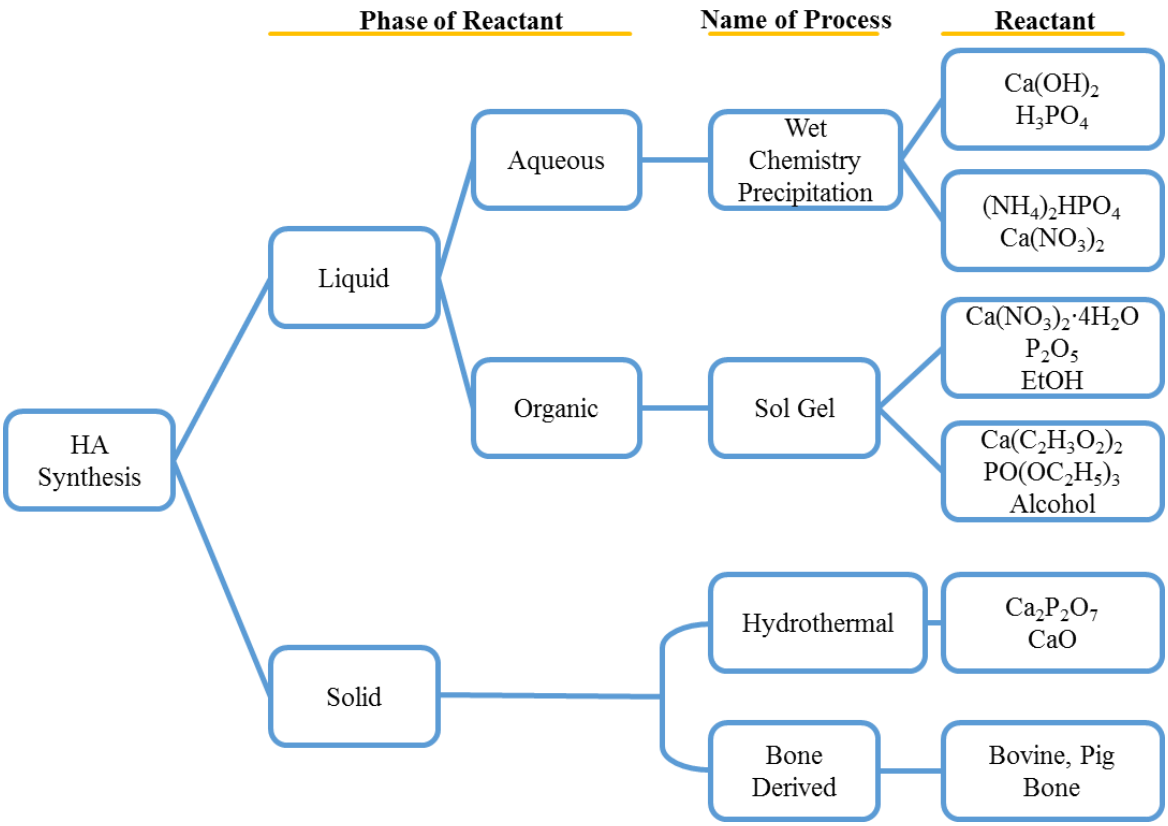

Figure 15. Tree diagram for different synthesis processes of HA particles.

Wet chemistry precipitation followed by hydrothermal treatment is a widely used method to produce HA particles[51-52]. This method involves the addition of phosphate ions solution to a calcium ion solution to precipitate HA. Various reactions can be applied to obtain HA through wet chemistry precipitation. One common reaction to be followed is Eq. (1):

$$10Ca(NO_3)_2 + 6(NH_4)_2HPO_4 + 8NH_4OH \rightarrow Ca_{10}(PO_4)_6(OH)_2 + 6H_2O + 20NH_4NO_3 \quad (1)$$

This reaction adds a calcium nitrate [$Ca(NO_3)_2$] solution dropwise to a diammonium hydrogen phosphate [$(NH_4)_2HPO_4$] solution at a constant temperature[53]. Ammonium hydroxide [NH_4OH] is used to maintain the pH above 10 during the reaction. The addition of the calcium nitrate yields the precipitation of a calcium phosphate, which is subsequently centrifuged, washed several times, resuspended and then hydrothermally treated. After the hydrothermal treatments, HA is collected and dried under vacuum, and ground with a mortar and pestle to obtain a fine powder[53].

For wet chemistry precipitation approaches, varying reaction parameters, such as temperature and reaction time, can affect the properties of the final HA particles. For example, increasing the reaction time at room temperature resulted in size reducing of the HA particles[54]. Particle size of HA can also be influenced by the temperature, where raising it leads to larger HA particles[55]. On the other hand, raising the temperature can also lead to a needle-shaped morphology, while lowering it causes the particle morphology to become more spherical[56].

3 HA particles properties

3.1 Biological properties and functions of HA particles

Osteoconductivity is the ability of bone cells to attach and grow on the surface or grow into the pores/channels of a biomaterial, which is a desired property for orthopedic implants[57]. Adsorption of protein on the surface of a material is the initial step of cell-biomaterial interaction. Proteins, such as albumin, can be adsorbed to the surface of HA

particles[58-59]. In addition, HA particles showed enhancement in adsorption of fibronectin and vitronectin on the composites scaffold[60]. Secondly, the presence of HA can facilitate osteoblast adhesion and proliferation *in vitro*, which is an indication of good osteoconductivity[50, 61]. Moreover, HA particles have also shown osteoinductivity, which is the ability of a material to induce stem cells to differentiate and develop into mature bone cells[57]. Liu et al indicated that nano-phase HA could promote the differentiation of mesenchymal stem cells into osteogenic cells[62].

3.2 Size effect

By adjusting synthesis parameters, nano and micron size HA particles can be produced. Significant differences were found between different sizes of HA particles. Gou et al. found that HA nanoparticles were more efficient in the adhesion and proliferation of human primary osteoblast cells than micron particles[63]. Additionally, HA nanoparticles improved mineralization more than HA micron particles, which is important for bone regeneration[63]. These findings paralleled those by Webster et al., where it was found that a ceramic's grain size was inversely related to the adhesion of osteoblasts[50]. These results may attribute to the fact that nano size HA resemble the natural mineral in bone more closely than its micron size counterpart[64].

Significant differences have also been found within the nanoscale level as well. Cai et al. synthesized HA nanoparticles of three different diameters (20 ± 5, 40 ± 10 and 80 ± 12 nm) and conducted an *in vitro* study using mesenchymal stem cells (MSCs) and osteosarcoma cells (U2OS). It was found that a smaller HA nanoparticle size increased proliferation of MSCs but decreased proliferation of U2OS cells[64]. Shi et al. also indicated

that smaller nano size of HA nanoparticles increased the proliferation of human osteoblast-like cells[61]. It was speculated that decreasing HA nanoparticle size will increase their penetration of the cell membrane and probability of inducing a response from the cell, i.e. proliferation and growth[61, 64].

3.3 Morphology effect

Different morphologies of HA particles can also affect its property significantly. Zhao et al. indicated that nanophase HA with spherical and rod shape resulted in significantly less cell death after culture with human bronchial epithelial cell, compared that of nanophase HA with needle and plate shape[65]. Conversely, no significant cell death was recorded in mouse macrophage cell culture when exposed to any of the nanophase HA groups[65]. Furthermore, Shi et al. examined the effect of two different types of morphologies (rod- and sphere-like) on human osteoblast-like (MG-63) cells. Sphere-like HA nanoparticles induced higher proliferation of MG-63 cells than rod-like HA nanoparticles[61]. Similarly, Zhao et al. showed that a spherical shape of HA nanoparticles caused greater adhesion and proliferation of osteoblasts than rod-like nanoparticles. This may be due to the fact that sphere-like nanoparticles had higher surface area than the rod-like nanoparticles[66].

4. Nano-HA as coating materials

Nanostructured hydroxyapatite (nHA) is found in natural bone and accounts for 70% of dry weight of human cortical bone[67]. It shows excellent biocompatibility, bioactivity, and osteoconductivity[68-69]. Special properties of nHA, such as nano-scale grain size and surface feature, are shown to increase osteoblast adhesion and long-term functions (e.g.

calcium mineral deposition), as compared with micron-scale hydroxyapatite (HA)[54, 68]. HA is widely used as a bone grafting material or as a coating to promote bone ingrowth to implants. The brittleness of HA limits its applications in load bearing conditions, and there are still ongoing research efforts on developing HA as a scaffold for load bearing applications, using freeze casting [70] and high temperature sintering[71]. Hydroxyapatite (HA) is a biodegradable ceramic, which resembles the chemical properties of the inorganic component of human bone[72]. Aside from its biocompatibility, the osteoconductive and osteoinductive abilities make synthetic HA favorable for biomedical applications[73-74]. Due to its brittleness, HA itself is limited for load-bearing conditions in musculoskeletal applications[75]. However, HA particles can be used as a bioactive coating material for load-bearing implants, which are promising to reduce the degradation rate and promote osteointegration of the Mg-based implants[76]. Nanophase hydroxyapatite (nHA) resembles the inorganic component of bone and thus is considered as an attractive coating material for skeletal implants[75]. In particular, nHA has been known for promoting adhesion and proliferation of osteoblasts (i.e., bone-forming cells)[54] and osteogenic functions of bone marrow derived mesenchymal stem cells[77], which is beneficial for bone healing.

In a summary, HA will be an important research topic as a biocompatible and bioactive coating material for orthopedic device applications. Wet chemistry precipitation can produce highly crystallized HA but limited quantity. Biocomposite coatings are more promising than the single phase HA in terms of tunable mechanical properties and improved bioactivity.

Chapter 6 Single-Phased Hydroxyapatite Coated Magnesium-Based Implant for Musculoskeletal Applications

1. Introduction

Protective and bioactive HA coatings applied to Mg substrates can potentially control the degradation rate and lead to more bio-functional Mg-based implants[1, 78]. The objective of this study is to fully characterize and evaluate HA coated Mg for potential medical implant applications. Characterizing the surface of the implants, such as topography and phase composition, provide detailed information of the interface between the Mg substrate and the surrounding physiological environment. Immersion of nHA and mHA coated Mg in revised simulated body fluid (rSBF) identified the degradation behavior of the implants *in vitro* and effects to the local environment, which may predict *in vivo* behaviors of the implants as well. The loss of compressive strength and Young's modulus of coated Mg after degraded for six weeks help to estimate the mechanical strength of the implants *in vivo*.

2. Materials and Methods

2.1 Sample Preparation

Pure Mg (Goodfellow Corporation, Coraopolis, PA) disks with a diameter of 7.5 mm and a height of 1 mm, and pure Mg rods with a diameter of 7.5 mm and a height of 15 mm were cleaned in ethanol for 10 min using ultrasonic bath before deposition. Nano size (nHA) and micron size (mHA) [$Ca_{10}(PO_4)_6(OH)_2$] particles (Himed, Old Bethpage, NY) were deposited on all the surfaces of the Mg disks and rods using the transonic particle acceleration (TPA) deposition process, also known as IonTite. TPA is a proprietary inhouse coating process at N2 Biomedical (formerly Spire Biomedical Inc.) for depositing thin

films of ceramics and other materials onto surfaces at low temperature and under precisely controlled conditions[40]. In order to find an optimal deposition process for nHA and mHA coatings on Mg, different pressures were applied during the TPA deposition process. Specifically, nHA_100 and mHA_100 were produced using a low deposition pressure, and nHA_400 and mHA_400 were produced using a high deposition pressure. Pure Mg substrates without HA coating were included as control. In addition, different geometry of all the samples, i.e., Mg disks (7.5 mm × 1 mm) and Mg rods (7.5 mm × 15 mm), were prepared to mimic the dimension of a plate and a craniofacial screw.

2.2 Characterization of the samples after deposition

The nHA_100, nHA_400, mHA_100, mHA_400, and Mg control were mounted on a flat SEM holder (Ted Pella) using double-sided copper tape and sputter coated with platinum/palladium at 20 mA for 60 seconds. The microstructures of nHA_100, nHA_400, mHA_100, mHA_400, and Mg control were examined under a scanning electron microscope (SEM; Nova NanoSEM 450, FEI Inc.) at high vacuum mode. The size distributions of hydroxyapatite particles of the coatings after deposition were determined based on SEM images using the ImageJ analysis tools. Specifically, individual particles were manually outlined using ImageJ to measure the size and calculate the distribution. The surface elemental compositions of the samples were determined using energy dispersive x-ray spectroscopy (EDS; Aztec, Oxford instrument) at an acceleration voltage of 20 kV. Cross-sections of the coatings were prepared by polishing off the coating on the top of the cylindrical samples and then mounted onto a SEM holder using double-sided

copper tape. The thickness of the coatings was determined based on the SEM images of cross-sections using ImageJ analysis tools.

The compressive strength of different Mg-based rods, i.e., nHA_100, nHA_400, mHA_100, mHA_400, and Mg control with a geometry of 7.5 mm × 15 mm, was obtained using compression testing system (5969, Insrton, Norwood, MA). Specifically, a constant strain rate of 1 mm/min was applied on the samples, and load stopped at the final strain displacement of 6 mm. The stress-strain curved for each sample was plotted in graph, and the ultimate compressive strength, maximum load and Young's modulus of each sample was calculated accordingly.

2.3 In vitro degradation and characterization of the samples by immersion study

The degradation behaviors of Mg disks (7.5 mm × 1 mm) and Mg rods (7.5 mm × 15 mm), i.e., nHA_100, nHA_400, mHA_100, mHA_400, and Mg control, were investigated using immersion methods in rSBF. Before immersion, all samples were weighed and sterilized under ultraviolet (UV) radiation for 4 hours. Both the Mg disks and Mg rods were first placed into the wells of 12 well tissue culture plates, and 3 ml of rSBF was added to each well. Until reaching the prescribed time points, the samples were incubated in rSBF under a standard cell culture condition (a sterile, 37ºC, 5% CO_2/95% air, and humidified environment). The prescribed time points were 12 hrs, 24 hrs, 48 hrs, 72 hrs, 1 week, 2 weeks, 4 weeks and 6 weeks.

After each time point, rSBF was collected from the wells, and the samples were dried at 37 ºC with a duration of 24 hours for Mg disks and 72 hours for Mg rods (large surface area). The dried samples were then weighed, photographed, and the mass change

was calculated. Specifically, the mass of the samples (M_i) after each incubation time was divided by its initial mass (M_0) to obtain the mass change (M_i/M_0). The pH of the media was measured using a pH meter (SB70Pm, SympHony, VWR). The pH increase of Mg-based samples, i.e., $pH_{(+)}$, was obtained by subtracting the baseline $pH_{(rSBF)}$, i.e., the pH of rSBF, from the pH of the media cultured with each sample, $pH_{(sample)}$, i.e., $pH_{(+)} = pH_{(sample)} - pH_{(rSBF)}$.

The Mg^{2+} and Ca^{2+} ion concentrations were quantified using inductive coupled plasma - optical emission spectrometry (ICP-OES; Optima 8000, Perkin Elmer, Waltham, MA, USA). Briefly, the collected solutions from each well were diluted with DI water by a factor of 1:100 into a total volume of 10 ml. Mg^{2+} ion concentrations were then obtained from a calibration curve generated using Mg^{2+} standards (Perkin Elmer) serially diluted to a concentration of 0.5, 1, 2, and 5 mg/L. Similarly, Ca^{2+} ion concentrations were then obtained from a calibration curve generated using Ca^{2+} standards (Perkin Elmer) serially diluted to a concentration of 0.05, 0.5, and 5 mg/L. The increase of Mg^{2+} ion concentration in media after cultured with Mg-based samples, i.e., $C_{(Mg, +)}$, was obtained by subtracting the baseline $C_{(Mg, rSBF)}$, i.e., the Mg^{2+} ion concentration of rSBF, from the measured Mg^{2+} ion concentration of the media cultured with each sample, $C_{(Mg, sample)}$, i.e., $C_{(Mg, +)} = C_{(Mg, sample)} - C_{(Mg, rSBF)}$. The decrease of Ca^{2+} ion concentration in media after cultured with Mg-based samples, i.e., $C_{(Ca, -)}$, was obtained by subtracting the Ca^{2+} ion concentration of the media cultured with each sample, $C_{(Ca, sample)}$, from the baseline $C_{(Ca, rSBF)}$, i.e., the Ca^{2+} ion concentration of rSBF, i.e., $C_{(Ca, -)} = C_{(Ca, rSBF)} - C_{(Ca, sample)}$. After the characterization, these samples were then placed into 3 ml of fresh rSBF solution and incubated till the next

prescribed time point. This characterization process was repeated for each prescribed time point. The degradation tests were performed in triplicate for each sample type.

After 6 weeks of immersion, all samples, including Mg disks (7.5 mm × 1 mm) and Mg rods (7.5 mm × 15 mm), were dried and placed on a conductive copper tape and sputter coated for SEM imaging and EDS analysis as described previously. The degradation products on the Mg rods (7.5 mm × 15 mm) were scratched off and collected for examining the phase and crystal structure. Specifically, the phases of the degradation products were determined using X-ray diffraction (XRD; Empyrean, PANalytical) at 45 KV and 40 mA with 2θ angles from 10° to 80º at a step size of 0.002º. The diffraction peaks were identified based on the international center for diffraction data (ICDD) database using HighScore software (PANAlytical). The chemical bonding structures of the degradation products were determined using Fourier transform infrared spectroscopy (FTIR, Optical 8000, Bruker) at the reflective mode. The compressive strength of Mg rods (7.5 mm × 15 mm) after immersion of 6 weeks in rSBF was also measured using Instron as previously described. The ultimate compressive strength, maximum load and Young's modulus of each sample after 6 weeks of immersion were calculated based on the stress and strain curves.

3. Results

3.1 Surface characterization and coating thickness of the samples

The microstructures of nHA_100, nHA_400, mHA_100, mHA_400, and Mg control were characterized by SEM analysis, as indicated in Figure 16. The nHA_100 and nHA_400 showed a full coverage of the Mg substrates. The nHA_100 and nHA_400 coatings were composed of two distinctive features. The first type of features was a flat

layer with spherical-like particles embedded, as indicated in the orange square in Figure 16a2. This feature was possibly formed by continuous pressure on the initially deposited HA nanoparticles, which compressed the particles into a flat layer. The second type of features was the propagation of HA nanoparticles on the surface of the coating layer, as indicated by the orange arrow in Figure 16a2. The HA coatings on mHA_100 and mHA_400 fully covered the Mg substrates, which showed irregular shape of HA particles after the deposition. Mg control without coating showed a flat surface with several cracks produced by the manufacturing process (Figure 16c). The EDS analysis confirmed the presence of Ca, P and O in coating of nHA_100, nHA_400, mHA_100 and mHA_400, which corresponding with the HA particles as indicated in Figure 1d. In addition, a small amount of Mg was also found in the coated samples, where the nHA coating showed higher Mg than that of mHA coating. For Mg control, major peak of Mg was confirmed with limited amount of O which caused by oxidization.

The HA particles were found less than 200 nm in nHA_100, with a 25 % of the particles stayed in the range from 100 nm to 150 nm, as indicated in Figure 17a. For nHA_400, the HA particles were less than 250 nm with 18 % of the particles had a diameter of 150 nm to 200 nm. In mHA_100 coating, 30 % of HA particles had a diameter from 200 nm to 300 nm, as indicated in Figure 17b. In mHA_400 coating, 18 % of HA particles had a diameter from 500 nm to 600 nm. In general, HA particles in nHA coating were found smaller than those in mHA coating. In addition, the coating with higher pressure, i.e., nHA_400 and mHA_400, showed larger HA particles than those in their counterparts, i.e., nHA_100 and mHA_100.

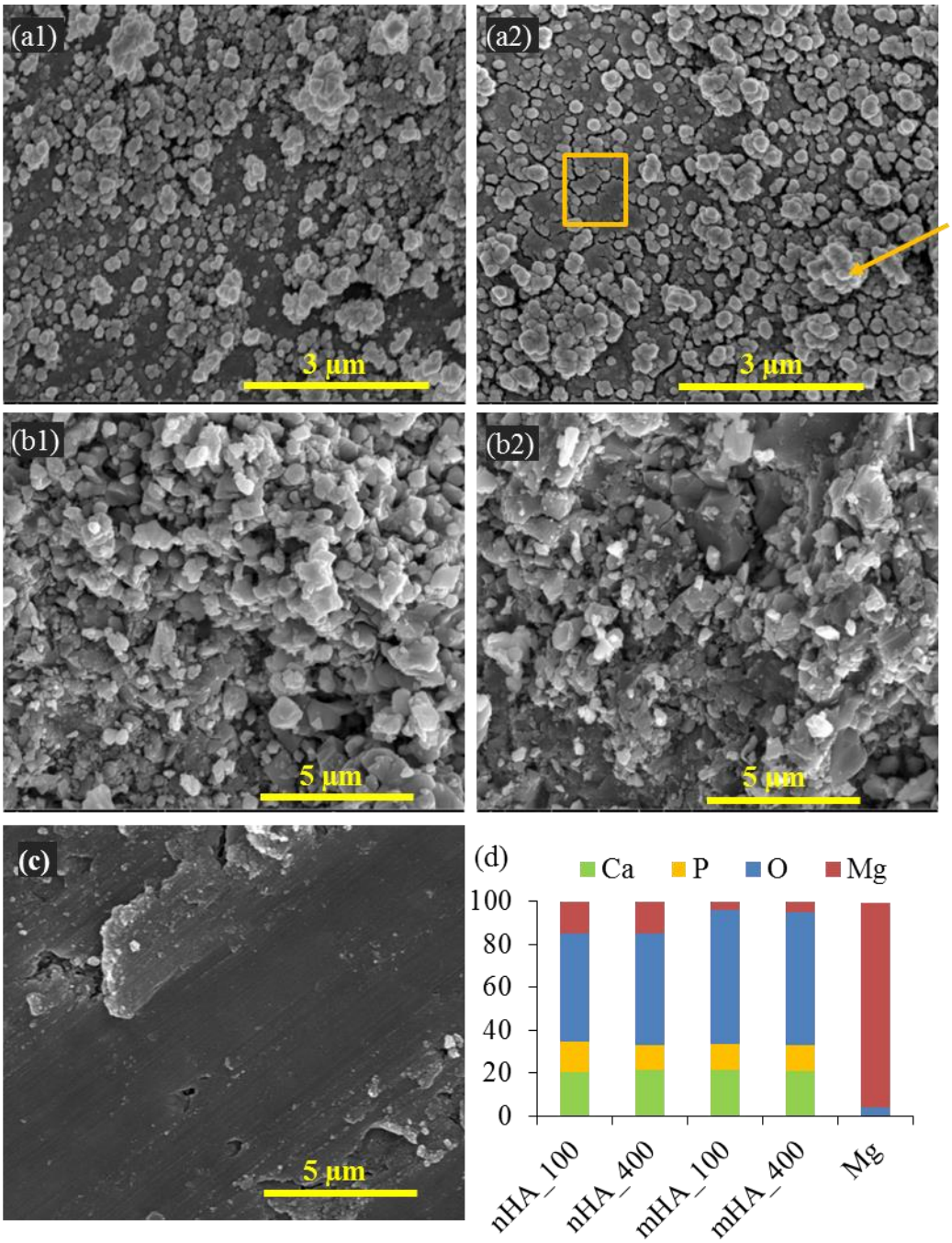

Figure 16 Surface topography and elemental composition of the nHA_100, nHA_400, mHA_100, mHA_400 coatings on Mg substrates, as well as Mg substrate without any coating. SEM images of (a1) nHA_100, (a2) nHA_400, (b1) mHA_100, (b2) mHA_400 and (c) Mg. The original magnification for nHA was 20,000x and for mHA, Mg was 10,000x. (d) Elemental composition (wt %) of all the samples.

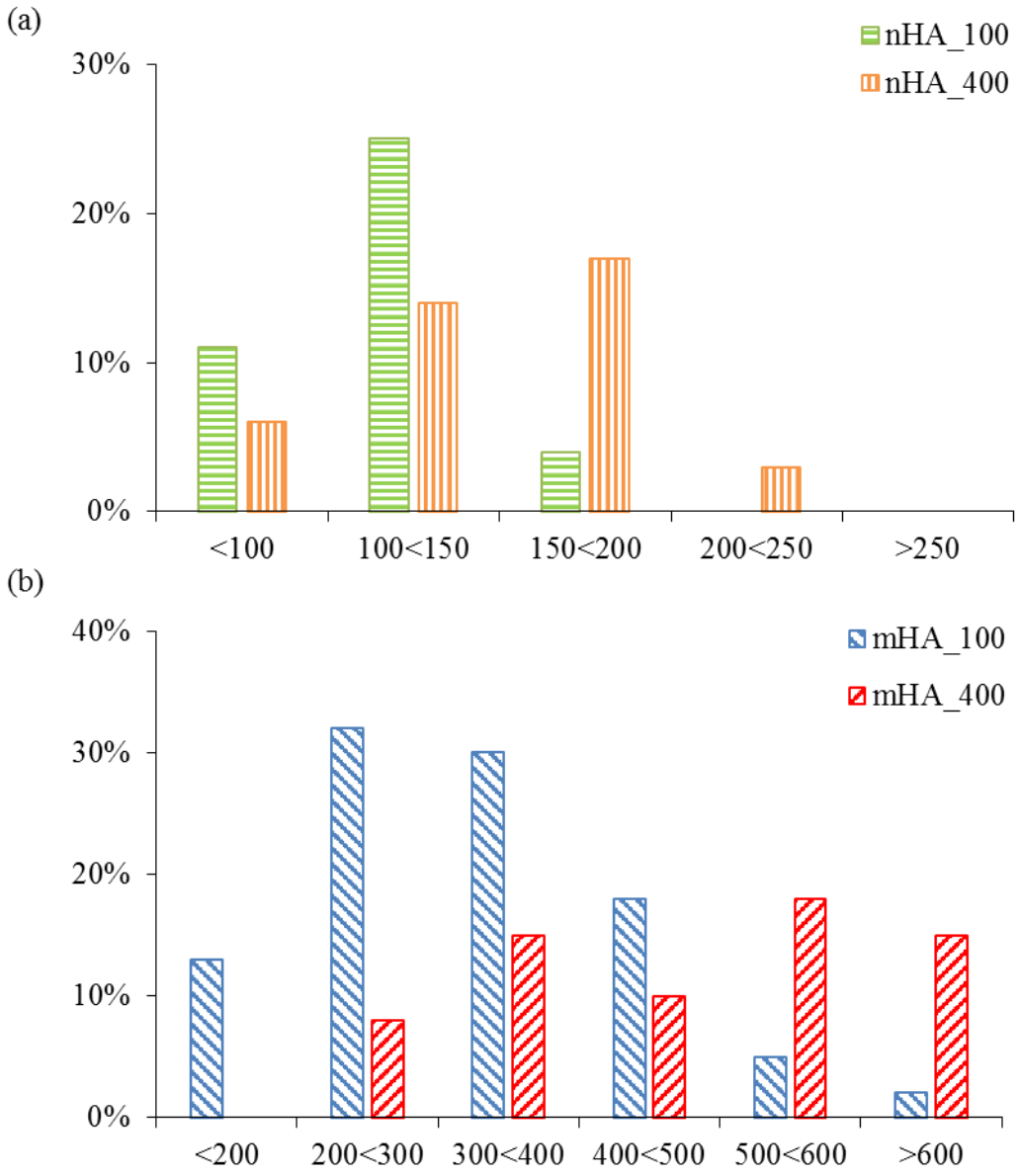

Figure 17 Size distributions of HA particles in (a) nHA_100, nHA_400 and (b) mHA_100, mHA_400 coatings on Mg substrates after TPA deposition. Unit of diameter: nm.

The SEM images of cross sections of nHA_100, nHA_400, mHA_100 and mHA_400 were summarized in Figure 18. For all the samples, the coating showed condensed coating without any obvious cracks at a magnification of 5,000x. The nHA_100,

nHA_400, mHA_100 and mHA_400 had coating thickness of 82.8 ± 7.3 µm, 143.8 ± 25.2 µm, 119.0 ± 10.9 µm and 116.4 ± 6.6 µm respectively.

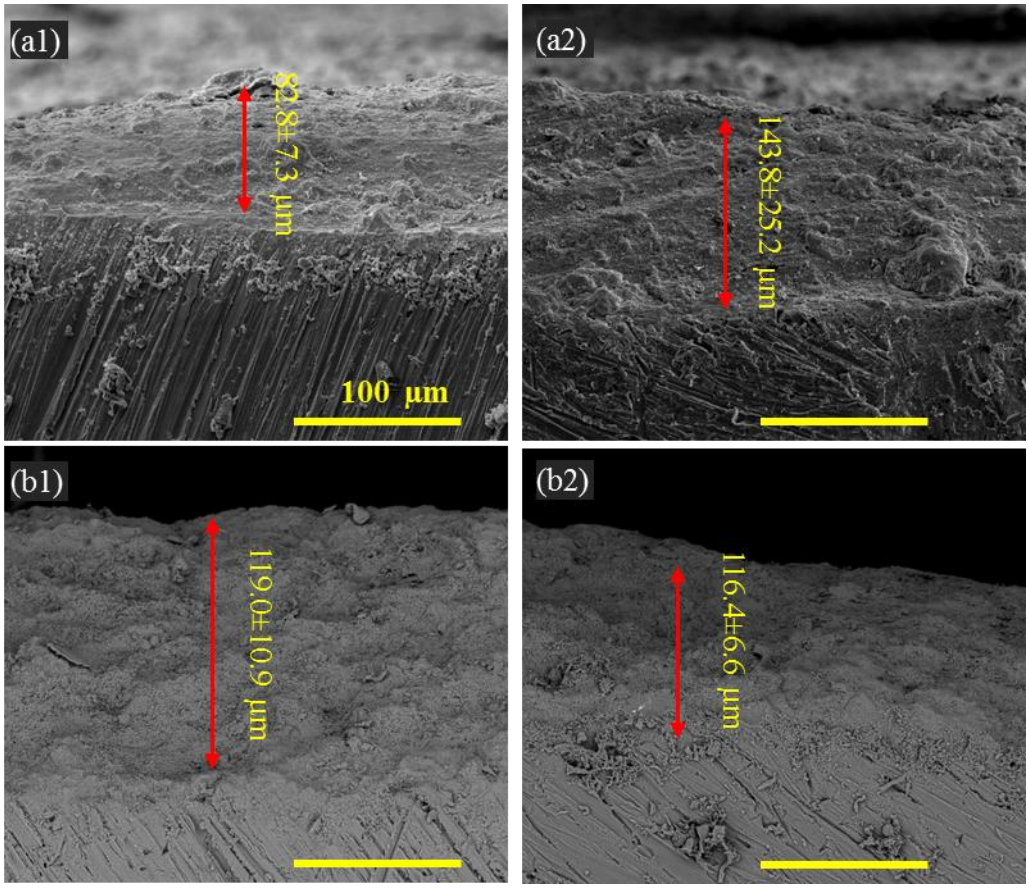

Figure 18 The cross sections of (a1) nHA_100, (a2) nHA_400 and (b1) mHA_100, (b2) mHA_400 coatings on Mg substrates after TPA deposition. The original magnifications for all images were 500x.

3.2 The in vitro degradation behavior of Mg Disks and Mg Rods in rSBF

3.2.1 Characterization of samples and degradation products after immersion

The macroscopic images of Mg disks, i.e., nHA_100, nHA_400, mHA_100, mHA_400, and Mg control with a geometry of 7.5 mm × 1 mm, at each prescribed time point during the 6 weeks immersion were summarized in Figure 19. All the samples showed continuous deposition of degradation products on the surface. Small crystal features started to form on the surface of all the samples at 1 week from observation by

human eyes, and the crystals accumulated more and grew larger during the rest of the immersion. The nHA_100 showed the most accumulation of the crystals after 6 weeks of immersion among all the samples. No obvious crack and penetration were observed on the surface of all the samples until 2 weeks. After 4 weeks of immersion, cracks were found on the edge of all the samples, and the cracks continuously developed during the rest of the immersion, which resulted irregular shape of Mg-based samples at the end of 6 weeks immersion.

The SEM images of Mg disks after 6 weeks immersion were indicated in Figure 20. All the Mg-based samples showed cracks after immersion, where the Mg control had the largest and the deepest cracks among all the samples. Crystal deposition products were found on the surface of nHA_100, nHA_400 and mHA_400, where the nHA_400 had the largest crystals. In nHA_400 and mHA_400 (Figure 20a2, b2), a white layer which was composed of small particles covered a large surface area of the samples. This white layer was possibly resulted from Ca/P deposition or remaining HA particles of the coating. The EDS analysis confirmed the presence of Ca, P, O, Mg and C in all the Mg-based samples. Interestingly, nHA_400 and mHA_400 had a higher content of Ca and P than all other samples, which indicated higher promotion of Ca/P deposition or longer preservation of HA coating during the immersion. Trace elements, sodium (Na) and potassium (K), were also found on all the Mg-based samples.

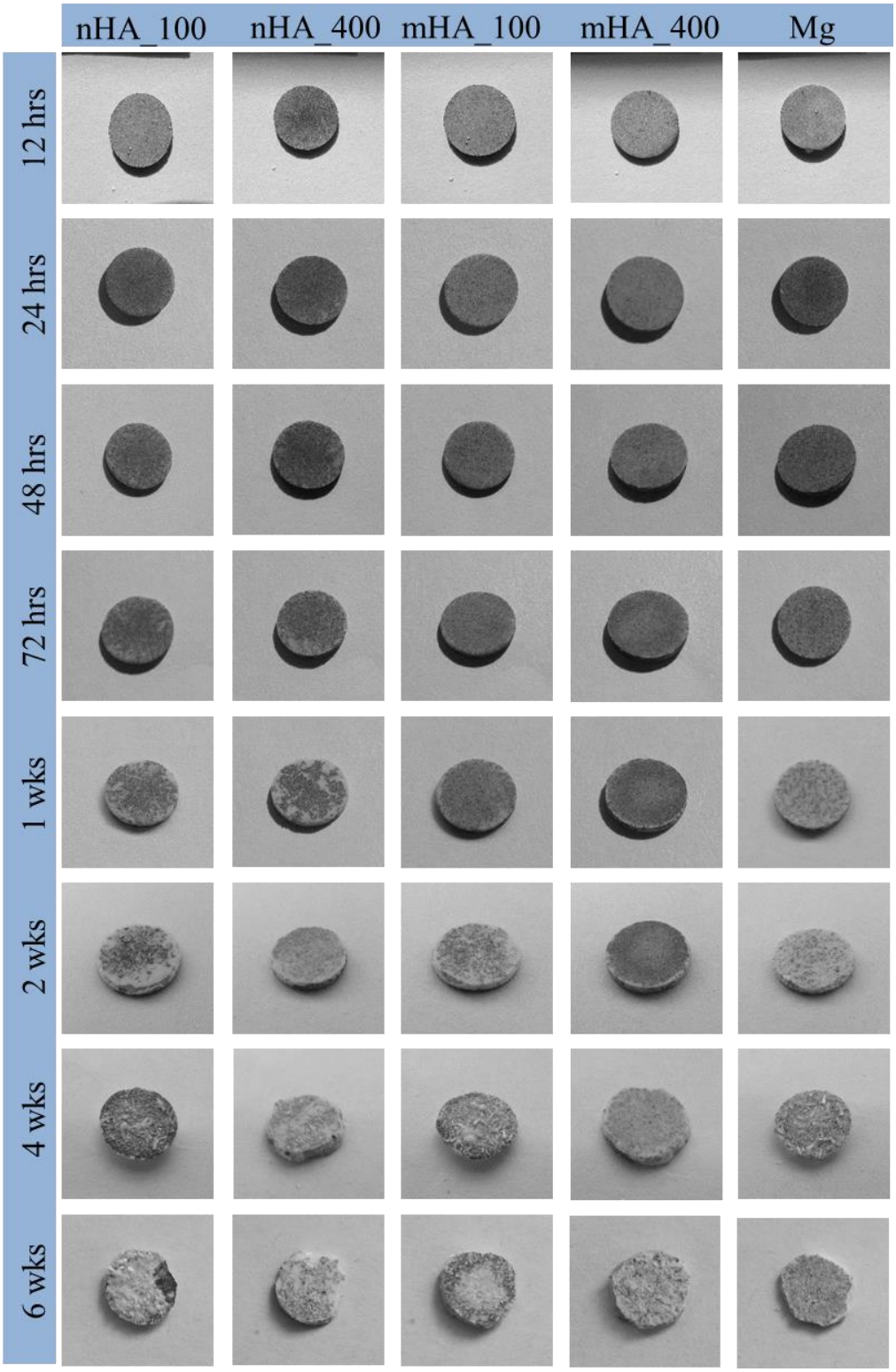

Figure 19 Macroscopic images of nHA_100, nHA_400, mHA_100, mHA_400 and Mg with a geometry of 7.5 mm × 1 mm at each prescribed time point during 6 weeks of immersion in rSBF.

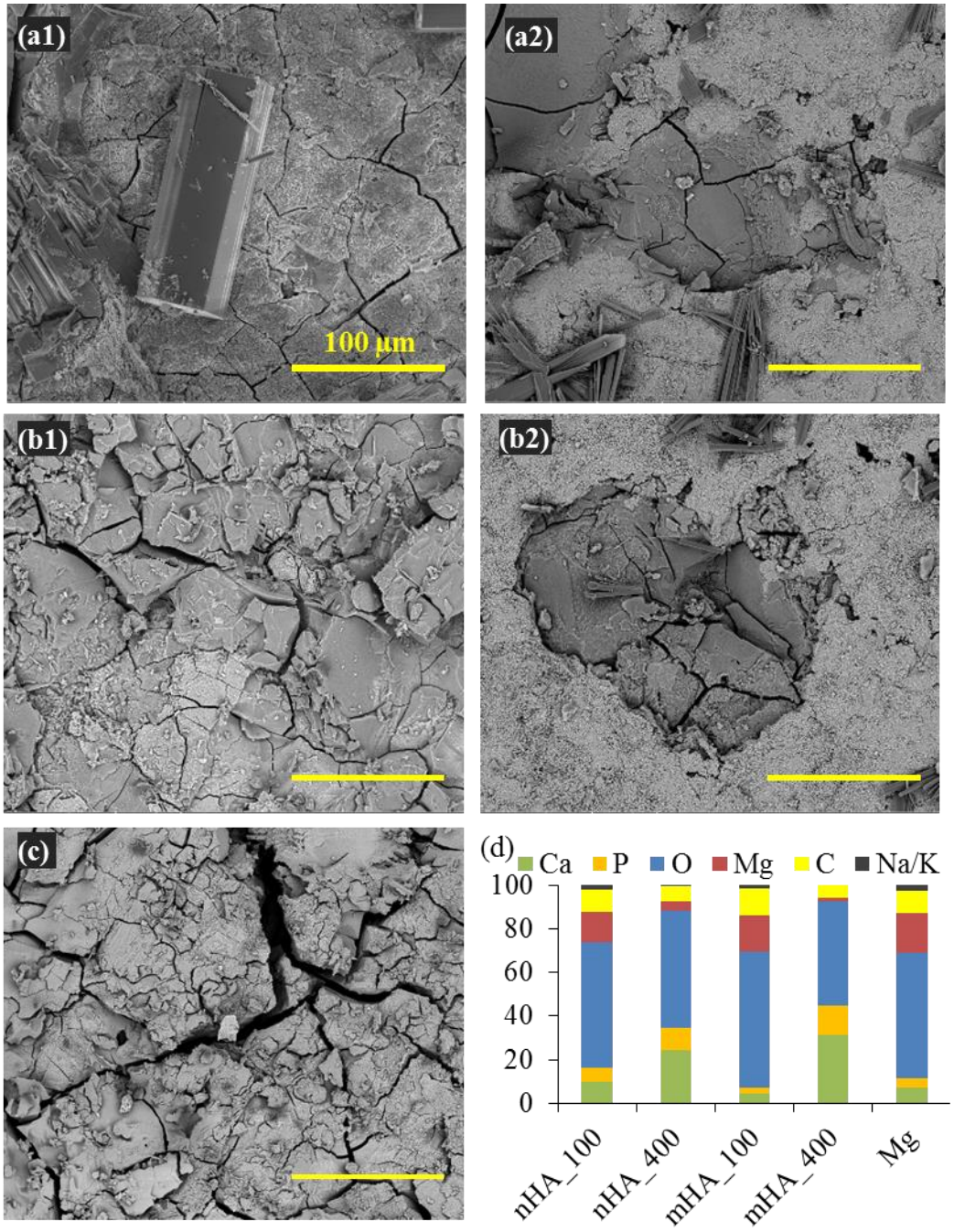

Figure 20 Surface topography and elemental composition of nHA_100, nHA_400, mHA_100, mHA_400 and Mg control with a geometry of 7.5 mm × 1 mm after immersion in rSBF for 6 weeks. SEM images of (a1) nHA_100, (a2) nHA_400, (b1) mHA_100, (b2) mHA_400 and (c) Mg. The original magnifications for all images were 500x. (d) Elemental composition (wt %) of all the samples after immersion.

The macroscopic images of Mg rods, i.e., nHA_100, nHA_400, mHA_100, mHA_400, and Mg control with a geometry of 7.5 mm × 15 mm, at each prescribed time

point during the 6 weeks immersion were summarized in Figure 21. All the samples showed continuous deposition of degradation products on the surface. Small crystal features started to form on the surface of all the samples at 72 hours from observation by human eyes, and the crystals accumulated more and grew larger during the rest of the immersion until week 6. No obvious crack and penetration were observed for all the samples except nHA_100 and Mg control. For these two samples, small cracks on the surface were observed at week 3 and continued to develop for the rest of the immersion until week 6.

The SEM images of Mg rods after 6 weeks immersion were indicated in Figure 22. The surface microstructures on the samples indicated formation of cubic shape crystals during the immersion in rSBF, which were consistent with previous macroscopic images. These crystals provided an almost full coverage of all the samples, except few spots of remaining HA coating as indicated by black arrow in Figure 22a1-a3. The EDS analysis confirmed the presence of Ca, P, O, Mg and C in all the Mg-based samples, as indicated in Figure 22d. Limited amount of Ca and P was found (< 2 % in weight). C was significantly higher than their counterparts in Mg disks (Figure 5d), which might come from the formed crystals.

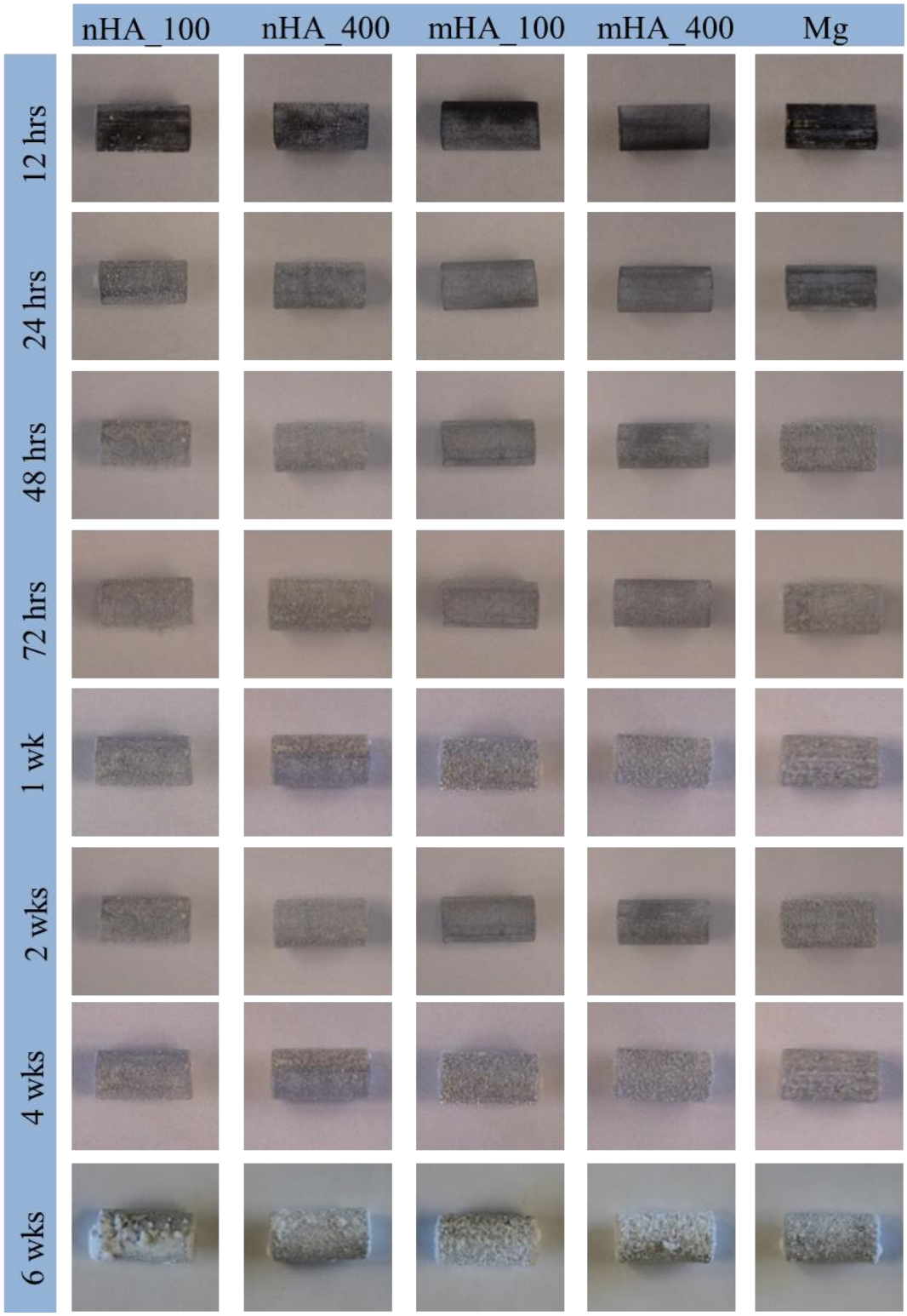

Figure 21 Macroscopic images of nHA_100, nHA_400, mHA_100, mHA_400 and Mg with a geometry of 7.5 mm × 15 mm at each prescribed time point during 6 weeks of immersion in rSBF.

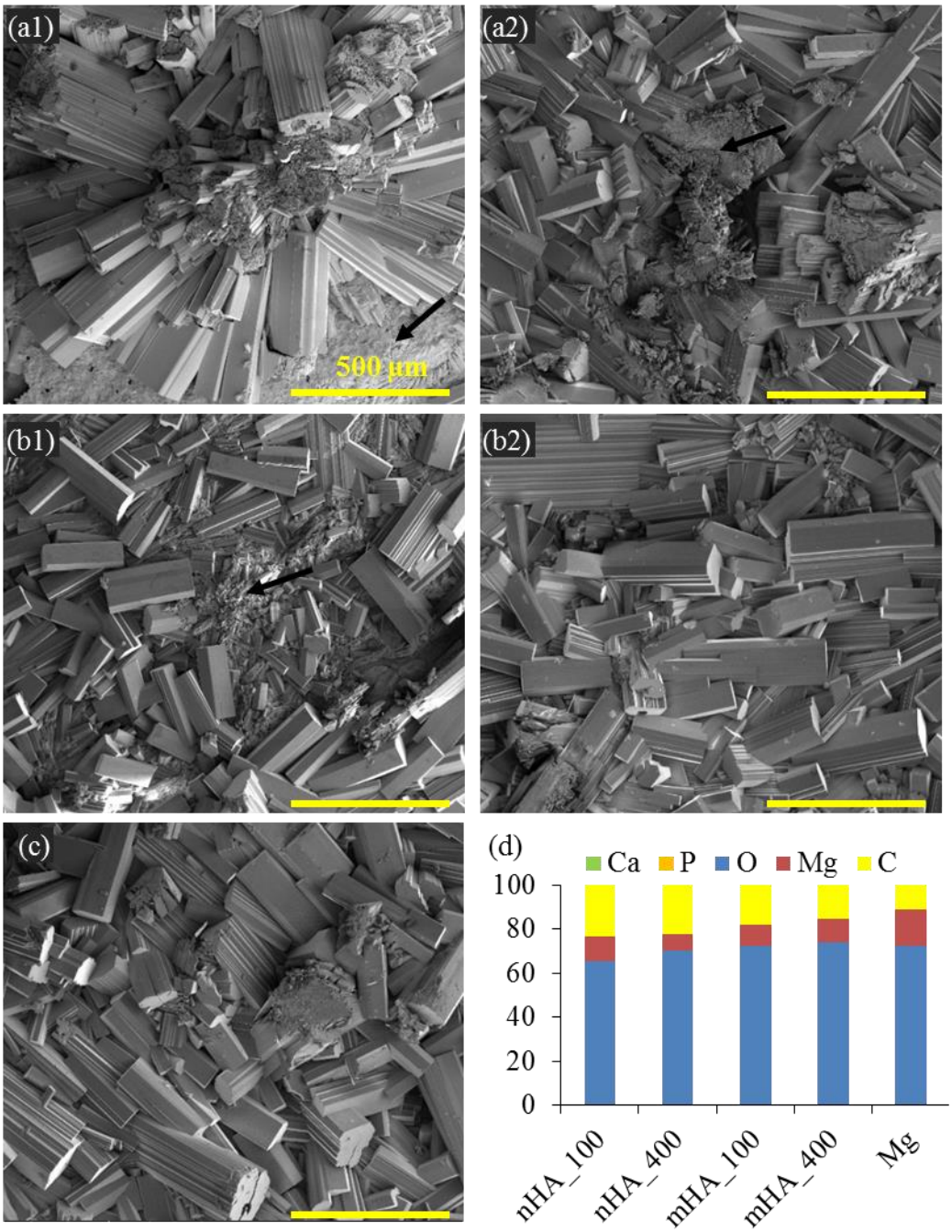

Figure 22 Surface topography and elemental composition of nHA_100, nHA_400, mHA_100, mHA_400 and Mg control with a geometry of 7.5 mm × 15 mm after immersion in rSBF for 6 weeks. SEM images of (a1) nHA_100, (a2) nHA_400, (b1) mHA_100, (b2) mHA_400 and (c) Mg. The original magnifications for all images were 500x. (d) Elemental composition (wt %) of all the samples after immersion.

The mass changes of Mg disks during the immersion, i.e., nHA_100, nHA_400, mHA_100, mHA_400, and Mg control with a geometry of 7.5 mm × 1 mm, were

summarized in Figure 23a. Starting at 24 hours, all the samples showed decrease of mass during the 6 weeks immersion. The nHA_400 and mHA_400 showed the smallest mass loss among all the samples, followed by nHA_100 and mHA_400. Mg control had the largest mass loss with only 60 % mass remaining at the end of the immersion. The mass changes of Mg rods, i.e., nHA_100, nHA_400, mHA_100, mHA_400, and Mg control with a geometry of 7.5 mm × 15 mm, were summarized in Figure 23b. The continuous deposition of degradation products increased the mass of all the samples by 4% in average after 6 weeks immersion. After immersion of 24 hours, all the samples had insignificant mass change compared with the initial mass. After 48 hours, 2% mass increase was observed on mHA_100 and mHA_400 while nHA_100, nHA_400 and Mg remained similar mass compared with the initial. After 1 week immersion, all the samples showed significant increase of mass, where nHA_100 and nHA_400 had more mass gain than the mHA_100, mHA_400 and Mg control.

Different geometries of Mg-based implants, i.e., disks and rods, showed significant differences in degradation morphology and mass change during 6 weeks immersion in rSBF. Mg disks showed partial coverage of degradation products, and typical degradation morphology of bare Mg, i.e., cracks. Mg rods, however, were fully covered by the crystal degradation products. Regarding the mass change, Mg disks showed continuous mass loss, while Mg rods showed continuous mass gain during the 6 weeks immersion.

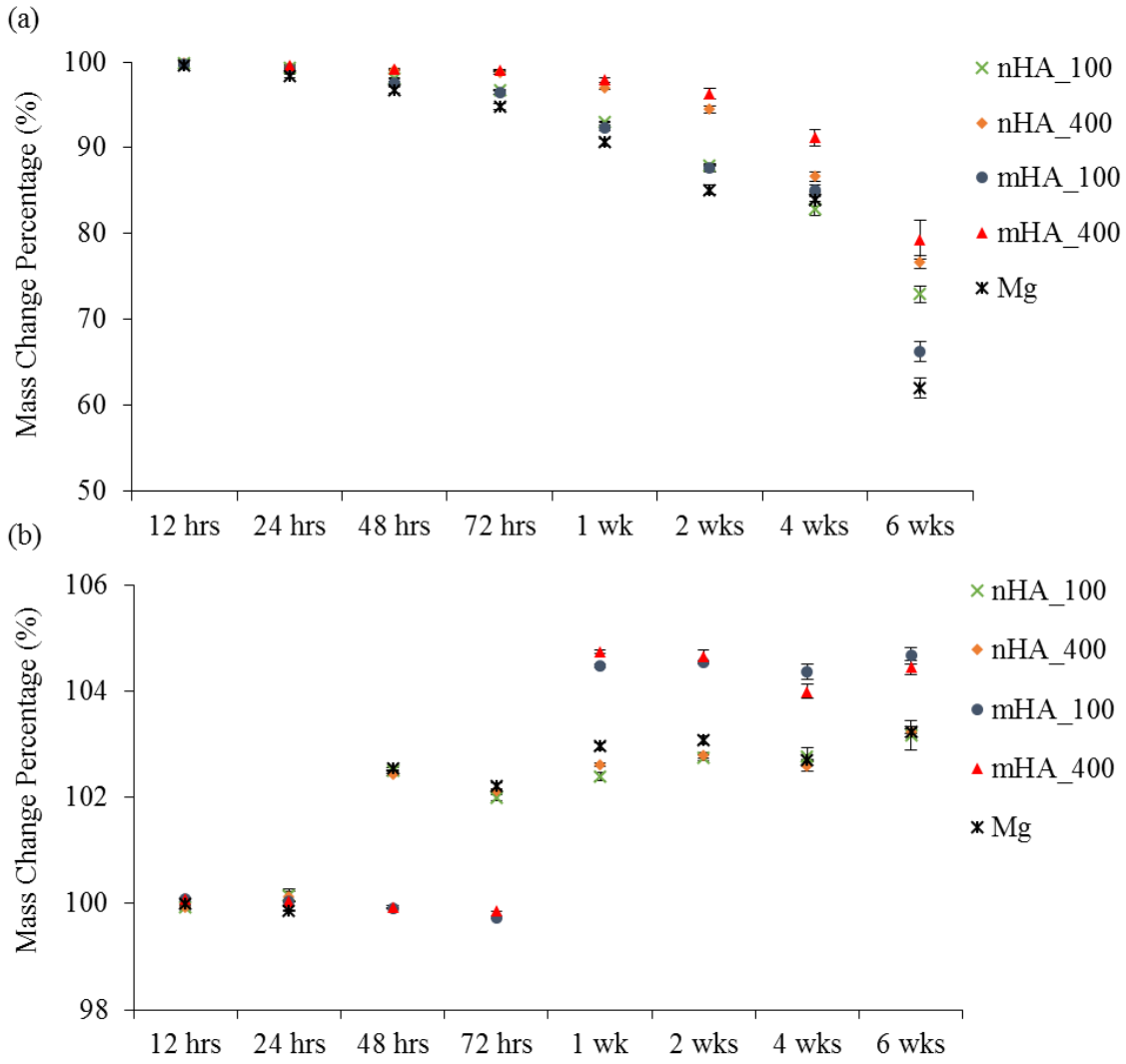

Figure 23 The mass change (final/initial) of nHA_100, nHA_400, mHA_100, mHA_400 and Mg control at different culture time point during the immersion in rSBF for 6 weeks. (a) Mass change of each sample with a geometry of 7.5 mm × 1 mm. (b) Mass change of each sample with a geometry of 7.5 mm × 15 mm. Data are mean ± standard error (N=3).

3.2.2 Post-media Analysis after *In Vitro* Culture with Mg-based Samples

The normalized pH of the media, i.e., increase of pH, was summarized in Figure 24a after culture with Mg disks, i.e., nHA_100, nHA_400, mHA_100, mHA_400, and Mg control with a geometry of 7.5 mm × 1 mm. Each group showed significant increase of pH at different time points during the 6 weeks immersion. In general, nHA_400 and mHA_400

showed lower increase of pH than all other samples until 2 weeks. After 4 weeks, all the samples showed a similar increase of pH with no significant difference. Similar with pH, each group showed a significant increase of Mg^{2+} ion concentration at different time points during the 6 weeks immersion (Figure 24b). In general, mHA_100 and mHA_400 showed lower increase of Mg^{2+} ion concentration than all other samples until 1 week. Interestingly, nHA_100, nHA_400 and Mg showed the highest increase of Mg^{2+} ion concentration at 1 week than their counterparts in all other time points. After 2 weeks, all the samples showed a similar increase of Mg^{2+} ion concentration with no significant difference. On the contrary with pH and Mg^{2+} ion concentration, each group showed a significant decrease of Ca^{2+} ion concentration at different time points during the 6 weeks immersion (Figure 24c). The nHA_100, nHA_400 and Mg showed the highest decrease of Ca^{2+} ion concentration at 1 week than their counterparts in all other time points. In general, mHA_100 and mHA_400 showed lower decrease of Ca^{2+} ion concentration than all other samples until 2 weeks. After 4 weeks, all the samples showed a similar decrease of Ca^{2+} ion concentration with no significant difference. Interestingly, the increase of Mg^{2+} ion concentration was linearly corresponding to the decrease of Ca^{2+} ion concentration in all the samples at all-time points. Specifically, the higher the increase of Mg^{2+} ion concentration, the higher decrease of Ca^{2+} ion concentration and vice versa.

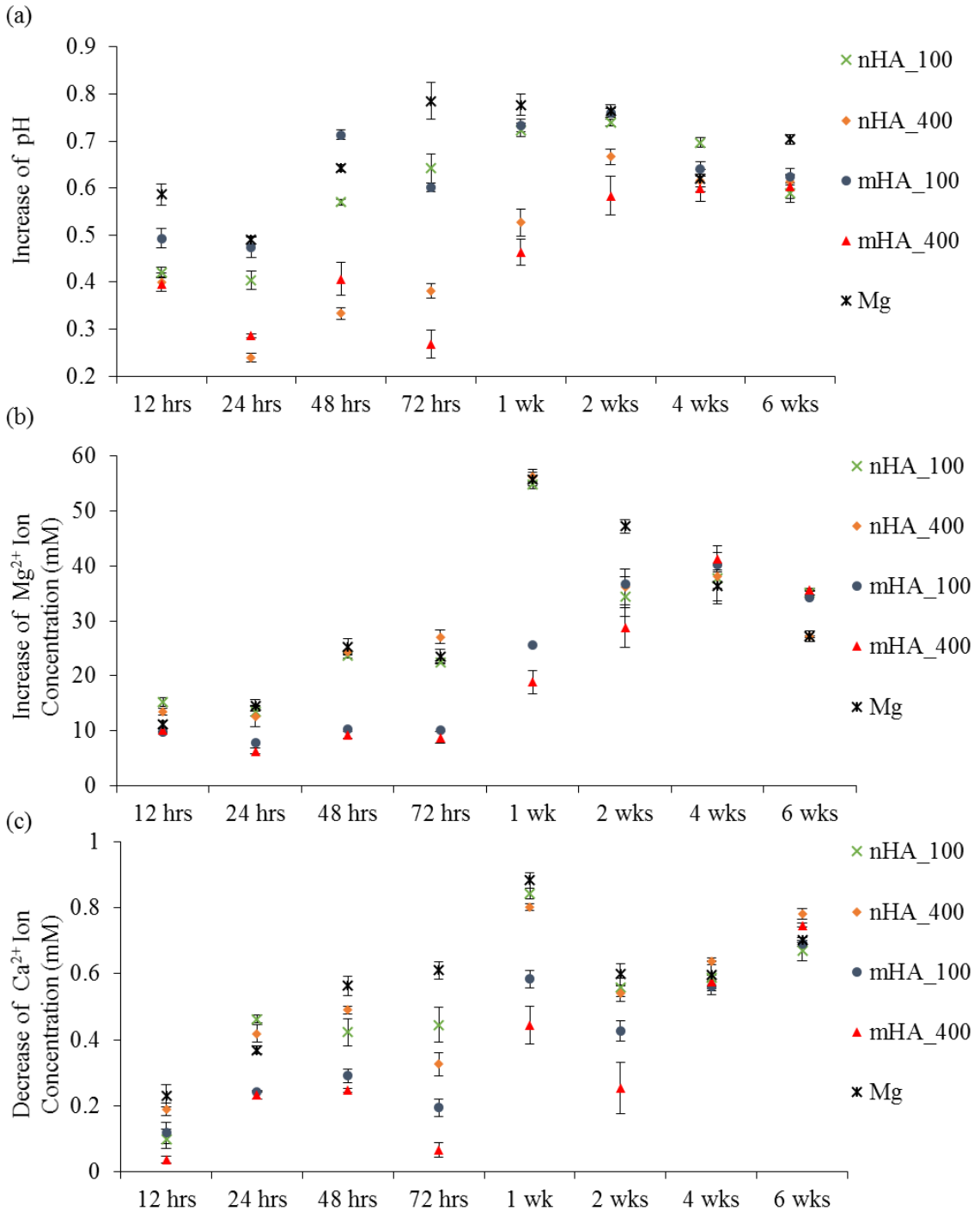

Figure 24 The post-media analysis at different culture time point after immersed nHA_100, nHA_400, mHA_100, mHA_400 and Mg control with a geometry of 7.5 mm × 1 mm in rSBF for 6 weeks. (a) The pH increase of collected rSBF after cultured with each sample at different time point. (b) Mg^{2+} ion concentration increase of collected rSBF after cultured with each sample at different time point. (c) Ca^{2+} ion concentration decrease of collected rSBF after cultured with each sample at different time point. Data are mean ± standard error (N=3).

The normalized pH of the media, i.e., increase of pH, was plotted in Figure 25a after culture with Mg rods, i.e., nHA_100, nHA_400, mHA_100, mHA_400, and Mg control with a geometry of 7.5 mm × 15 mm. At each time point, the Mg-based substrates showed a significant increase of pH, but no significant difference were found between the Mg-based samples. Similarly with the pH, Mg-based rods had a significant increase of Mg^{2+} ion concentration at all-time points, but no significant difference were detected when comparing among the Mg-based substrates (Figure 25b). The Ca^{2+} ion concentration had a significant decrease when culture with all the Mg-based substrates which indicated a precipitation and deposition of Ca^{2+} on the surface of Mg-based substrates (Figure 25c). Significant difference was not found when comparing each Mg-based substrates regarding the decrease of Ca^{2+} ion concentration. Interestingly, the decrease of Ca^{2+} ion concentration was significantly reduced after 4 weeks of immersion, which might reach the saturation of the Ca^{2+} ion deposition.

Different geometries of Mg-based implants, i.e., disks and rods, had significantly different effects on pH and ion change of the rSBF during 6 weeks immersion. In general, Mg disks had significant less pH increase, Mg^{2+} ion releasing, and Ca^{2+} ion deposition. This was resulted because Mg disks had significant less surface area than that of Mg rods. At week 4 and week 6, however, the deposition of Ca^{2+} ion on Mg disks was higher than that of Mg rods, which due to the saturation of the Ca^{2+} ion deposition on Mg rods.

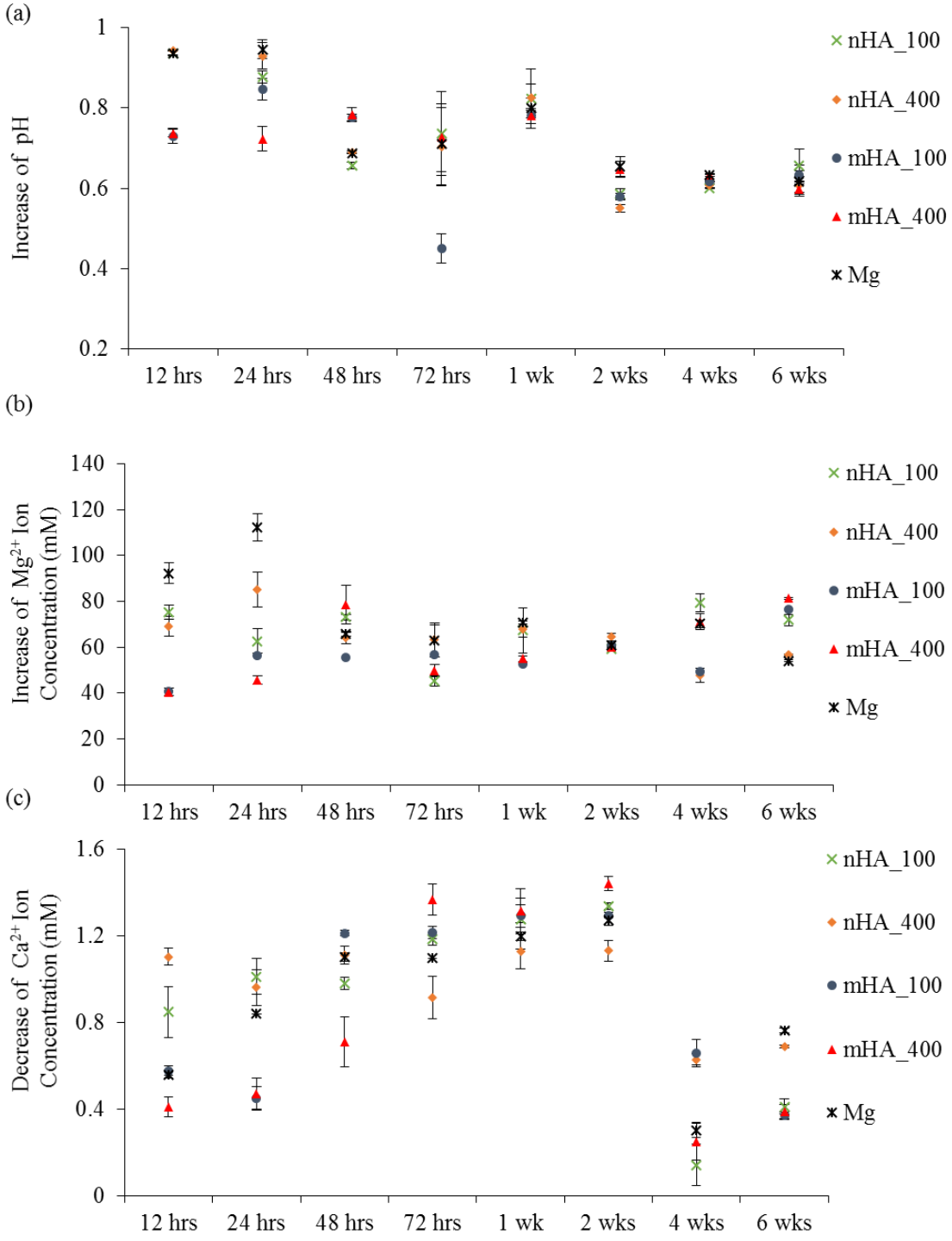

Figure 25 Post-media analysis at different culture time point after immersed nHA_100, nHA_400, mHA_100, mHA_400 and Mg control with a geometry of 7.5 mm × 15 mm in rSBF for 6 weeks. (a) The pH increase of collected rSBF after cultured with each sample at different time point. (b) Mg^{2+} ion concentration increase of collected rSBF after cultured with each sample at different time point. (c) Ca^{2+} ion concentration decrease of collected rSBF after cultured with each sample at different time point. Data are mean ± standard error (N=3).

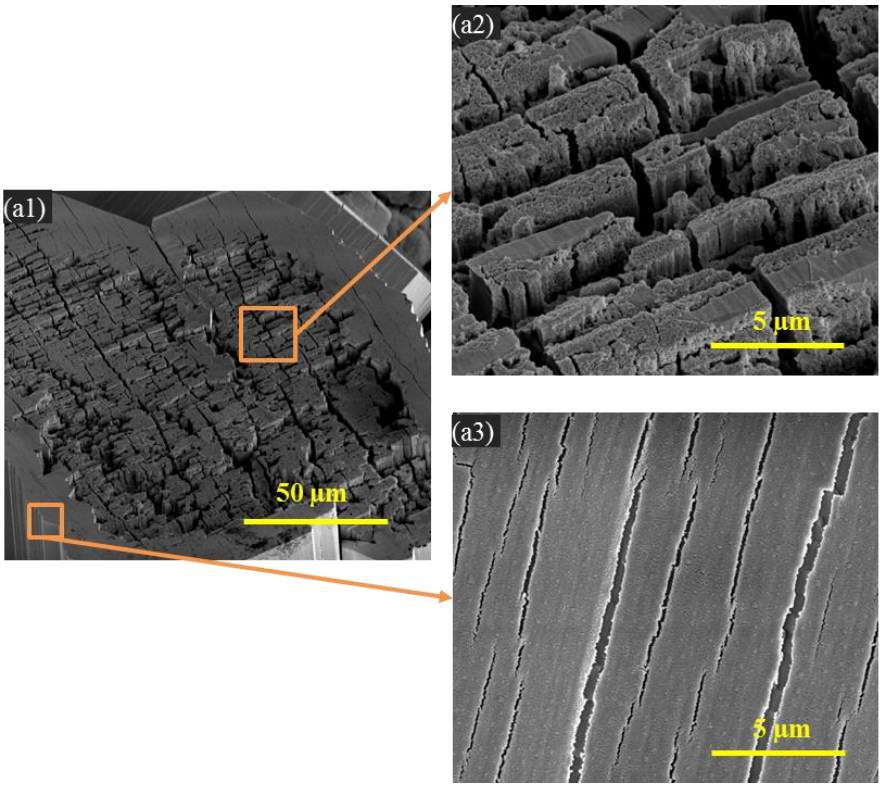

Figure 26 SEM images of the crystals which were found in the degradation layers of Mg after immersed in rSBF for 6 weeks. (a1) Cross region of the crystal. (a2) High magnification SEM image of the cross region of the crystal. (a3) High magnification SEM image of the surface region of the crystal. The original magnifications for (a1) was 1,000x and for (a2), (a3) was 10,000x.

3.3 The Formation of Crystals on the Surface of Mg-based Samples

Crystal degradation products formed on both the Mg disks and Mg rods, where the crystals were large and well-developed on Mg rods. Thusly, further characterizations of the crystal degradation products were performed on Mg rods. The cross section image of the crystal was shown in Figure 26a1. With further high magnification SEM analysis, layers by layers microstructure was found inside the cubic as indicated in Figure 26a2. A single layer was composed of spherical particles which might be the initial nano-size precursors of the crystal. The outside surface of the crystal was flat with few cracks observed, as indicated in Figure 26a3. Similarly, spherical shape feature was observed on

the surface, which were precursors of the crystal. In general, it was suggested that the cubic crystal was formed by aggregation and self-assembling of nano-size precursors.

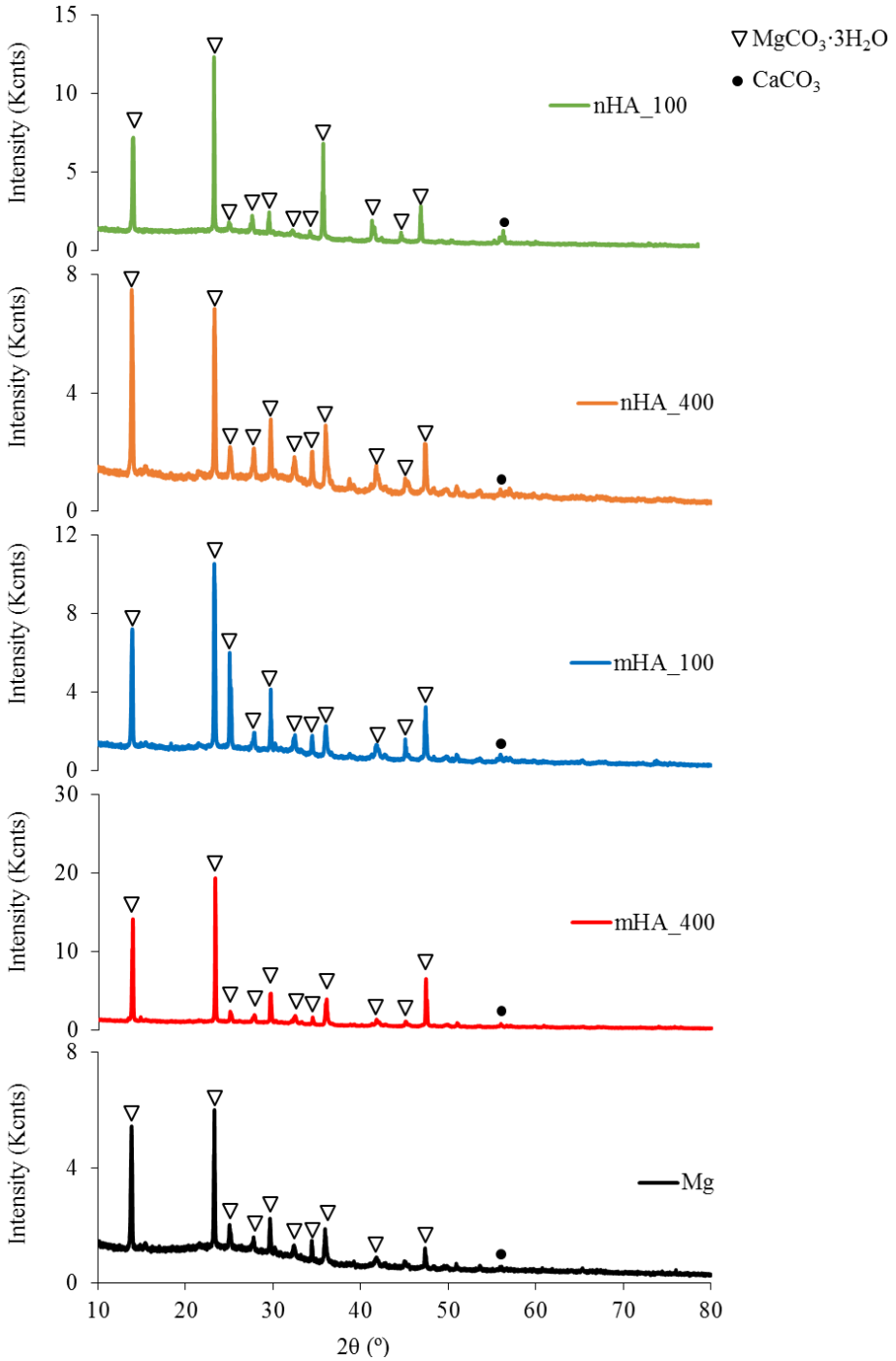

Figure 27 XRD spectra of degradation products on the surface of nHA_100, nHA_400, mHA_100 mHA_100, mHA_400 and Mg after immersed in rSBF for 6 weeks.

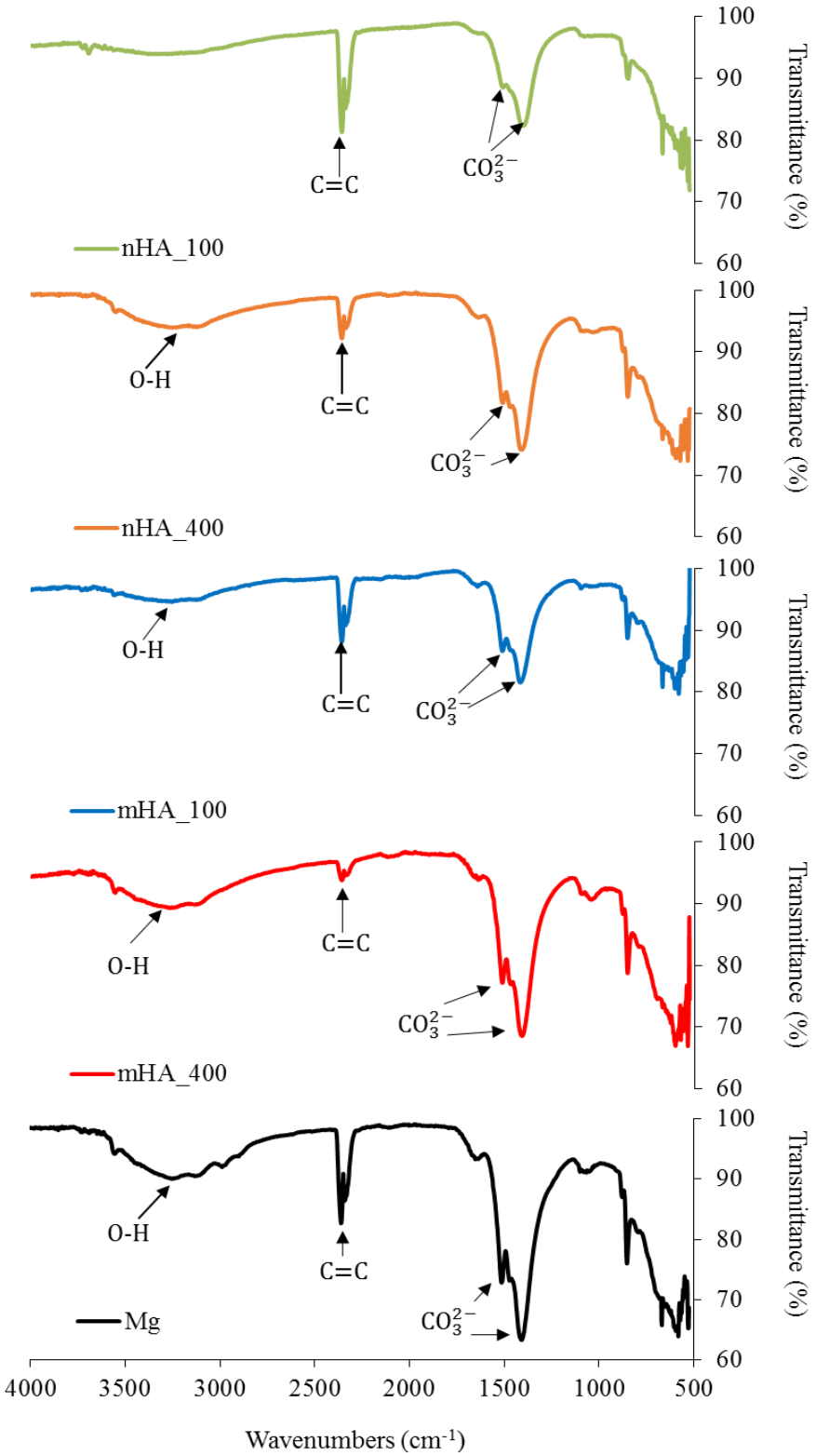

Figure 28 FTIR spectra of degradation products on the surface of nHA_100, nHA_400, mHA_100 mHA_100, mHA_400 and Mg after immersed in rSBF for 6 weeks.

XRD spectra of the samples further confirmed the major peaks matched the reference of $MgCO_3 \cdot 3H_2O$ (Figure 27). Other minor peaks also suggested the presence of $CaCO_3$, which was consistent with previous EDS report. FTIR also confirmed the presence of $MgCO_3 \cdot 3H_2O$ (Figure 28). Specifically, O-H, C=C, and CO_3^{2-} functional groups were identified in the FTIR spectra, which corresponded to the presence of $MgCO_3 \cdot 3H_2O$. All samples showed similar XRD spectra and FTIR spectra after 6 week immersion in rSBF, which suggested a consistent formation of highly crystallized $MgCO_3 \cdot 3H_2O$ phase on all the samples.

3.4 Mechanical Properties of the Mg-based Samples before and after Immersion

Stress and strain curves of Mg rods, i.e., nHA_100, nHA_400, mHA_100, mHA_400 and Mg with a geometry of 7.5 mm × 15 mm, were summarized in Figure 29. Before immersion, Mg-based samples had an ultimate compressive strength around 300 MPa, where the nHA_100 showed the lowest among all (Table 1). After immersion, the ultimate compressive strength of Mg-based samples showed a significant decrease, where Mg control showed the lowest compressive strength among all. The nHA_400 and mHA_400 showed a higher compressive strength compared to other samples, which indicated the coating of 400 series had a better protection of the Mg rods. The maximum load of Mg rods was around 13 kN for all the samples expect nHA_100, which was 11 kN before immersion. A significant decrease was also found for all the Mg-based samples after immersion of 6 weeks. Mg controls had the lowest maximum load of 7 kN, and the nHA_400 and mHA_400 maintained a higher maximum load than all other samples. Young's modulus of the Mg-based samples had a similar result to ultimate stress and

maximum load. Specifically, Mg-based samples showed a significant decrease of Young's modulus, and Mg control had the lowest Young's modulus after 6 weeks immersion.

Table 1: Mechanical properties of nHA_100, nHA_400, mHA_100, mHA_400 and Mg with a geometry of 7.5 mm × 15 mm. (a) Mechanical properties of all Mg-based samples before immersion. (b) Mechanical properties of all Mg-based samples after immersed in rSBF for 6 weeks.

(a)	Ultimate compressive strength (MPa)	Maximum load (N)	Compressive modulus (GPa)
nHA_100	260	11,501	9.03
nHA_400	311	13,724	9.5
mHA_100	305	13,473	9.1
mHA_400	290	12,793	11.2
Mg	300	12,647	9.8

(b)	Ultimate compressive strength (MPa)	Maximum load (N)	Young's modulus (GPa)
nHA_100	215	9,522	5.1
nHA_400	262	11,585	6.4
mHA_100	244	10,797	6.4
mHA_400	276	12,203	6.7
Mg	169	7,032	4.3

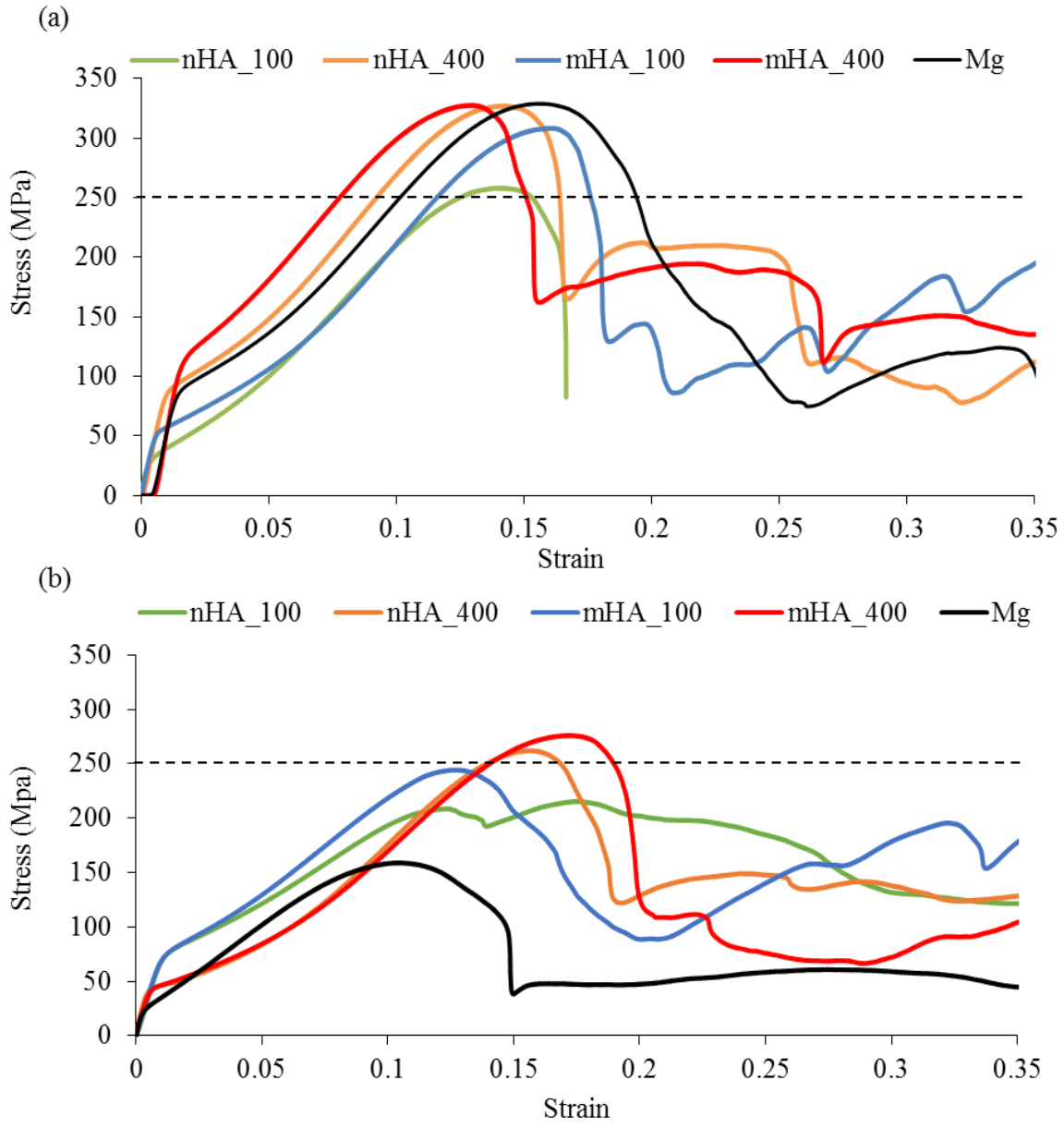

Figure 29 Stress and strain curves of nHA_100, nHA_400, mHA_100, mHA_400 and Mg with a geometry of 7.5 mm × 15 mm. (a) Stress and strain curves of all Mg-based samples before immersion. (b) Stress and strain curves of all Mg-based samples after immersed in rSBF for 6 weeks.

Chapter 7 Nanocomposite Coated Magnesium-Based Implant for Musculoskeletal Applications

1. Introduction

Developing nHA-based composite coating on Mg is also proposed to improve the coating adhesion and bioactivity[79-81]. Biodegradable polymer, such as poly(lactic-co-glycolic acid) (PLGA), could improve the nHA coating adhesion on Mg-based substrates[1], when used in conjunction with nHA. The main degradation products of PLGA are lactic acid and glycolic acid, which can be naturally metabolized in the human body[82]. Moreover, the acidic degradation products of PLGA may be able to neutralize the OH^- ions released during Mg degradation, thus mediating local pH[83]. Poly(lactic-co-glycolic acid) (PLGA) has been approved by the U.S. food and drug administration (FDA) for certain human clinical applications. PLGA spheres have been well studied for drug delivery applications[67, 84]. PLGA degrades in human body by hydrolysis to provide controllable release of drugs during degradation. The two degradation products of PLGA, lactic acid and glycolic acid, are by-products of various metabolic pathways in the body[85]. As a synthetic copolymer, PLGA showed great biocompatibility and biodegradability. However, PLGA has low mechanical strength when used alone.

Collectively, the nHA and PLGA composite coating on Mg substrates provide a promising solution to address the problems associated with each single-phase material and achieve synergistic properties for biodegradable implants. Specifically, Mg substrates provide essential mechanical strength for load bearing, while nHA particles improve bioactivity and osteoconductivity at the implant-tissue interface. The PLGA polymer phase promotes interfacial adhesion between the nHA and Mg, while the nHA phase improves

mechanical strength of PLGA[86]. Additionally, the acidic degradation products of PLGA neutralize the basic degradation products of Mg. The nanostructured coatings on Mg substrates serve dual purposes simultaneously. One is to serve as a barrier to regulate the degradation rate of Mg and another is to improve bone regeneration. Therefore, the triphasic material design, i.e., Mg as the metallic substrate, nHA as the ceramic phase of coating, and PLGA as the polymer phase of coating, provides complementary properties for musculoskeletal implant and device applications[85, 87-88]. The objective of this study is to deposit nanocomposites and nanoparticles onto magnesium (Mg) substrates and characterize them for potential biomedical applications. The components involved, that is, nano-sized hydroxyapatite particles (nHA), poly (lactic-co-glycolic acid) (PLGA), and Mg substrates are all biodegradable in the human body, thus promising for biodegradable medical implant and device applications.

Electrophoretic deposition (EPD) is a promising process for creating nanostructured coatings on Mg substrates. EPD process allows deposition of charged particles onto substrates with complex three dimensional (3D) geometries under an applied electric field at room temperature; and the resulted coatings have controllable thickness and homogeneous morphology[89-91]. Because of these merits, EPD process has been widely used to deposit ceramic materials onto metallic substrates (e.g. titanium). HA coating deposited onto titanium substrates through EPD maintained its tensile bonding strength at 50 to 60 MPa after immersed in simulated body fluid for 8 weeks, which meets the FDA requirement, as compared with other coating methods[92-93]. For example, plasma spray coated or electrochemically deposited HA on titanium showed a respective bonding

strength of 30 MPa and 14 MPa after immersed in distilled water for 4 weeks[92-93]. In addition to improved bonding strength of the coating, the relatively low cost of EPD process compared with plasma spray makes it an attractive option. Most importantly, for deposition of nanoparticles or nanocomposite spheres onto Mg substrates, EPD process can be performed in organic electrolytes (e.g. ethanol or acetone) instead of water to prevent Mg substrates from aggressive degradation during the deposition. Electrophoretic deposition (EPD) is compatible with complex 3-D geometry of implants and is scalable for manufacturing of implants in industry[91].

2. Materials and Methods

2.1 Preparation of nanoparticles and nanocomposite spheres

2.1.1 Synthesis of hydroxyapatite nanoparticles (nHA)

Hydroxyapatite nanoparticles (nHA) were synthesized using a wet chemistry precipitation method followed by hydrothermal treatment. Briefly, 1 M calcium nitrate powder (Sigma-Aldrich) was dissolved in 40 ml deionized (DI) water and ammonium hydroxide (Sigma-Aldrich) was added to adjust to pH 10 or above and produce a final volume of 100 ml. The 0.6 M diammonium hydrogen phosphate (Sigma-Aldrich) solution was prepared similarly with pH adjusted to 10 or above. The calcium nitrate solution was then added into the solution of diammonium hydrogen phosphate using a burette controlled at a 3.6 ml/min flow rate while stirring at 40 °C.

The chemical reaction for synthesizing the nHA [$Ca_{10}(PO_4)_6(OH)_2$] is as follows:

$$10Ca(NO_3)_2 + 6(NH_4)_2HPO_4 + 8NH_4OH \rightarrow Ca_{10}(PO_4)_6(OH)_2 + 6H_2O + 20NH_4NO_3$$

After 20 hours of continuous stirring at 40 °C, the mixture was centrifuged at a spinning speed of 3,000 RPM (Model J-E, Beckman Coulter Inc.) to collect the nHA pellet and remove the supernatant. The nHA particles were washed 3 to 4 times by centrifuge in DI water to remove residual reactants, resuspended in 100 ml DI water, placed in an acid digestion vessel (Model 4748, Parr Instrument Company), and then heated to 200 °C for 20 hours in an oven (Heratherm OGS60, Thermo Scientific). After the hydrothermal treatment, the solution was centrifuged to collect the nHA pellet, and the nHA pellet was subsequently dried in a vacuum oven (Model 414004/57A, VWR) at 80 °C. The dried nHA powder was ground using a mortar with a pestle for about 20 minutes or until satisfactory by visual inspection.

2.1.2. Preparation of nanocomposite spheres and PLGA spheres

Emulsion evaporation method was used to prepare nHA_PLGA composite spheres and PLGA spheres. Specifically, 45 mg PLGA (Sigma-Aldrich, 50/50 lactide/glycolide) with an average molecular weight of 45,000 to 75,000 Da, was dissolved in 3 ml chloroform and sonicated in an ultrasonic bath (Model 97043-936, VWR) at 40 °C. After PLGA was completely dissolved, 5 mg nHA powder was added into PLGA solution and dispersed using a high-power probe sonicator (Model S-4000, Misonix) at 18 watts power for 5 min to reduce the agglomeration of nHA particles in PLGA. After that, 15 ml polyvinyl alcohol (PVA) solution was added to the top of the dispersed nHA_PLGA composite suspension. The PVA solution was prepared by dissolving 1 weight (wt.) % PVA in 1 ml DI water at 70 °C. The mixture was then emulsified using the high-power probe sonicator at a power of 18 watts for 1 min to generate the composite spheres. The

chloroform was evaporated by stirring the suspension overnight. The remaining suspension was centrifuged at 4000 rpm to collect the composite spheres and remove the DI water. This step was repeated for 3 to 4 times to wash away residual reagents. The washed spheres were either suspended in 1 ml DI water and lyophilized (12 L Console freeze dryer, Labconco) for 36 hours before characterization, or suspended in 10 ml ethanol for EPD process. PLGA spheres were prepared as a control using the similar process except that nHA particles were not added.

2.2 Electrophoretic deposition of nanocomposite spheres or nanoparticles onto Mg

The nHA_PLGA composite spheres of 50 mg suspended in 10 ml ethanol served as the electrolyte for depositing nHA_PLGA composite onto Mg substrates. The nHA particles dispersed in ethanol served as the electrolyte for depositing nHA particles onto Mg substrates. To break the nHA agglomerates and obtain a stable colloidal suspension, 50 mg nHA particles were sonicated in 10 ml of ethanol for 5 min using the high-power probe sonicator.

Mg sheets (MiniScience) with a thickness of 1 mm were cut into 10x5 mm rectangle discs using a Notcher (NO.100, Whitney Metal Tool CO.). The substrates were ground using 600 grits SiC paper. After grinding, the substrates were cleaned in acetone (Sigma-Aldrich) and ethanol (Sigma-Aldrich) for 15 min each using an ultrasonic cleaner (Model 97043-936, VWR). Two 10x5x1 mm Mg substrates were used as an anode and a cathode, respectively. The distance between the two parallel substrates was adjusted to 10 mm, as shown in Figure 30. The bottom half (5×5×1 mm) of the Mg substrate was immersed into

the electrolytes as prepared, while the top half was connected to the clamps that attached to the power supply (No.SC-5M, Variac). In this study, a voltage of 150 V and deposition time ranging from 0.5 to 10 min were used. During the EPD process, the electrolyte was stirred when the deposition time was longer than 1 min. When the deposition time was shorter than or equal to 1 min, the electrolyte was not stirred since the deposition finished before the particles had time to settle down.

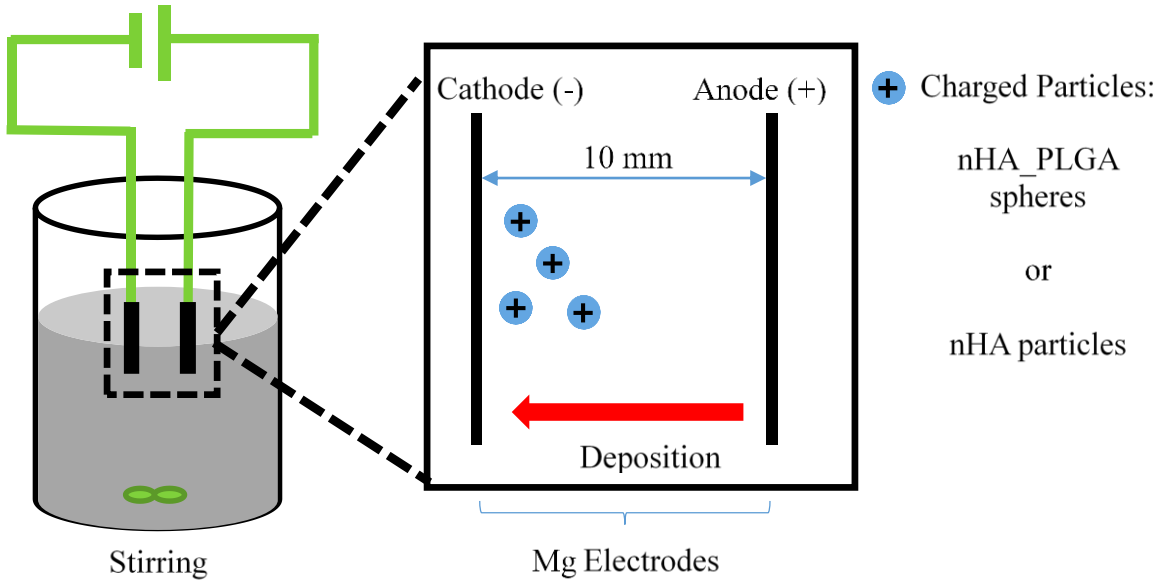

Figure 30 Schematic illustration of electrophoretic deposition of charged particles (either nHA_PLGA composite spheres or nHA particles) onto the Mg substrate.

2.3 Material characterization before and after EPD process

The dried nHA_PLGA composite spheres, nHA particles, and PLGA spheres were mounted on a flat SEM holder (Ted Pella) using double-sided copper tape and sputter coated with platinum/palladium at 20 mA for 60 seconds. The microstructure of nHA_PLGA composite spheres, nHA particles, and PLGA spheres were examined under a scanning electron microscope (SEM; Nova NanoSEM 450, FEI Inc.) using either the Everhart-Thornley detector or the Concentric Backscattered detector at high vacuum mode.

The size distributions of nHA_PLGA composite spheres, nHA particles, and PLGA spheres were determined based on SEM images using the ImageJ analysis tools. Individual sphere or particle was manually outlined using ImageJ to measure the size and distribution. The elemental compositions of the samples were determined using attached energy dispersive x-ray spectroscopy (EDS; Aztec, Oxford instrument) at an acceleration voltage of 10 KV.

The phase and crystal structure of nHA_PLGA composite spheres, nHA particles, and PLGA spheres were examined using X-ray diffraction (XRD; Empyrean, PANalytical) at 45 KV and 40 mA with 2θ angles from 10° to 80º at a step size of 0.02º. The diffraction peaks were identified based on the international center for diffraction data (ICDD) database using HighScore software (PANAlytical). The chemical bonding structures of nHA_PLGA composite spheres, nHA particles, and PLGA spheres were determined using Fourier transform infrared spectroscopy (FTIR, Equinox 55, Bruker) at the transmission mode.

The Zeta potential of nHA_PLGA composite spheres, nHA particles, and PLGA spheres were measured using a Zeta potential & submicron particle size analyzer (Delsa^{TM}Nano C, Beckman Coulter). The flow cell of the analyzer was washed with ethanol three times initially. The respective electrolyte containing nHA_PLGA composite spheres, nHA particles, or PLGA spheres was diluted with ethanol by a factor of 5, and injected into the flow cell with a syringe. The test was carried out at room temperature with an applied potential of 5 V/cm and each sample was tested for three times. The respective electrical mobility of nHA composite spheres, nHA particles and PLGA spheres was measured based on the frequency shift of the scattered light using laser doppler method.

Zeta potential was calculated based on the electrical mobility of the particles, the average velocity of electro-osmotic flow, relative dielectric constant of the solution, solution viscosity, and applied electric field strength according to Smoluchowski equation.

After EPD process, the nHA_PLGA and nHA coatings on Mg substrates were characterized using SEM and EDS analyses. The macroscopic images of the EPD coatings produced at 0.5 – 10 min deposition time were taken with a black background using a camera (Model SX500 IS, Cannon) after the coatings were completely dried in air. Cross-sections of the coatings on Mg substrates were prepared for SEM by polishing the edge of the sample and then mounted vertically onto a 90º SEM holder using double-sided copper tape. The thickness of the coatings was determined based on the SEM images of cross-sections using ImageJ analysis tools. The size and distribution of nHA_PLGA spheres and nHA particles on Mg substrates after EPD process were determined using ImageJ analysis tools, similar to the method mentioned previously.

Table 2: Experimental parameters used for the hardness test.

Indenter Radius (µm)	**5**	**20**
Maximum Force (mN)	0.5	5
Loading Rate (mN/min)	1	10
Unloading Rate (mN/min)	1	10
Creep Time (s)	15	15

2.4 Mechanical testing of nanocomposite and nanoparticle coatings on Mg substrates

The surface indentation hardness of the nHA_PLGA coated Mg and nHA coated Mg was examined using the micro hardness testing module of a mechanical tester (Nanovea, Irvine, CA) according to the ASTM standard E2546 (Standard Practice for

Instrumented Indentation Testing). The spherical indenters with a radius of either 5 µm or 20 µm were used to perform the micro indentation. The specific testing parameters are summarized in the Table 2. The indentation hardness and indentation modulus were calculated for each sample based on the load-displacement curve.

Table 3: Experimental parameters used for the micro-scratch test.

Initial Load (N)	**0.01**
Final Load (N)	3.0
Loading Rate (N/min)	6.0
Scratch Length (mm)	3.0
Scratching Speed (mm/min)	6.0

The adhesion strength of the nHA_PLGA coated Mg and nHA coated Mg was examined using the micro scratch testing module of a mechanical tester (Nanovea). A 120° cone-shaped diamond tip with a radius of 200 µm was used to perform the micro-scratch. The testing parameters are summarized in the Table 3. The initial delamination point was determined based on the optical micrograph of the coating and the friction force curve. The force at which the initial delamination occurred was defined as the critical load (N) for the coating failure.

2.5. Measurement of corrosion properties

The corrosion properties of nHA_PLGA coated Mg, nHA coated Mg, and non-coated Mg were examined according to the ASTM standard G59 (Standard Test Method for Conducting Potentiodynamic Polarization Resistance Measurements) using a Potentiostat (Model 273 A, EG&G Princeton Applied Research). The coated or non-coated Mg substrates were used as the working electrode, platinum was used as the counter electrode, and Ag/AgCl was used as the reference electrode. Only half of the Mg substrates

(5x5mm), i.e., the coated area, were immersed, while the counter and reference electrodes were fully immersed in simulated body fluid (SBF). The potential was set from -3.5 V to 0.5 V with a constant scan rate of 100 mV/s for 40 seconds, and the temperature was set at 37 ºC to represent the body temperature. The corrosion potential, corrosion current density, and corrosion rate (penetration rate) were calculated based on the ASTM standard G102 (Standard Practice for Calculation of Corrosion Rates and Related Information from Electrochemical Measurements).

3. Results and Discussion

3.1. Material characterization before EPD

3.1.1 Morphology, size, and elemental composition of nanocomposite spheres and nanoparticles

The nHA_PLGA composite spheres showed a consistent spherical morphology with a size range of 0.6 µm to 1.5 µm, according to the SEM image (Figure 31a) and quantitative analysis using ImageJ (Figure 31a1). The average size of nHA_PLGA composite spheres was 0.94 ± 0.19 µm and the predominant spheres (30 %) had a size between 0.8 to 0.9 µm (Figure 31a1). The EDS analysis showed the presence of carbon (C), oxygen (O), phosphorus (P), and calcium (Ca) in the composite spheres (Figure 31a2). The peaks of C and O in the EDS spectrum mainly corresponded to the PLGA polymer, while the peaks of O, P and Ca were from the nHA nanoparticles with a Ca/P ratio of 1.65.

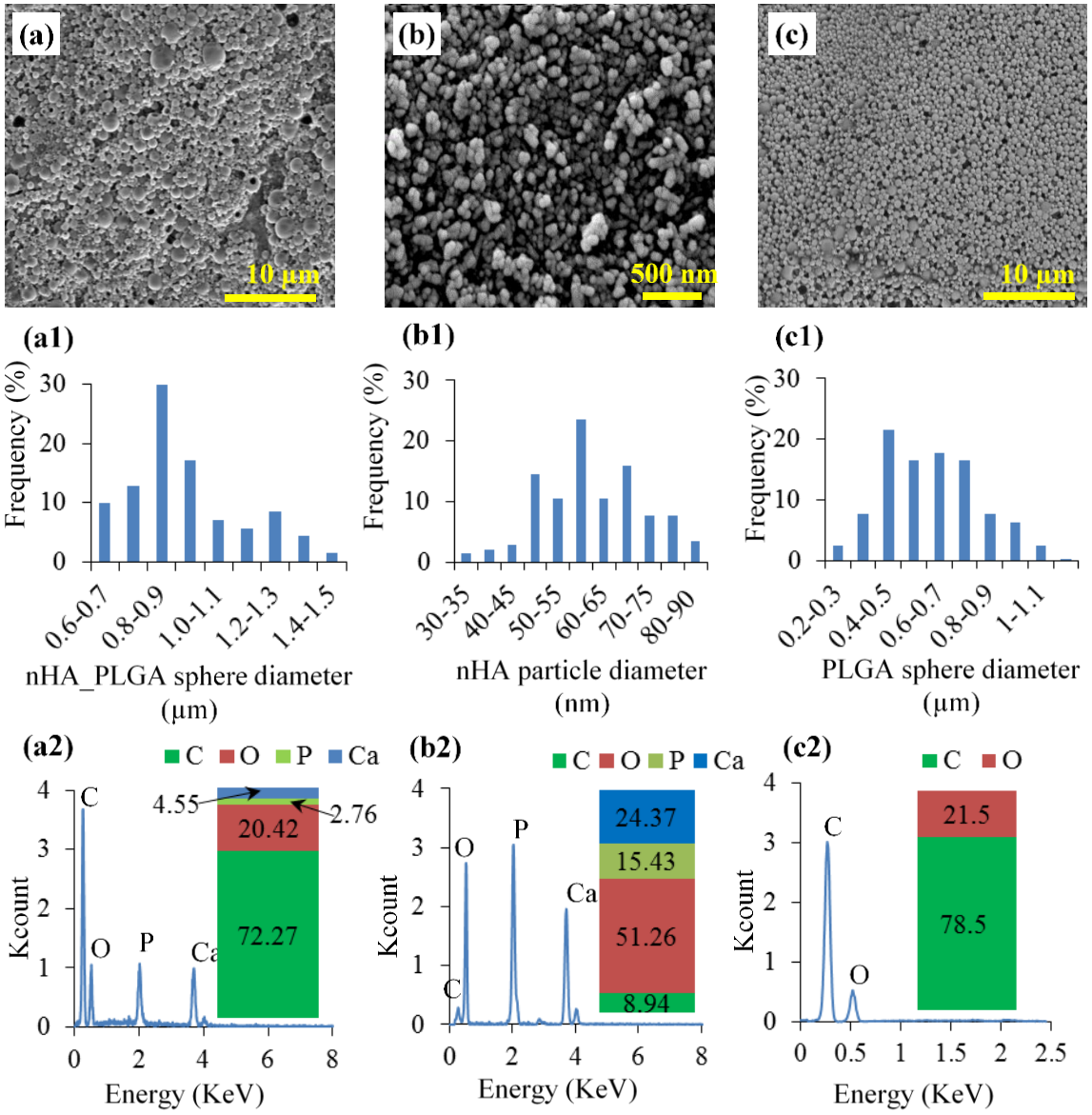

Figure 31 SEM and EDS analyses of (a, a1, a2) nHA_PLGA composite spheres, (b, b1, b2) nHA particles, and (c, c1, c2) PLGA spheres. (a, b, c) SEM of (a) nHA_PLGA composite spheres with a scale bar of 10 µm and an original magnification of 4,000x, (b) nHA particles with a scale bar of 500 nm and an original magnification of 100,000x, and (c) PLGA spheres with a scale bar of 10 µm and an original magnification of 4,000x. (a1, b1, c1) Size distribution of (a1) nHA_PLGA composite spheres with an average size of 0.9 ± 0.19 µm, (b1) nHA particles with an average size of 59 ± 10 nm, and (c1) PLGA spheres with an average size of 0.63 ± 0.19 µm. (a2, b2, c2) EDS spectra and quantified elemental compositions (atomic %) of (a2) nHA_PLGA composite spheres, (b2) nHA particles, and (c2) PLGA spheres. The acceleration voltage was 10 KV for SEM and EDS analyses.

The nHA particles synthesized by wet chemistry showed a near spherical morphology at the nanometer scale (Figure 31b). The average size of nHA particles was

55 ± 11 nm with a size range from 30 to 90 nm, based on quantitative image analysis using ImageJ (Figure 31b1). The majority of nHA particles (25%) had a size between 55 to 60 nm. The EDS analysis detected the presence of C, O, P, and Ca peaks in the nHA particles with a Ca/P atomic ratio of 1.58, close to that of the natural HA in the bone (Figure 31b2). The slight deviation of Ca:P ratio from 1.67 of natural bone might be attributed to the possible presence of other trace phases of calcium phosphates or inherent detection limit of EDS analysis. Further verification using XRD is needed. PLGA spheres had a similar spherical morphology as the composite spheres, but smaller in size at the sub-micron scale, as shown in the SEM image (Figure 31c). The average size of PLGA spheres was 0.63 ± 0.19 μm with a size distribution from 0.2 to 1.2 μm according to the quantitative image analysis (Figure 31c1). The majority of PLGA spheres (25%) had a size between 0.4 to 0.5 μm. The EDS analysis showed only C, O peaks in the PLGA spheres, as expected for the polymer.

The size of spheres or particles is important for the success of EPD process. Generally, smaller particle size is preferred for EPD. Sato et al. reported successful deposition of $YBa_2Cu_3O_{7-\delta}$ particles at the nano scale (60 nm) and submicron scale (3 μm) onto silver plate in an iodine/acetone mixed bath at 10 V and 3 minutes[94]. Moreover, EPD of the nano-sized particles showed less crack formation after sintering 945 ^{o}C for 1 hour[94]. However, there was no clearly defined size limit because EPD process is also dependent on other factors (e.g. zeta potential of particles, stability of colloidal systems, electrolytes, voltage used) as well. The main limitation for depositing large particles is related to their stability under the gravity force since large particles tend to settle down faster according

the Stokes law; EPD may not occur if the particles settle down before being deposited. In a previous study, we reported successful deposition of nHA_PLGA composite microspheres with an average size of 40 µm onto Mg substrates through EPD process[52]. This process was carried out at 100 V with a long duration time of deposition (30 min) and continuous agitation. The SEM images of the coating indicated a morphology change from sphere to oval after the EPD process[52]. This study showed that the submicron scale nHA_PLGA composite spheres with an average size of 0.94 µm and nano-scale nHA particles with an average size of 55 nm was successfully deposited in a much shorter duration (1 min) using EPD process at 150 V, and the particles retained the similar size and morphology after EPD.

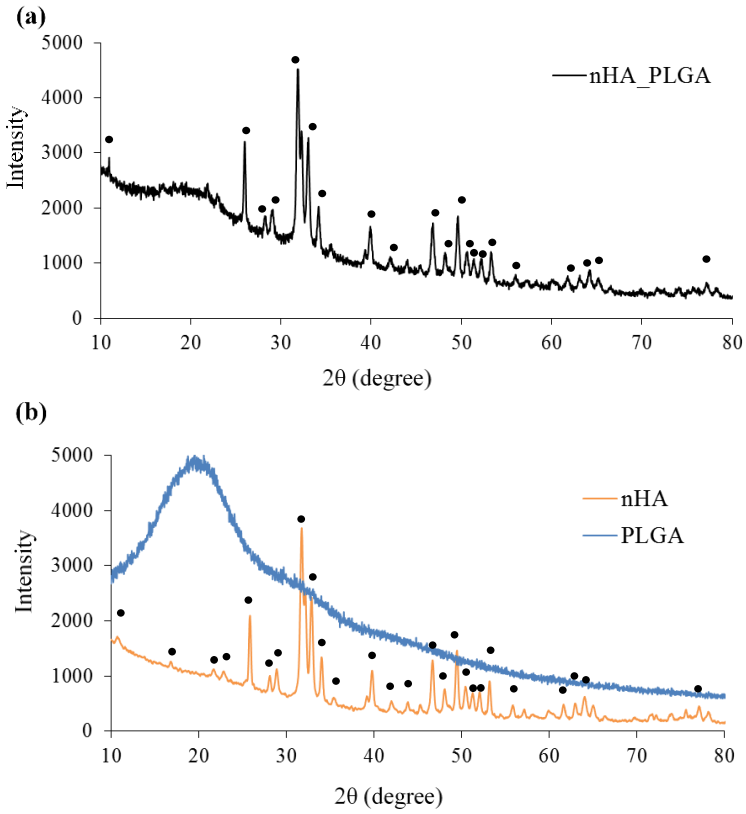

Figure 32 XRD spectra of (a) nHA_PLGA composite spheres (black), and (b) nHA particles (orange) and PLGA spheres (blue). The dots indicate HA phase.

3.1.2 Phase composition and chemical bonding of nanocomposite spheres and nanoparticles

XRD analysis showed the crystal structure and phase composition of the nHA_PLGA composite spheres, nHA particles, and PLGA spheres (Figure 32). The XRD spectrum of nHA_PLGA composite spheres (Figure 32a) confirmed the presence of both nHA and PLGA phases. The nHA phase in the composite spheres is consistent as compared with nHA nanoparticles (Figure 3b, the spectrum in orange color), indicating that the emulsion evaporation process did not cause nHA phase change in the composite spheres. As expected, the major peaks of XRD spectrum of nHA particles matched with the HA reference. Other phase such as tricalcium phosphate was not detected, indicating crystalline HA was the dominant phase. The XRD spectrum of the PLGA polymer (Figure 32b, the spectrum in blue color) showed a broad peak around 20 degree which corresponded with crystalline region of PLGA, and the rest of spectrum indicated the amorphous region of PLGA.

FTIR analysis showed the types of chemical bonding present in the nHA_PLGA composite spheres, nHA particles, and PLGA spheres (Figure 33). In the FTIR spectrum of nHA_PLGA composite spheres (Figure 33a), the major peaks of chemical bonds for both nHA and PLGA were detected. The FTIR spectrum of nHA particles (Figure 33b, the spectrum in orange color) showed chemical bonds of P-O amorphous bending, two P-O crystal bending and P=O stretching at 559.3 cm^{-1} , 528.0 cm^{-1}, and 599.9 cm^{-1}, 1088.5 cm^{-1}, which matched with the HA reference. The C-O, C=O, C-H bonding of PLGA spheres (Figure 33b, the spectrum in blue color) were observed at 1084.9 cm^{-1}, 1747.3 cm^{-1}, 2943.2 cm^{-1} respectively, which matched with the PLGA reference.

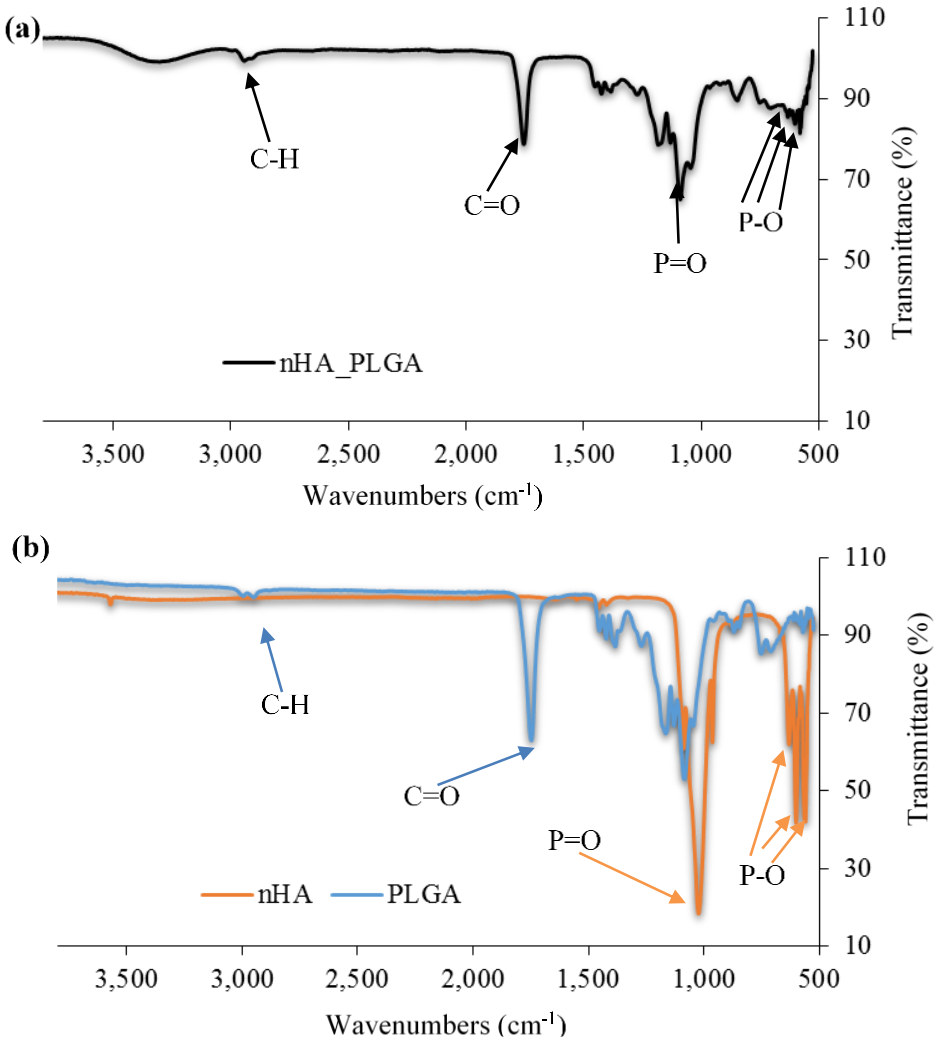

Figure 33 (a) FTIR spectra of nHA_PLGA composite spheres (black), and (b) nHA particles (orange) and PLGA spheres (blue) analyzed in transmission mode.

Collectively, the EDS, XRD and FTIR results confirmed the biphasic nature of the nHA_PLGA composite spheres and the respective composition, phase, and chemical bonding of each phase.

3.1.3 Zeta potential of nanocomposite spheres and nanoparticles

Zeta potential of particles plays an important role in EPD process. The zeta potential and electrical mobility of the respective nHA composite spheres, nHA particles and PLGA spheres in ethanol are summarized in Table 4. Zeta potential is an essential

parameter of charged particles in a colloidal system for EPD process, which represents potential difference between the dispersion medium and the stationary layer of fluid attached to the dispersed particle. Zeta potential indicates the interactions between charged particles and can be related to the stability of the colloidal suspensions. Generally, the colloids with higher zeta potential values (either negative or positive) are more stable than the colloids with lower zeta potential values. Specifically, zeta potential values more than ±60 mV can be considered as excellent stability, from ±30 to ±60 mV can be considered as moderate to good stability, and any values below ±30 mV is considered as low stability.

Table 4: Zeta potential and electrical mobility of nHA_PLGA composite spheres, nHA particles, and PLGA spheres.

Samples	**Zeta Potential (mV)**	**Electrical Mobility (cm^2/Vs)**
nHA_PLGA	33.54±2.74	$4.48\pm0.36\times10^{-5}$
nHA	63.31±4.45	$8.47\pm0.60\times10^{-5}$
PLGA	5.51±5.78	$1.32\pm1.69\times10^{-5}$

Both nHA_PLGA composite spheres and nHA particles showed respective positive charge of 33.54 ± 2.74 mV and 63.31 ± 4.45 mV, indicating relatively good stability in comparison with PLGA spheres (5.51 ± 5.78 mV). The nHA particles had a better stability due to the smaller particle size at the nanometer scale, as compared to the submicron sized nHA_PLGA composite spheres. PLGA spheres showed a low zeta potential of 5.51 ± 5.78 mV in ethanol, and thus were not able to be deposited onto the Mg substrates when the same EPD conditions as that for nHA_PLGA composite spheres and nHA particles were applied.

The mechanism of surface charging for particles in a polar medium (e.g., water) is mainly through adsorption of dissociated ions from the electrolyte solution or ionization of

its own surface groups. In a non-polar medium, such as ethanol, ethanol serves as the proton donor for surface charge. Wang et al. demonstrated that alumina particles in ethanol were charged and stabilized, and concluded that the mechanism of the positive surface charge was through the adsorption of protons onto the alumina surface[95]. Similarly, the nHA phase in nHA_PLGA composite spheres contained hydroxyl groups that tend to attract protons and result in positive charges on the surface.

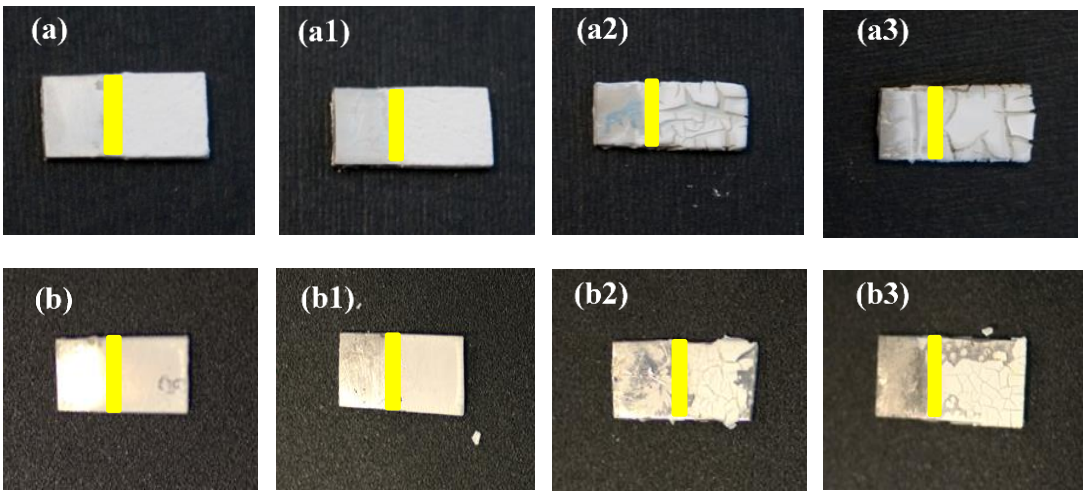

Figure 34 The marcoscopic images of (a-a3) nHA_PLGA composite coatings and (b-b3) nHA coatings on Mg substrates after EPD process at an applied voltage of 150 V and duration of (a, b) 0.5 min, (a1, b1) 1 min, (a2, b2) 5 min, and (a3, b3) 10 min, respectively. The rigt side of the yellow line indiates the EPD coatings deposited on Mg substrates and the left side of the yellow line indicates non-coated area for clamping.

3.2. Material characterization after EPD

The macroscopic images of the Mg substrates with the deposited nHA_PLGA composite spheres and nHA particles showed the effects of deposition time on the coating quality (Figure 34). The thickness of the coating increased as the deposition time increased from 0.5 min to 10 min. When the deposition time was over 1 min, significant cracks started to appear on both the nanocomposite and nHA coatings. A homogenous coating of the nHA_PLGA spheres or nHA particles on Mg substrates was achieved without any visible

cracks at an applied voltage of 150 V for 1 min of deposition time. Therefore, the nHA_PLGA and nHA coatings deposited on Mg substrates at 150 V for 1 min were selected for further material characterization, mechanical testing and corrosion study.

The SEM images of the cross section of the nHA_PLGA coating deposited on Mg substrates at 150 V with a deposition time of 1 min showed a thickness of 110.12 ± 10.45 µm (Figure 35a). The nHA coating deposited on Mg substrates under the same condition showed a coating thickness of 93.02 ± 5.65 µm (Figure 35b). The cracks were observed along the cross section of nHA coated Mg, possibly induced by the air-drying process after EPD, or by the polishing process used for sample preparation before SEM. As compared with the nHA coating, the nHA_PLGA composite coating on the Mg substrate showed a uniform and dense coating without obvious defects.

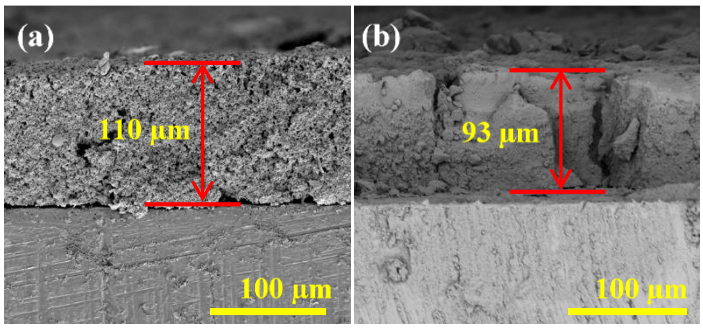

Figure 35 SEM images of cross sections of Mg substrates coated with (a) nHA_PLGA composite spheres, and (b) nHA particles after EPD process at an applied voltage of 150 V and a duration of 1 min. The nHA_PLGA coating had a thickness of 110.12 ± 10.45 µm and nHA coating had a thickness of 93.02 ± 5.65 µm.

The high magnification SEM images of nHA_PLGA or nHA coatings on Mg substrate after EPD showed that the nanocomposite spheres and nanoparticles retained similar morphology (Figure 36) as they were before EPD. The deposited nHA_PLGA composite spheres had a size distribution from 0.6 to 1.6 µm, with 25% composite spheres

had a size range of 0.8 to 0.9 µm (Figure 36a1). The nHA coating after EPD showed a size distribution from 20 to 70 nm with 25 % particle size ranged from 40 to 45 nm (Figure 36b1). The nHA_PLGA composite spheres showed a similar size and distribution while nHA particles showed a slight shift toward smaller particle size when compared with their counterparts before EPD.

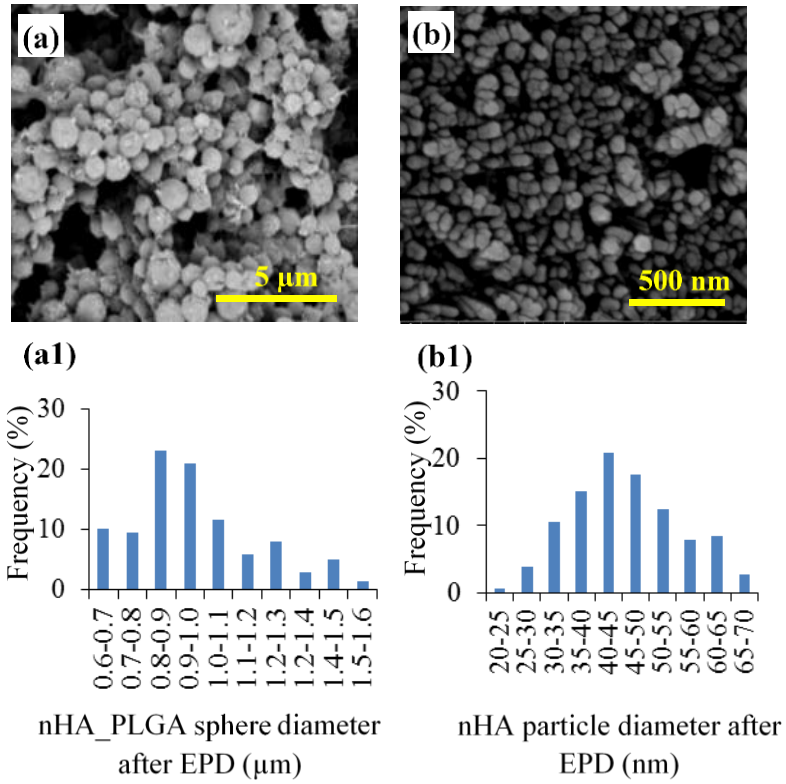

Figure 36 SEM images and size analyses of Mg coated with (a, a1) nHA_PLGA composite spheres, and (b, b1) nHA particles. (a, b) SEM images of (a) nHA_PLGA coated Mg with a scale bar of 5 µm and an original magnification of 10,000x, and (b) nHA coated Mg with a scale bar of 500 nm and an original magnification of 100,000x. (a1, b1) Size distribution of (a1) nHA_PLGA composite spheres and (b1) nHA particles on Mg substrates after EPD.

The SEM images of the nHA_PLGA coatings showed a uniform homogenous coverage without cracks (Figure 37a, a1), while the nHA coatings showed flat surface with some micro cracks at the submicron scale (Figure 37b). The crack-free surface of nHA_PLGA coatings provides better degradation protection for Mg substrates and makes

the degradation more predictable. The SEM images of nHA_PLGA and nHA coatings on Mg substrates at a lower magnification (Figure 37a1, b1) confirmed that both coatings had full coverage on the Mg substrates. The porous microstructures on the surface of nHA_PLGA coatings (Figure 8a) provide desirable anchor sites for cell attachment, thus improving the bioactivity of material. The EDS spectra of nHA_PLGA and nHA coatings showed no Mg peak, which further confirmed a complete coverage of the substrates. (Figure 37a2, b2).

Preventing crack formation on coating during drying or sintering after EPD process is a key challenge. Polymer additives have been incorporated into the electrolyte to increase the adhesion strength of the deposited coatings and reduce cracking. Zhitomirsky et al. added poly (diallyldimethylammonium chloride) into the electrolyte to address the crack formation issue on zirconia coatings when the coating thickness exceeded 0.1 to 0.2 μm. The polymer additive in the electrolyte was adsorbed onto the surface of the zirconia particles, and the highly charged zirconia particles deposited onto the substrates with adsorbed polymer molecules. In this study, PLGA served as a polymer binder; and, therefore, in comparison with nHA coating, the nHA_PLGA composite coating provided better adhesion on Mg substrates without obvious cracks detected under SEM.

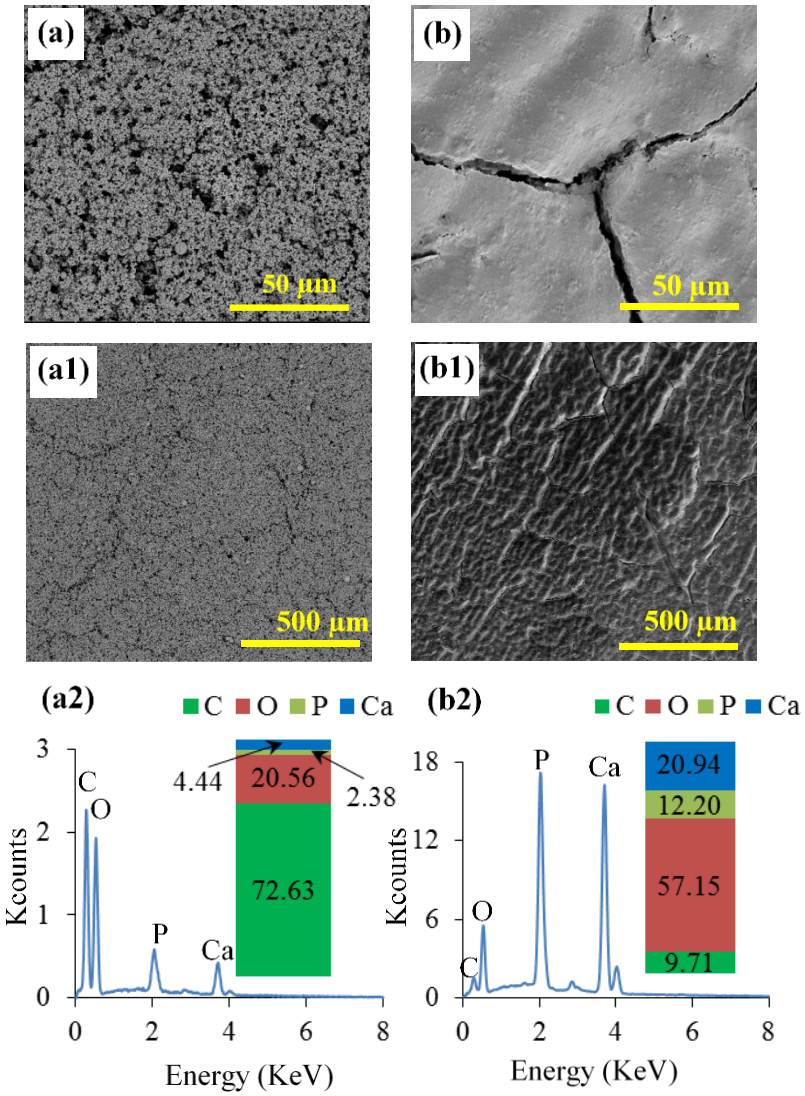

Figure 37 SEM and EDS analyses of Mg coated with (a, a1, a2) nHA_PLGA composite spheres, and (b, b1, b2) nHA particles. (a, b) SEM images of Mg coated with (a) nHA_PLGA composite spheres and (b) nHA particles with a scale bar of 50 µm and an original magnification of 1000x. (a1, b2) SEM images of Mg coated with (a1) nHA_PLGA composite spheres and (b1) nHA particles with a scale bar of 500 µm and an original magnification of 100x. (a2, b2) EDS spectra and elemental compositions (atomic %) of Mg coated with (a2) nHA_PLGA composite spheres and (b2) nHA particles, at an acceleration voltage of 10 KV and an original magnification of 1000x.

EPD process can be carried out in aqueous solutions for most metals. Zhitomirsky et al. suggested that EPD in aqueous suspensions required lower electrical potential, which reduces the cost, but generates hydrogen bubbles due to the electrolysis of water. Uchikoshi et al. compared EPD deposition of alumina and zirconia in aqueous solutions with different

metal substrates as the cathode, including platinum, stainless steel, nickel, and palladium. As compared with other substrates that showed millimeter scale pores, only the palladium substrate showed no pore formation at the micron and millimeter scale mainly due to the absorption of hydrogen by palladium[96]. However, in this study, Mg is an active metal that can react with water as the electrode. When the potential was applied for EPD in aqueous electrolytes, rapid reaction of Mg substrates with water generated hydrogen gas bubbles and heat, which interfered with the particle or sphere deposition onto the substrates. For this reason, ethanol was used as electrolyte instead of water. Although EPD in ethanol required a higher electrical potential than in water, this is necessary to circumvent the rapid chemical reactions of Mg substrates with water.

3.3 Mechanical properties: indentation hardness, modulus, and adhesion strength

The indentation hardness and modulus of the nHA_PLGA coating and nHA coating were calculated based on their respective load-displacement curves, as shown in Figure 38a and 38b. Specifically, the contact depth (h_c) was calculated based on the Equation 1. The h_{max} was the maximum depth, P_{max} was the maximum load, and S was the slope of the unloading curve.

$$h_c = h_{max} - \frac{3P_{max}}{4S} \quad (1)$$

The projected area (A_c) was calculated based on the Equation 2 for spherical indenter. The h_c was the contact depth and R is the radius of the indenter.

$$A_c = \pi(2Rh_c - h_c^2) \quad (2)$$

The indentation hardness of the coating (H) was determined from the maximum load (P_{max}), divided by the projected contact area (A_c), based on Equation 3.

$$H = \frac{P_{max}}{A_c} \quad (3)$$

The indentation modulus (E) was determined from the slope of unloading of the load-displacement curve based on the Equation 4.

$$E = \frac{\sqrt{\pi}}{2}\frac{S}{\sqrt{A_c}} \quad (4)$$

According to the calculation, the nHA_PLGA coated Mg substrates had a hardness of 14.58±3.33 MPa when using the indenter with a radius of 5 μm, as summarized in Table 4. Shirazi et al. reported that the PLGA film prepared by solvent casting method had a hardness of 214 MPa, which was greater than the hardness of the nHA_PLGA coating[97]. The lower hardness of the nHA_PLGA coating was likely because of the porous microstructure of the coating, in contrast to the solid PLGA film produced by solvent casting method[97]. The nHA coated Mg substrates showed a hardness of 96.11±18.61 MPa using the indenter with a radius of 5 μm, as shown in Table 5.

Table 5: Indentation hardness and modulus of nHA_PLGA coated and nHA coated Mg using indenters.

Samples	Indenter Radius (μm)	Hardness (MPa)	Hardness (Vickers)	Modulus (GPa)	Maximum Depth (μm)
nHA_PLGA coated Mg	5	14.58±3.33	1.49± 0.34	0.36 ± 0.05	1.44 ± 0.35
nHA coated Mg		96.11±18.61	9.80 ± 1.90	4.16 ± 0.99	0.20 ± 0.04
nHA_PLGA coated Mg	20	7.42 ± 0.36	0.76 ± 0.04	0.28 ± 0.01	6.77 ± 0.38
nHA coated Mg		10.98 ± 1.99	1.12 ± 0.20	1.38 ± 0.08	4.24 ± 0.80

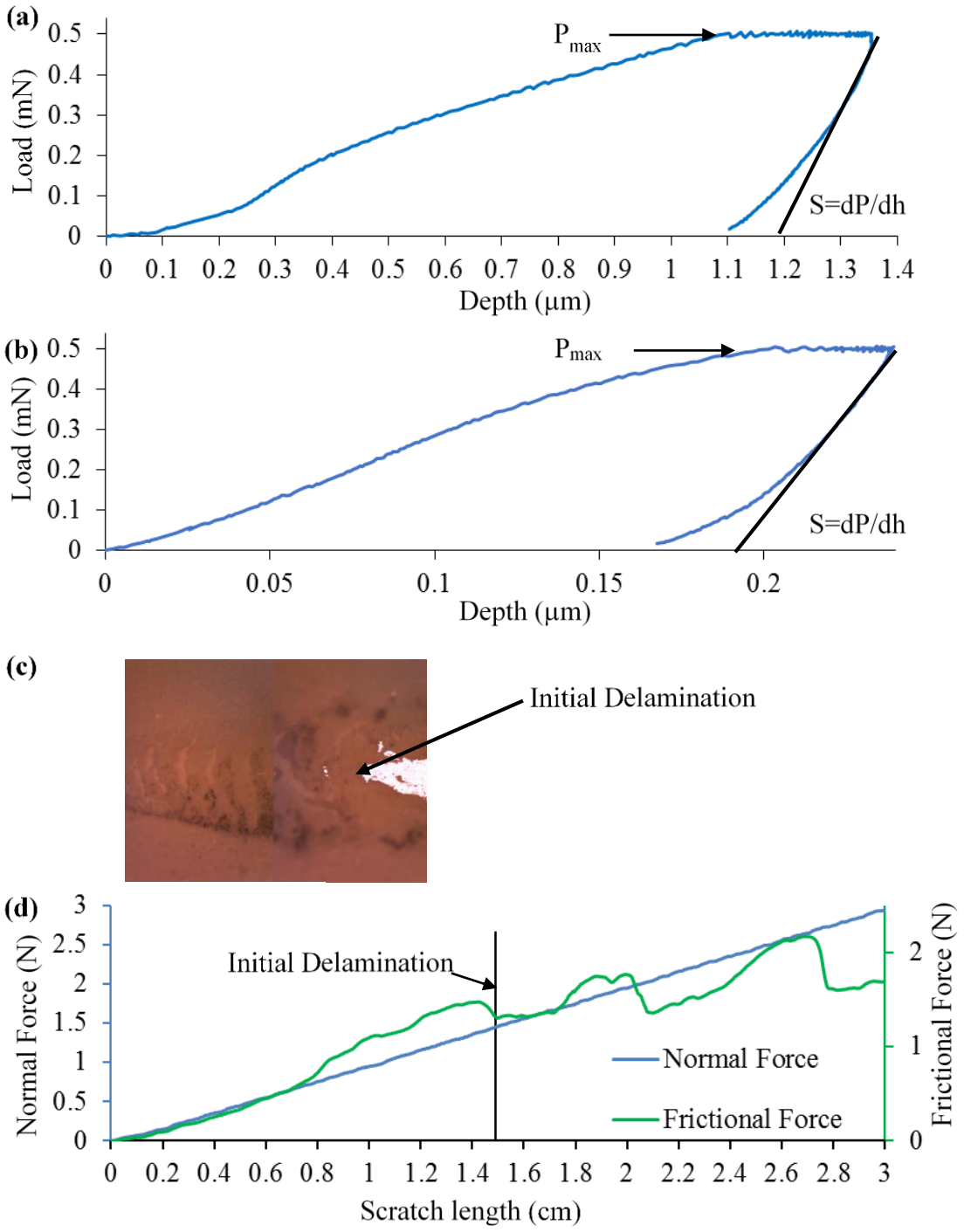

Figure 38 The results of micro-indentation and micro-scratch test. (a,b) The load-displacement curve of (a) nHA_PLGA coating and (b) nHA coating when using the 5 µm indenter. (c) The optical micrograph of the nHA-PLGA coating after the micro-scratch test. (d) The friction force curve during the micro-scratch test for the nHA-PLGA coating.

Kaya et al. reported that electrophoretically deposited 20 nm HA nanoparticles on titanium substrate had a hardness of 4880 MPa after sintering at 600°C[98]. In this study, the hardness of the nHA coated Mg was measured immediately after EPD process without sintering (also called green coating). The porous structure of the green coating might have contributed to the lower hardness measured. We confirmed this hypothesis using an indenter with a radius of 20 μm. The larger indenter had a larger contact area with the samples; that is, the indenter had greater probabilities to be in direct contact with the pores in the coating. Consequently, the measured hardness of the coating decreased to 10.98±1.99MPa when using the larger indenter. A sintering process may improve the nHA coating hardness, which will be investigated in the future.

The indentation modulus of the nHA_PLGA coated Mg was 0.36±0.05 GPa using the 5 μm indenter, and the modulus results reduced to 0.28±0.008 GPa using 20 μm indenter, as shown in Table 5. The modulus of the nHA_PLGA coating had a similar value as compared with a porous PLGA membrane produced by electrospinning[99]. Specifically, Duan et.al reported that the PLGA membrane generated through the electrospinning process had a modulus of 0.41 GPa[99]. In contrast, the indentation modulus of the nHA coated Mg was greater, specifically, 4.16±0.99 GPa when using the 5 μm indenter, as shown in Table 4. When using the 20 μm indenter, the modulus of the nHA coated Mg reduced to 1.38±0.08 GPa, which was likely due to the porous structures of the coating. Kaya et al. reported that electrophoretically depositing HA nanoparticles with a size of 20 nm on titanium had a modulus of 15 GPa after sintering at 600°C[98]. In this study, the modulus of the green coating, i.e. the nHA coating without sintering, was found to have a

lower value than the sintered nHA coating[98]. This suggested that the mechanical properties of the coatings could be improved by sintering in the future studies.

Table 6: Micro-scratch results of nHA_PLGA coated and nHA coated Mg.

Samples	Critical Load (N)
nHA_PLGA coated Mg	1.56± 0.08
nHA coated Mg	1.32±0.02

The critical load of the coatings was defined as the load at the initial delamination, which was determined based on the optical micrograph (Figure 38c) and the friction force curve (Figure 38d). Specifically, the starting point of initial delamination was identified on the optical micrograph where the bright spot appeared. The starting point of initial delamination was confirmed using the friction force curve, as indicated in Figure 38d. The force at the initial delamination was defined as the critical load. The critical load of nHA_PLGA and nHA coated Mg substrates was 1.56±0.08 and 1.32±0.02 N respectively, as listed in Table 6. The nHA_PLGA coating had a higher critical load than the nHA coating, which indicated that the PLGA improved the adhesion strength of the coating. The scratch resistance of the nHA coating on Mg was similar to the ceramic nanoparticles electrophoretically deposited on titanium alloy[100]. Specifically, the HA and TiO_2 nanoparticles with a respective size of 35 and 65 nm were co-deposited onto titanium alloy using EPD, and the critical load of the coating reached 1.52 N before sintering[100].

Table 7: The Tafel test results of nHA_PLGA coated, nHA coated, and non-coated Mg.

Samples	Corrosion Potential (V)	Corrosion Current Density (A/cm^2)	Corrosion Rate (mm/year)
nHA_PLGA coated Mg	-1.310±0.016	$1.20\pm0.32\times10^{-3}$	50±16
nHA coated Mg	-1.528±0.046	$2.35\pm0.54\times10^{-3}$	104±22
Non-coated Mg	-1.555±0.007	$3.04\pm0.13\times10^{-3}$	121±5

3.4. Corrosion properties

The corrosion properties of the coated and non-coated Mg substrates were determined based on the potentiodynamic measurements. The potentiodynamic polarization curves of nHA_PLGA, nHA coated Mg, and non-coated Mg were generated in simulated body fluid (SBF) at the pH of 7.4 and 37ºC, as shown in Figure 39. The corrosion potential for nHA_PLGA coated Mg was -1.310 ± 0.016 V and nHA coated Mg was -1.528 ± 0.046 V, as compared with the corrosion potential for non-coated Mg (-1.555 ± 0.007 V). The corrosion rate (penetration rate) of nHA_PLGA coated Mg was calculated to be 50 ± 16 mm/year and nHA coated Mg was 104 ± 22 mm/year, as compared with non-coated Mg which was 121±5 mm/year, as summarized in Table 7. The results showed that both nHA_PLGA and nHA coatings reduced the corrosion rate of Mg, and the nHA_PLGA composite coatings reduced Mg corrosion rate the most.

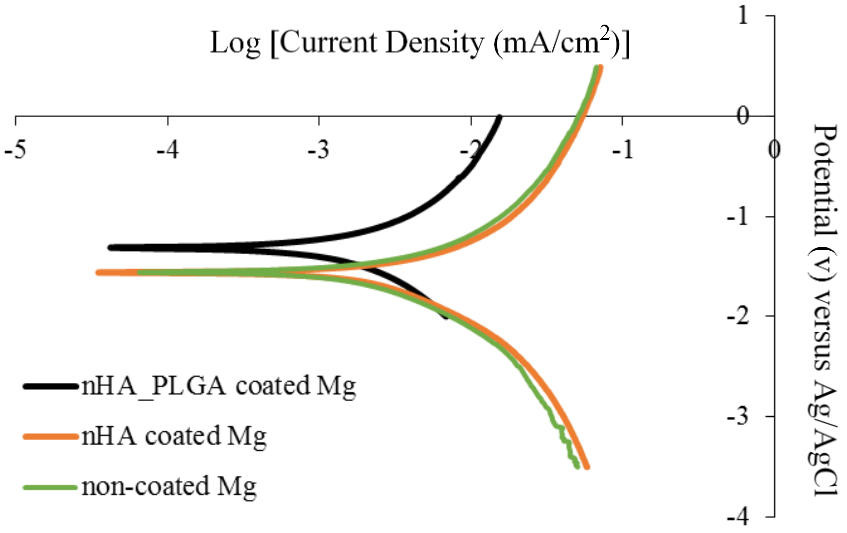

Figure 39: Potentiodynamic polarization curves of Mg coated with nHA_PLGA composite spheres and nHA particles in comparison with non-coated Mg, in a simulated body fluid (SBF) at pH 7.4 and 37ºC.

In a summary, nanophase hydroxyapatite (nHA) and poly (lactic-co-glycolic acid) (PLGA) composite microspheres as well as nHA nanoparticles were successfully deposited on three-dimensional magnesium (Mg) substrates in an ethanol electrolyte using electrophoretic deposition (EPD) and characterized. EPD provides a tunable process to adjust the composition and morphology of the nanostructures on Mg substrates through changing the processing parameters, e.g. characteristics of charged species, electrolyte, applied voltage, and deposition time. Surface characterization of the nHA_PLGA composite microspheres and nHA nanoparticles showed consistent morphology, composition, size, and distribution before and after deposition onto Mg substrates using EPD. Mg substrates coated with nHA_PLGA composite spheres were uniform without cracks. The nHA_PLGA coating showed greater adhesion strength when compared with nHA coating. The nanocomposite coated Mg showed slower corrosion rate than the nHA coated Mg and non-coated Mg, thus promising for use as the next-generation biodegradable implant materials. Further studies of the interfacial properties of the triphasic nHA, PLGA and Mg are still needed for their potential applications in biodegradable implants or devices.

Chapter 8 Proposal of Standard In Vitro Test of Magnesium

1. Introduction

In order to represent the *in vivo* environment around ureteral stents closely, we designed three *in vitro* culture methodologies to study the interactions of HUCs with Mg-based biomaterials in different spatial configurations. Specifically, the three different culture methodologies are (1) direct culture that characterizes the interactions of newly seeded cells with the biomaterials of interest directly at the interface, (2) direct exposure culture that mimics the interactions between the established cells in the body with the biomaterial of interest when they are in direct contact with each other, (3) exposure culture that represents the interactions between the established cells and the biomaterial of interest when they are not in direct contact with each other but in the same environment. Moreover, we previously demonstrated that different surface conditions of Mg alloy samples, such as oxidized versus metallic surfaces, influenced their degradation rates and cytocompatibility[19]. Thus, the effects of sample surface conditions (oxidized versus metallic) on HUCs were also investigated in each culture method in this study. In addition, HUCs were cultured in the media with adjusted initial pH and Mg^{2+} ion concentration to explore the possible effects of soluble degradation products of Mg-based materials on the cells.

The objective of this study was to investigate the cytocompatibility of Mg alloys and their soluble degradation products *in vitro* using the HUC cultures for potential urological device applications, e.g., ureteral stents. The results from this *in vitro* study will also provide valuable information regarding the degradation behavior of magnesium-

yttrium (MgY) and AZ31 alloys in the HUC cultures. The critical pH and Mg^{2+} ion concentration were investigated to determine their effects on HUCs *in vitro* and potentially provide design guidelines for the use of Mg-based materials *in vivo*. Furthermore, the culture methods established in this study offer potential *in vitro* culture models to screen Mg-based biodegradable metals for ureteral stent applications and identify possible adverse effects of Mg-based materials in the early stage.

2. Materials and Methods

2.1 Sample Preparation

Mg-4 wt. % yttrium (MgY) alloy was prepared using a metallurgical processing of melting and casting as previously described[19, 101]. Commercially available Mg-3 wt. % aluminum-1wt. % zinc (AZ31, Alfa Aesar) and pure magnesium (Mg, 98% purity, Miniscience) was included as controls. MgY, AZ31, and Mg substrates were first grinded using 600-grit silicon carbide (SiC) abrasive papers (Ted Pella Inc., Redding, CA, USA) and then autoclaved to oxidize the surfaces using an autoclave (BSL3, R-V industries Inc., PA, USA). The substrates with oxidized surfaces were referred to as MgY_O, AZ31_O and Mg_O, respectively. The substrates that were sequentially polished to expose the metallic surface using the SiC papers of 600, 800, and 1200 grits were referred to as MgY_M, AZ31_M and Mg_M, respectively.

Polyurethane stents (PU; US626, Cook medical, Bloomington, IN, USA) were flattened and used as a reference to represent the current materials used for commercially available ureteral stents. Specifically, PU stents were first cut open and placed between two glass slides for flattening. They were submerged in 100 ºC water for 20 min, cooled in

room temperature for 10 min, re-submerged in 100 ºC water for another 10 min, placed in the refrigerator at 4 ºC for 10 min, and then dried in air at room temperature for at least 12 hours. Premium microscope slides (Fisher Scientific, Hampton, NH, USA) was included as a reference for cell culture experiments.

All substrates were cut into 5×5 mm squares with a thickness of 0.25 mm for MgY and 1 mm for AZ31 and Mg. MgY and PU were cut using scissors, while AZ31 and Mg were cut using a notcher (No.100, Whitney Metal Tool Co.). Glass slides were cut using a glass cutter. After cutting, all substrates were cleaned in acetone (Sigma Aldrich, St Louis, MO, USA) for 60 min and then 200 proof ethanol (Sigma Aldrich, St Louis, MO, USA) for 60 min at room temperature using an ultrasonic bath (Model 97043-936, VWR, Radnor, PA, USA). The initial mass of each sample were weighed before the cell culture using an analytical balance (Ms104S, Mettler Toledo, Columbus, OH, USA), and recorded as the initial mass (M_o). The post-culture samples were weighed after complete dry to determine the final mass (M_f). The mass ratio of substrates was then calculated following M_f/M_o, i.e., the ratio of final mass (M_f) to the initial mass (M_o). All samples were disinfected under ultraviolet (UV) radiation for at least 1 hour on each side. The samples were characterized before exposure to cell culture.

The disinfected samples were all coated with 2 μg/cm^2 of poly-L-lysine (PLL; Sciencell, Carlsbad, CA, USA) to prepare the samples for the HUC culture. For the PLL coating, the substrates were placed in the center of non-treated 12 well culture plates, and 7.6 μl of 1 mg/mL PLL solution was added on top of each substrate followed by 1 mL of distilled water. The plates were then placed into the incubator (MCO-19AIC, SANYON

Eelectric CO. Ltd., JP) with standard cell culture conditions (i.e., a sterile, 5% CO_2/95% air, humidified environment) for at least 2 hours, and then washed twice with deionized (DI) water to remove the non-bound PLL on the substrates.

2.2 Human Urothelial Cell Culture

2.2.1 Preparation of Human Urothelial Cell Culture

Human urothelial cells (HUCs; Sciencell, Carlsbad, CA, USA) isolated from the human bladder were thawed and cultured in the HUC growth media. HUC growth media were prepared by adding 1% urothelial cell growth supplement (UCGS; Sciencell, Carlsbad, CA, USA) and 1% penicillin/streptomycin (P/S; Sciencell, Carlsbad, CA, USA) into basal urothelial cell media (UCM; Sciencell, Carlsbad, CA, USA). Non-treated T-75 flasks coated with 2 μg/cm^2 of PLL were used for HUC culture as described above. HUCs were cultured in the prepared flasks with 25 ml of media under standard cell culture conditions. The culture media was changed every other day until the cells reached 90 to 100 % confluence. The cells were then detached using trypsin (Life Technologies, Carlsbad, CA, USA), seeded and cultured with the samples of interest as described above.

2.2.2 Culture of HUCs with the Samples

Three different methodologies were used to culture HUCs with the samples, as shown in Figure 40. Figure 40a1-a3 illustrate the Direct Culture (D), Figure 40b1-b3 illustrate the Direct Exposure Culture (DE), and Figure 40c1-c4 illustrate the Exposure Culture (E).

Direct Culture (Figure 40a1-a3): Non-tissue culture treated 12-well plates (BD Falcon™, Franklin Lakes, NJ, USA) were coated with 2 μg/cm^2 of PLL using the same

procedure as described above. The PLL-coated substrates as described above were then placed into the center of the PLL coated well plates, as shown in Figure 40a1. The HUCs were seeded directly onto the prepared substrates in each well at a seeding density of 10,000 cells/cm^2, i.e. the initial cell density, C_o, and cultured for 24 hours under standard cell culture conditions, that is, a sterile, 5% CO_2/95% air, humidified environment, as shown in Figure 40a2-a3.

Direct Exposure Culture (Figure 40b1-b3): HUCs were first seeded into each well of the PLL-coated 12-well plates and cultured for one day, as shown in Figure 1b1. Phase contrast images were taken to determine initial cell density (C_o). Specifically, 5 random images of each well were collected using an inverted optical microscope (Eclipse Ti and NIS software, Nikon, Melville, NY, USA). The total cell numbers in each image were counted using ImageJ and the cell density in each well was calculated as C_o (cells/cm^2). The prepared substrates were then placed directly on top of the cell layer and cultured for 24 hours, as shown in Figure 1b2-b3.

Exposure Culture (Figure 40c1-c4): HUCs were first seeded into each well of the PLL-coated 12-well plates and cultured for one day, as shown in Figure 40c1. Phase contrast images were used to calculate the initial cell density (C_o) in each well prior to sample introduction, using the same method as described in direct exposure culture. The PLL-coated substrates were placed in a Transwell® insert that had a membrane pore size of 0.4 μm diameter (BD Falcon™, Franklin Lakes, NJ, USA). The Transwell® inserts with the samples were introduced into each well, and the distance between the Transwell® insert and the cell layer was 0.9 mm, as shown in Figure 40c2. The samples were cultured with

HUCs for 24 hours and 48 hours, as shown in Figure 40c3-c4. During the 48 hours of exposure culture, the media for each well were removed and replaced with fresh media at the first 24 hours.

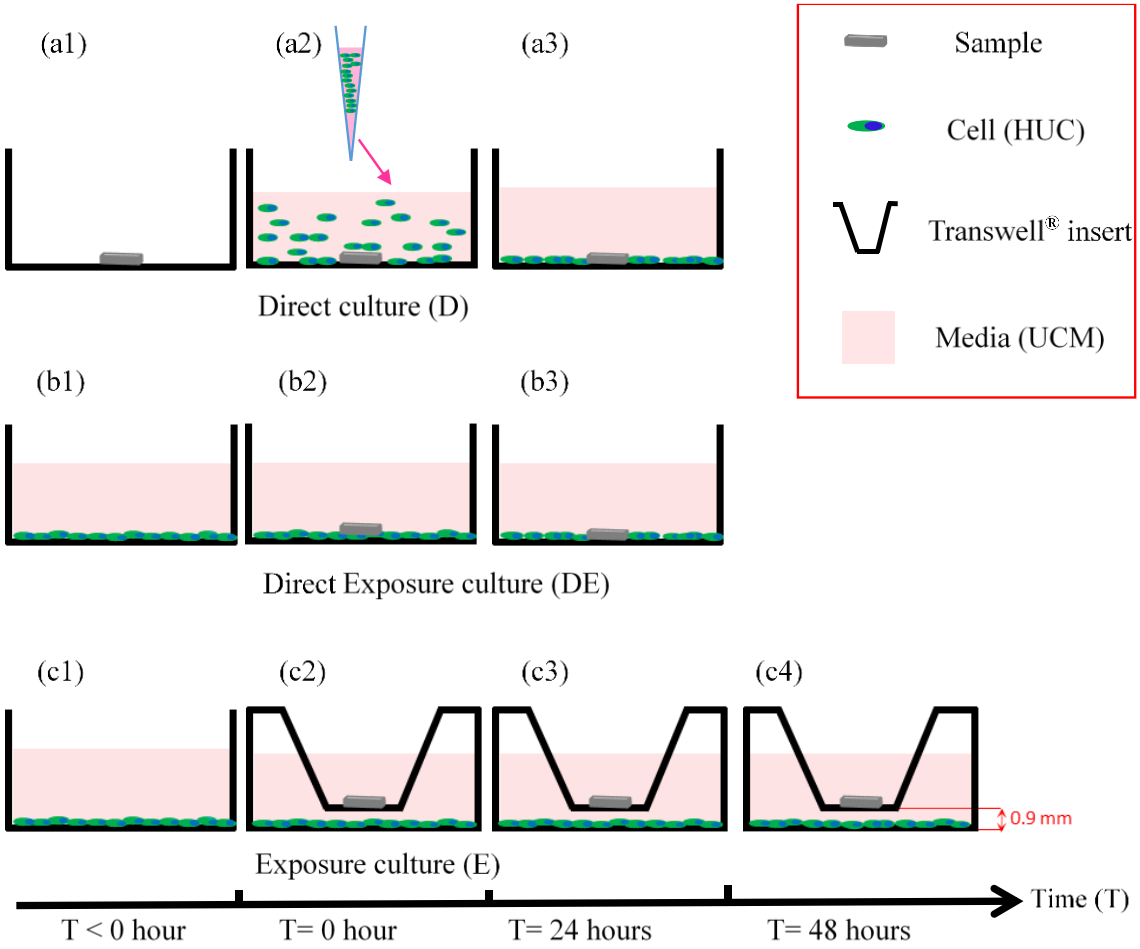

Figure 40 The illustrations of different culture methodologies in a well of a 12 well tissue culture plate, (a) direct culture (D); (b) direct exposure culture (DE); and (c) exposure culture (E). The first column (a1-c1) represents the time before the samples were exposed to the cell culture (T < 0 hour); the second column (a2-c2) represents the starting point when the samples were in the culture (T = 0 hour); the third column (a3-c3) represents the time point when the samples were cultured with the cells for 24 hours (T = 24 hours). (c4) The culture was extended for additional 24 hours (T = 48 hours). The volume of the media in each well was 4 ml.

The substrates with HUCs were all cultured in 4 mL media. HUCs cultured in the wells without any substrates were used as reference; this group was termed as “Cells” in the results. Blank media (4 mL) without cells and substrates was termed as “Media” and

used as a blank reference. The cell culture experiments were all conducted in triplicate. All well plates were incubated under the same standard culture condition for the prescribed period.

2.3 Fluorescence Imaging for Cell Density and Morphology

After the prescribed culture period, the cells attached on or around each sample in each well were fixed and stained for fluorescence imaging to visualize cell morphology and to calculate cell adhesion density. In direct culture or direct exposure culture, the cells attached directly on the sample surface were considered as direct contact, while the cells attached on the tissue culture plate around the sample were considered as indirect contact. In exposure culture, the cells attached onto the tissue culture plate were considered as indirect contact.

After the prescribed culture period, non-adherent cells were washed away using 1 mL phosphate buffered saline (PBS), and the adherent cells were fixed with 4% paraformaldehyde (VWR, Radnor, PA, USA) for 20 min and washed with PBS for 3 times. The fixed cells were then stained with Alexa Fluor® 488-phalloidin (Invitrogen) for 20 min and 4', 6-diamidino-2-phenylindole (DAPI; Invitrogen) for 5 min. After each staining, the cells were washed twice with 1 mL PBS. The well plates were placed on a fluorescence microscope (Eclipse Ti with NIS software, Nikon, Melville, NY, USA) for imaging. The final cell density (C_f) after each prescribed culture was quantified based on at least fifteen fluorescence images per well. Specifically, the cell number per well was quantified by counting the DAPI-stained nuclei in each image and then the final cell density was calculated as the number of adherent cells per unit area. The cell density ratio was

calculated as C_f/C_o, i.e., the ratio of final cell density (C_f) to the initial cell density (C_o). Cell morphology was quantified by manually outlining 10 cells per image in ImageJ to obtain the values for average spreading area per adherent HUC, maximum diameter (D_{max}), and minimum diameter (D_{min}) of each cell. The aspect ratio of cells was calculated as D_{max}/D_{min}. Average spreading area of adhered HUCs in the cultures with the substrates of interest was normalized by the cells only control group of each culture. Average aspect ratio of adhered HUCs in the cultures with the substrates of interest was normalized by the cells only control group of each culture.

2.4 Sample Characterization before and after Cell Culture

To verify the presence of PLL on the surface of Mg-based substrates, Mg substrates that were polished to 1200 grits were cut into the size of 15×10×1mm, and coated with PLL as described above. The glass substrates were cut into the same size and coated with PLL for comparison. PLL-coated Mg (Mg_PLL), PLL-coated glass (Glass_PLL), non-coated Mg and non-coated glass controls were characterized using X-ray photoelectron spectroscopy (XPS). A Kratos AXIS ULTRA^{DLD} XPS system equipped with an Al Kα monochromatic X-ray source and a 165-mm mean radius electron energy hemispherical analyzer was used. The spectra were acquired at a vacuum pressure below 3×10^{-9} torr. Pass energies used for survey scans started from 1400 eV and ended at -5 eV with a step size of 1 eV and 1 sweep. The detailed scans of N 1s started from 410 eV and ended at 390 eV with a step size of 0.1 eV and 20 sweeps.

The Mg-based substrates (MgY, AZ31, and Mg with either oxidized or metallic surfaces), PU control, and glass reference were characterized before and after cell culture

using a scanning electron microscope (SEM; Nova NanoSEM 450, FEI Inc. Hillsboro, OR, USA) with the concentric backscattered detector at the high vacuum mode under an acceleration voltage of 10 kV and a spot size of 4.5. The surface elemental compositions of the substrates before and after the cell culture were determined using energy dispersive x-ray spectroscopy (EDS; Aztec, Oxford instruments, Abingdon, UK). After the prescribed HUC culture, all substrates were collected from the well plate, and dried in air at room temperature for at least 12 hours. The pre-culture and post-culture samples were mounted onto a flat SEM holder (Ted Pella Inc., Redding, CA, USA) using double-sided copper tape. For the pre-culture samples, all substrates except MgY_M, AZ31_M and Mg_M were sputter coated with platinum/palladium at 20 mA for 60 seconds using a sputter coater (Model 108, Cressington Scientific Instruments Ltd., Watford, UK). For the post-culture samples, all substrates were sputter coated with platinum/palladium.

2.5 Post-culture Media Analysis

The post-culture media were collected from each well for measuring pH and Mg^{2+} ion concentrations. The pH of the media was measured immediately after collection using a pre-calibrated pH meter (SB70Pm, SympHony, VWR). The Mg^{2+} ion concentrations were quantified using inductive coupled plasma - optical emission spectrometry (ICP-OES; Optima 8000, Perkin Elmer, Waltham, MA, USA). Briefly, the collected media from each well were diluted with DI water by a factor of 1:100 into a total volume of 10 ml. Mg^{2+} ion concentrations were then obtained from calibration curves generated using Mg^{2+} standards (Perkin Elmer) serially diluted to a concentration of 0.5, 1, 2, and 5 mg/L.

The Mg^{2+} ion release rates of Mg-based samples were calculated based on the measurements of Mg^{2+} ion concentration. Briefly, the Mg^{2+} ion concentration in the Media group ($C_{i,\ media}$), i.e., the baseline Mg^{2+} ion concentration, was subtracted from the Mg^{2+} ion concentration measured in the Mg and Mg alloy groups ($C_{i,\ alloy}$) to obtain the actual concentration of Mg^{2+} ions released from the degradation of each sample ($C_{f,\ deg}$), i.e., $C_{f,\ deg}=C_{i,\ alloy}-C_{i,\ media}$. The total mass of Mg^{2+} ions released (M) was calculated by multiplying $C_{f,\ deg}$ with the total media volume (V; 4 mL), i.e., $M= C_{f,\ deg} \times V$. Mg^{2+} ion release rates (R) of each sample in HUC culture was calculated as $R= M/S/t$, i.e., the total mass of Mg^{2+} ions released (M) from each sample divided by the surface area (S) of the sample and the duration (t) of the culture.

2.7 Statistical Analysis

A one-way analysis of variance (ANOVA) was used to examine the statistical differences among all the groups of interest. Tukey *post-hoc* test was used for detecting statistical differences when comparing two different groups. The plotted data in the graphs represent average values ± standard deviation. A statistically significant difference was considered at $p < 0.05$.

3. Results

3.1 XPS Analysis of PLL Coating on Mg

The survey scan of XPS analysis for Mg_PLL did not show significant peaks of C and N, since only a monolayer of PLL was expected on the surface. Major peaks, such as Mg KLL, O 1s, O KLL and Mg 1s, were observed on both the Mg_PLL and Mg as indicated in Figure 41a, which represented Mg and the oxides formed during the PLL

coating process. A detailed scan of C and N did show the increase of intensity for C and N on Mg_PLL when compared with non-coated Mg (Figure 41a1, Figure 41a2), and the appearance of N peak on Mg_PLL but not on Mg (Figure 2a2). In comparison, the survey scan of XPS analysis for Glass_PLL did not show significant peaks of C and N, either. Major peaks, such as Si 2s, Si 2p, O 1s and O KLL, appeared on both the Glass_PLL and non-coated glass, as shown in Figure 41b, which was expected for the glass substrate. A detailed scan of C and N confirmed the presence of the C and N peaks, and showed that the intensity of C and N peaks increased significantly after the PLL was coated on the glass, as shown in Figure 41b1 and Figure 41b2.

3.2 Cytocompatibility of the HUCs with Mg Alloys

3.2.1 Direct Culture

In direct culture, no HUCs were found on the surface or underneath the MgY, AZ31 and Mg substrates, and no HUCs were found underneath the PU control and the glass reference, but there were HUCs directly adhered onto the PU control and the glass reference after 24 hours (images not shown). This indicated that the degradation of Mg-based substrates possibly prevented or interrupted direct attachment of HUCs. In contrast, there were HUCs adhered onto the tissue culture plate around all the Mg-based substrates, as shown in Figure 42 (24hrs_D row).

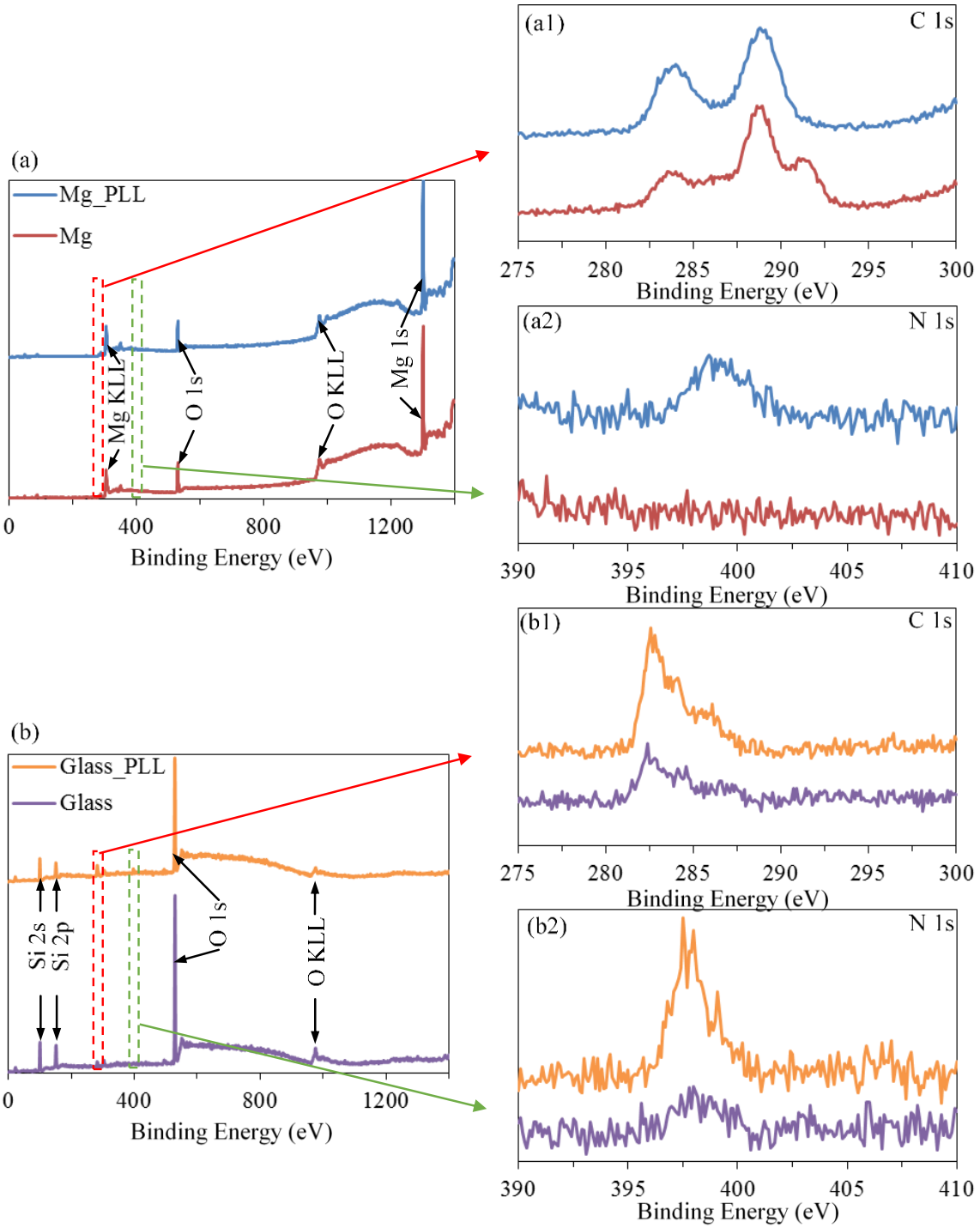

Figure 41 XPS spectra of PLL-coated Mg and glass as well as their respective non-coated controls. (a) PLL-coated Mg in blue, non-coated Mg in red, and (b) PLL-coated glass in orange, non-coated glass in purple. (a1, a2) Magnified XPS spectra for C 1s and N 1s peaks from Mg substrates respectively, and (b1, b2) magnified XPS spectra for C 1s and N 1s peaks from glass substrates respectively.

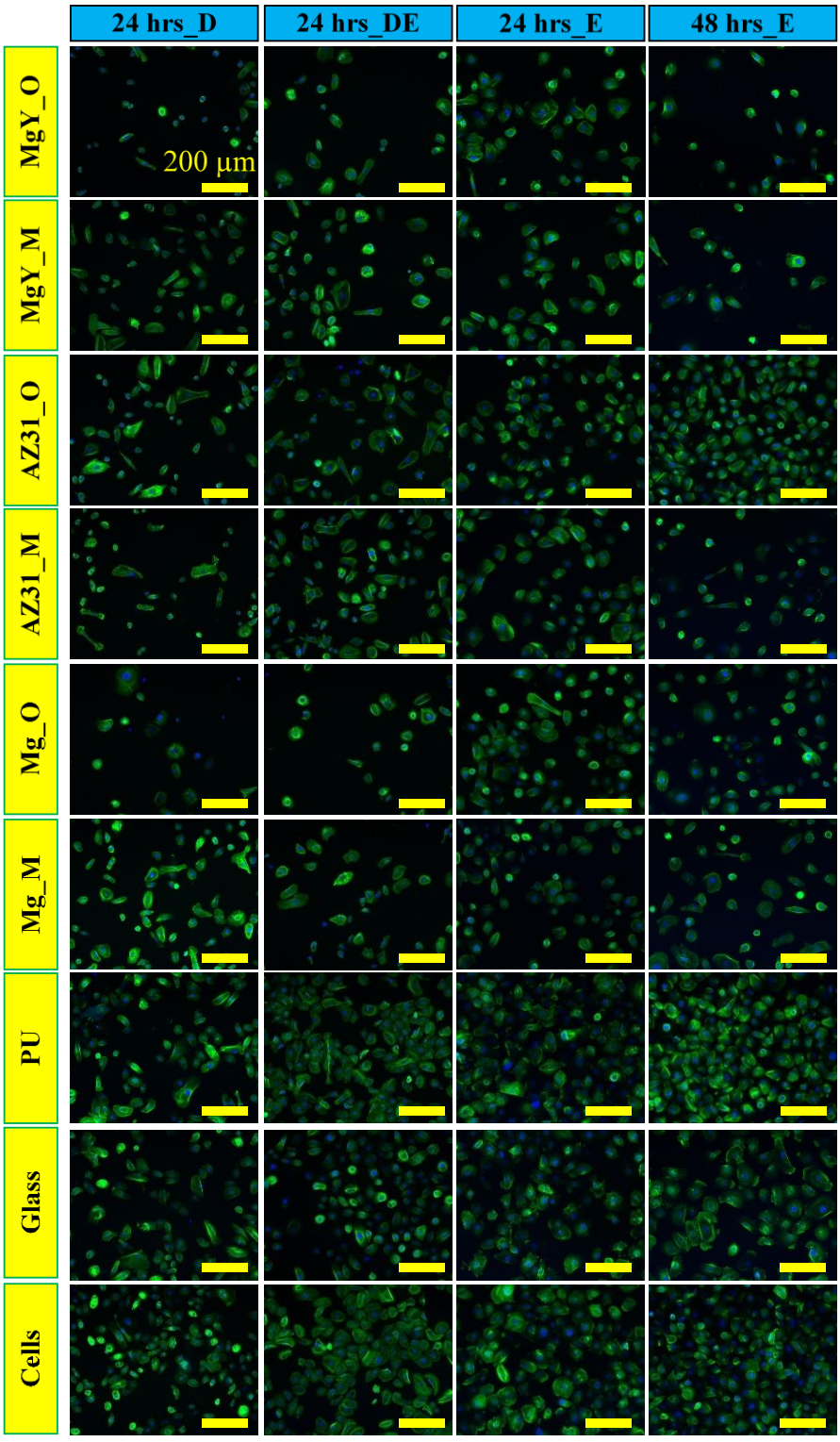

Figure 42 Representative fluorescence images of HUCs adhered on the well plates after cultured with each group of materials of interest under direct culture (D), direct exposure culture (DE), or exposure culture (E). Scale bar = 200 μm for all images. Original magnification: 100×.

Since there were no HUCs directly attached onto the surfaces of Mg-based substrates, only the cells attached onto the tissue culture plates around the samples (indirect contact) were quantified, as, show in Figure 43a (24hrs_D). Statistically significant difference was found among these groups after the culture [$F(8,18)=46.1$, $p=0.034$]. The average adhesion density of HUCs was slightly lower when cultured with MgY, AZ31 and Mg substrates in 24 hrs_D culture. HUCs on the well plates showed an increasing cell density when cultured with the PU control, indicating cell proliferation. HUCs cultured with the glass reference or the cells only control groups showed similar cell density as the initial. Statistically significant difference was detected when comparing MgY, AZ31 and Mg substrates with the PU control. MgY_O and Mg_O showed a lower cell density in average when compared with other Mg-based groups, but no statistically significant difference was detected. When comparing the oxidized with the metallic surface conditions, HUC density showed no statistically significant difference for each pair of Mg-based substrates in 24 hrs_D, i.e., no difference between MgY_O and MgY_M, between AZ31_O and AZ31_M, and between Mg_O and Mg_M.

The spreading area of HUCs in 24 hrs_D indicated statistically significant difference among all samples after normalized by the cell group [$F(7,16)=4.27$, $p=0.005$], as shown in Figure 43b. The average spreading area of Mg_O substrates were found to be statistically lower than that of MgY_M, AZ31_O, and PU. When comparing the oxidized with the metallic surface conditions, HUC spreading area showed no statistically significant difference for each pair of Mg-based substrates in 24 hrs_D, i.e., no difference between MgY_O and MgY_M, between AZ31_O and AZ31_M, and between Mg_O and

Mg_M. The aspect ratio of HUCs after cultured in 24 hrs_D indicated no statistically significant difference among the different groups as shown in Figure 43c. The average aspect ratio of MgY and PU group was higher than that of the other groups, but not statistically significant.

3.2.2 Direct Exposure Culture

In direct exposure culture, HUCs directly underneath the MgY, AZ31 and Mg substrates were found dead after 24 hours, suggesting that the MgY, AZ31 and Mg substrates killed the cells that were in direct contact. In contrast, HUCs were viable and exhibited normal morphology under the PU and glass substrates (image not shown). Meanwhile, HUCs were found viable around the Mg-based substrates (indirect contact in direct exposure culture), as shown in Figure 42 (24hrs_DE row).

Since there were no HUCs survived directly underneath the Mg-based substrates, only the cells attached onto the tissue culture plates around the samples (indirect contact) were quantified, as shown in Figure 43 (24hrs_DE). Statistically significant difference was found among the groups in direct exposure culture [$F(8,18)=34.68$, $p<0.0001$]. HUC density decreased when cultured with the Mg-based substrates, while the cell density remained stable for the PU control, glass reference, and the cells only reference. Statistically significant difference was found between MgY groups and the control groups of PU, glass reference, and the cells only. MgY_O and Mg_O showed the lower cell density in average, and AZ31_O and AZ31_M showed higher cell density in average, but no statistically significant difference was detected among the Mg-based substrates. In addition, no statistically significant difference was found when comparing the oxidized surface

versus metallic surface for each Mg-based substrate pair in 24 hrs_DE, i.e., no difference between MgY_O and MgY_M, between AZ31_O and AZ31_M, and between Mg_O and Mg_M.

The spreading area of HUCs in 24 hrs_DE showed no statistically significant difference among all samples after normalized by the cell only control group, as shown in Figure 43b. The average spreading area of Mg_O substrates were found to be the lowest and PU was the highest. The aspect ratio of HUCs after cultured in 24 hrs_D showed no statistically significant difference among the different groups as shown in Figure 43c.

3.2.3 Exposure Culture

In exposure culture, HUCs were found to attach on the well plates when cultured with Mg-based substrates as shown in Figure 42 (24hrs_E row). Viable HUCs were also found underneath the Mg-based substrates (a 0.9 mm distance was kept). The exposure culture was carried out for another 24 hours to observe HUCs for a longer exposure time, as shown in Figure 42 (48hrs_E row). Adherent HUCs were found when cultured with the Mg-based substrates after 48 hours of exposure culture. Similarly, viable HUCs were found underneath the Mg-based substrates.

The HUC density after exposure culture with the Mg-based substrates and the controls was quantified, as shown in Figure 43a (24hrs_E and 48hrs_E). Statistically significant difference was detected among the groups in 24 hrs_E [$F(8,18)=30.11$, $p<0.0001$) and in 48 hrs_E [$F(8,18)=20.11$, $p<0.0001$]. MgY showed a statistically significant lower cell density than the PU control, glass reference and the cells only groups. Among all the Mg-based substrates, AZ31 showed a higher cell density in average, but no

statistically significant difference was detected. In contrast, HUC density increased after 24 hours of exposure culture with the PU control, glass reference and the cells only groups, indicating cell proliferation. After 48 hours of exposure culture, MgY further decreased cell density as compared with its counterpart in 24 hrs_E, and showed statistically significant lower cell density than the PU control, glass reference and the cells only groups. After 48 hours of exposure culture, AZ31 continued to show a higher cell density in average among all the Mg-based substrates, but no statistically significant difference was detected. HUCs further proliferated in the control groups of PU, glass reference and the cells only after 48 hrs_E. In 24 hrs_E or 48 hrs_E, no statistically significant difference was found when comparing the oxidized surface versus metallic surface for each Mg-based substrate pair, i.e., no difference between MgY_O and MgY_M, between AZ31_O and AZ31_M, and between Mg_O and Mg_M.

The spreading area of HUCs in 24 hrs_E and 48 hrs_E indicated statistically significant difference among all samples after normalized by the cells only control group [$F(7,16)=12.57$, $p<0.0001$], [$F(7,16)=17.56$, $p<0.0001$], as shown in Figure 43b. The average spreading area of HUCs cultured with the Mg substrates were found to be lower than that of the other group; specifically Mg_O was statistically lower than MgY, AZ31, PU and glass. After 48 hrs_E, the average spreading area of HUCs cultured with MgY, AZ31, and Mg_M reduced; specifically MgY showed statistically lower than that of PU and glass. When comparing the oxidized with the metallic surface conditions, HUC spreading area showed no statistically significant difference for each pair of Mg-based substrates in 24 hrs_E and 48 hrs_E, i.e., no difference between MgY_O and MgY_M,

between AZ31_O and AZ31_M, and between Mg_O and Mg_M. The aspect ratio of HUCs after cultured in 24 hrs_E and 48 hrs_E indicated no statistically significant difference among different groups, as shown in Figure 43c. The average aspect ratio of Mg_O was found to be lower than that of the other groups in 48 hrs_E, but not statistically significant.

3.2.4 Comparison of HUC Behaviors under Three Different Culture Methodologies

When comparing the cell density of three different culture methods at 24 hours in Figure 43a, i.e., 24 hrs_D, 24 hrs_DE, 24 hrs_E, MgY showed no statistically significant difference in cell density as compared to the cells only control group in 24 hrs_D, but showed significantly lower cell density than the cells only control group in 24 hrs_DE and 24 hrs_E. However, AZ31 and Mg showed no statistically significant difference in cell density as compared with the cells only control after 24 hours of culture under three different conditions, i.e., 24 hrs_D, 24 hrs_DE, 24 hrs_E, even though AZ31 and Mg showed higher cell density in average in 24 hrs_E than their counterparts in 24 hrs_D and 24 hrs_DE.

When comparing the spreading area of HUCs under the three different culture methods at 24 hours in Figure 4b, Mg_O showed lower HUC spreading area than the other groups in average in all three culture methods, and statistically lower than the PU control in 24 hrs_D and 24 hrs_E. The aspect ratio of HUCs showed no statistically significant difference for the three different culture methods when comparing the respective sample groups, as shown in Figure 4c. The surface conditions of Mg-based substrates, i.e., oxidized versus metallic, did not have any significant effects on the density, spreading area and aspect ratio of HUCs under the three different culture methods.

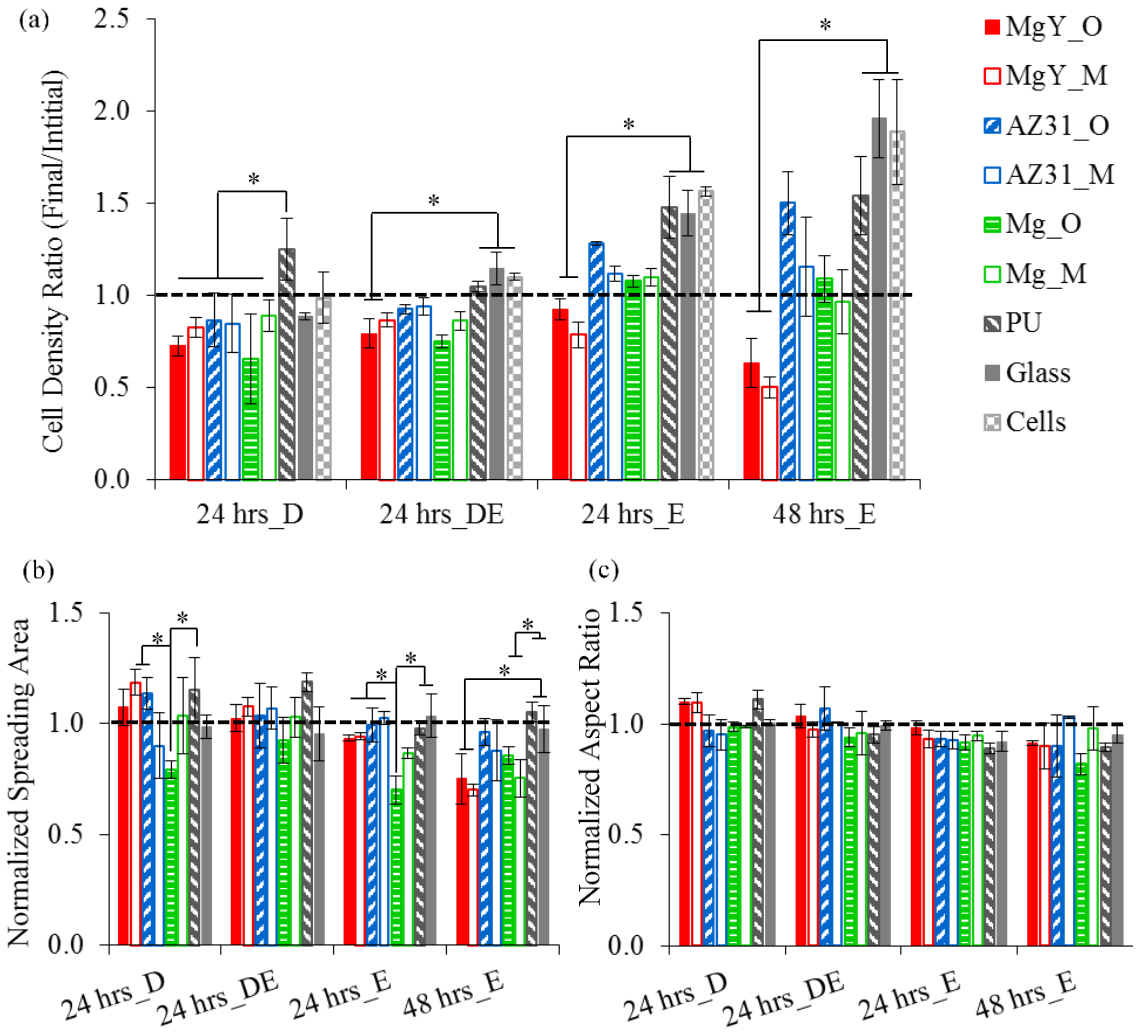

Figure 43 HUC behaviors after cultured with the materials of interest under direct culture (D), direct exposure culture (DE), or exposure culture (E). (a) Cell density ratio (final/initial cell density) of each group after culture. The cell seeding density of 10,000 cells/cm2 was used as initial cell density for 24 hrs_D, and the cell adhesion density before sample introduction (calculated based on the phase images) was used as initial cell density for 24 hrs_DE, 24 hrs_E and 48 hrs_E. (b) Normalized spreading area of adhered HUCs. Average spreading area of adhered HUCs in the cultures with the substrates of interest was normalized by the cells only control group of each culture. (c) Normalized aspect ratio (Dmax/Dmin) of adhered HUCs. Average aspect ratio of adhered HUCs in the cultures with the substrates of interest was normalized by the cells only control group of each culture. Data are mean ± standard deviation (N=3); *p<0.05.

3.3 Degradation of Mg Alloys in Urothelial Cell Culture

3.3.1 Surface Morphology of the Substrates before and after the Culture

Before the culture, the SEM images of MgY_O, AZ31_O, and Mg_O showed random precipitates that are most likely to be oxides or hydroxides, while the SEM images

of MgY_M, AZ31_M, and Mg_M showed traces of scratch lines, typical for surfaces polished using SiC abrasive papers, as shown in Figure 44 (0 hr row). The EDS data in Figure 6a confirmed the presence of Mg, oxygen (O) and carbon (C) on MgY_O, AZ31_O, and Mg_O. In contrast, the samples with metallic surface showed predominantly Mg, with much less amount of O than their oxidized counterparts, and without C. PU substrates showed flat surface with particulate features that were most likely from doping metals. The EDS data in Figure 6a indicated that the PU was mainly composed of C and O as well as a small quantity of Bi (4 wt. %) which was likely the metal dopant. Glass showed smooth flat surface before the culture, and EDS data in Figure 6a confirmed the main elemental component was O, silicon (Si) and sodium (Na).

After all cultures, MgY showed more aggressive degradation, namely localized corrosion and penetrated cracks (Figure 44 column 1-2), as compared with the other Mg-based substrates. In Figure 44 column 3-6, AZ31 and Mg showed similar degradation morphology with cracks across the whole surface under 24 hrs_D and 24 hrs_E, while the AZ31 and Mg under 24 hrs_DE showed some dark spots, possibly caused by direct contact with cells. When comparing oxidized versus metallic surfaces, MgY_O and MgY_M surfaces showed different degradation morphologies, while the difference between surface conditions (oxidized versus metallic) in the groups of AZ31 and Mg was insignificant. MgY_O showed more aggressive degradation when compared with MgY_M, as indicated by significant loss of surface integrity and aggressive propagation of cracks. The PU and glass substrates did not degrade, but did show the deposition of media components (Figure 44 column 7-8).

The EDS results in Figure 45 showed that the substrates with metallic surface had a significant increase of O in weight percentage after all the cultures, likely resulted from the reactions between Mg and the media that created a degradation layer on the surface. In contrast, the oxidized surfaces showed less significant increase in O content when comparing before and after culture. Furthermore, the detection of C and other elements on the Mg-based substrates after culture also suggested deposition of degradation products and media components on the surface. The EDS results confirmed the main components of PU and glass, such as O and Si, which showed no significant change after all the cultures. The detection of Na on PU as well as C on glass after all the cultures indicated deposition of media components on the surfaces of PU and glass. The culture methodologies, i.e., direct, direct exposure and exposure culture, did not seem to have any significantly different effect on the surface morphology of Mg-based samples, except that some dark spots in 24 hrs_E were observed and might be a result of direct contact with the cells, based on SEM images in Figure 45. Surface elemental composition of the substrates showed no significant difference under different culture methodologies, as confirmed in EDS results in Figure 45.

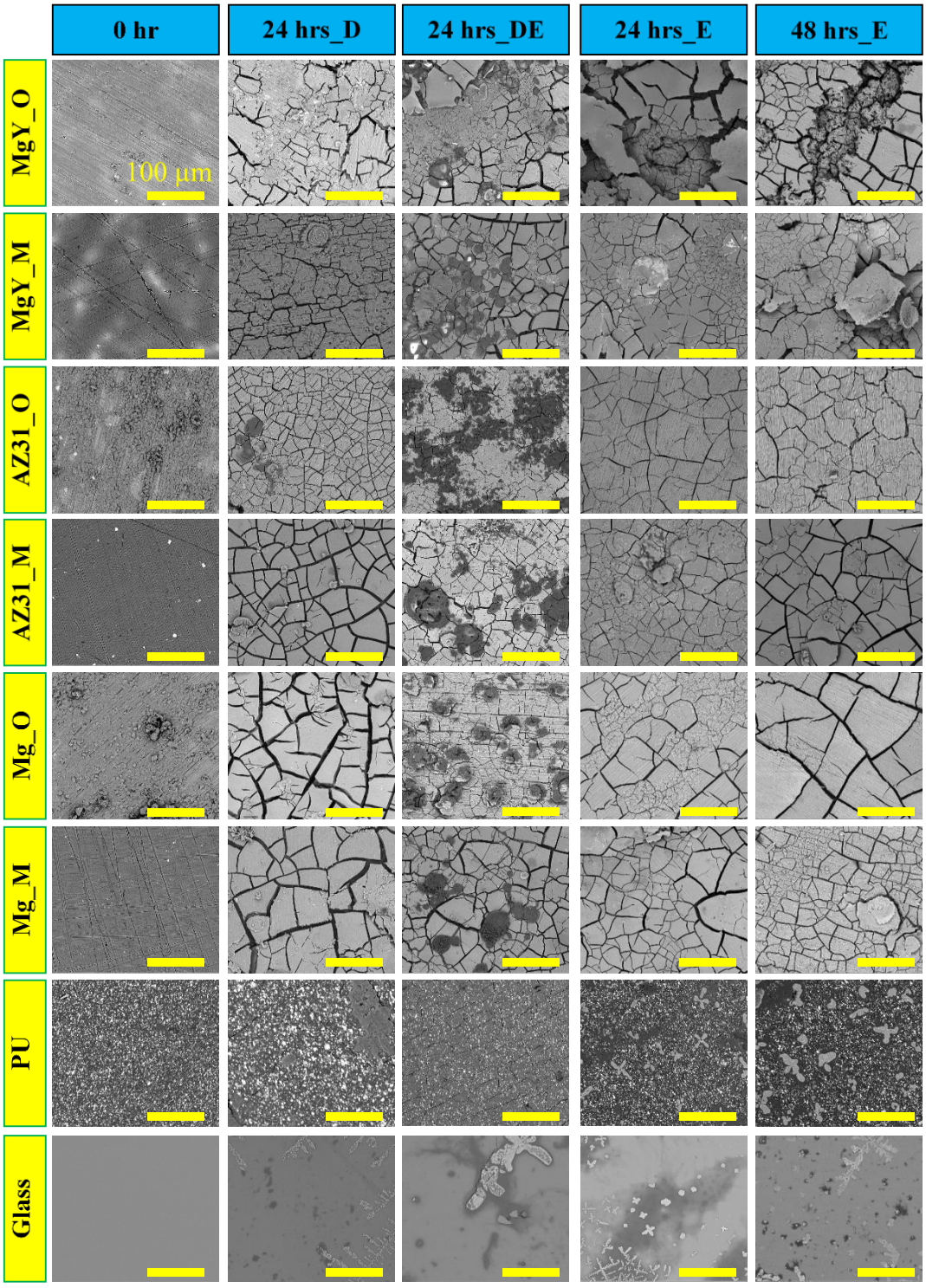

Figure 44 SEM images of each substrate before (0 hr) and after cultured with the cells under direct culture (D), direct exposure culture (DE), or exposure culture (E). Scale bar = 100 µm for all images. Images were taken at an acceleration voltage of 10 kV with an original magnification of 500x.

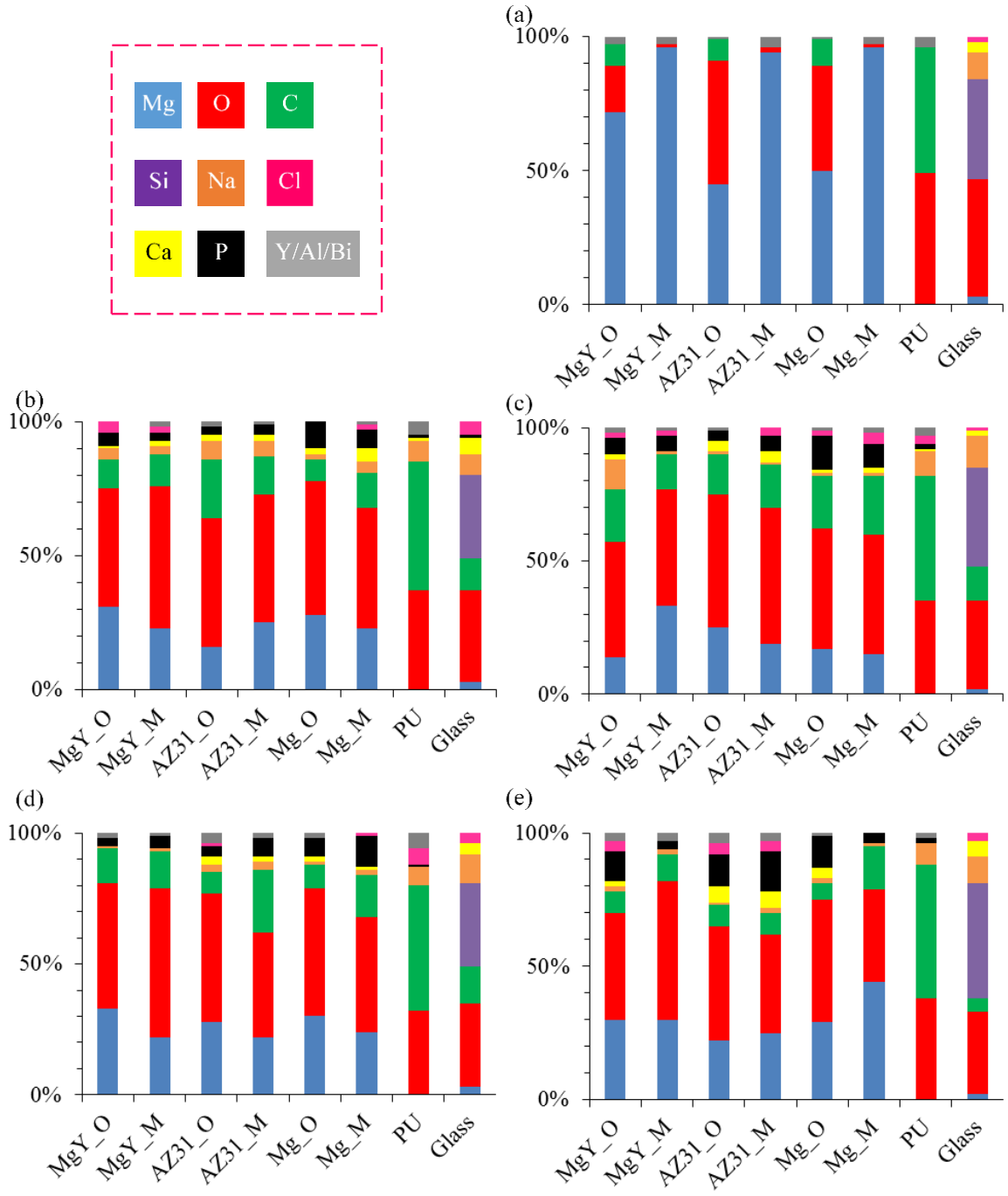

Figure 45 Surface elemetal compositions of diffrent substrates before and after cultured with HUCs. (a) Before the samples were cultured with HUCs. (b) After the samples were cultured with HUCs under direct culture (D) for 24 hours. (c) After the samples were cultured with HUCs under direct exposure culture (DE) for 24 hours. (d, e) After the samples were cultured with HUCs under exposure culture (E) for 24 hrs and 48 hours, respectively.

3.3.2 Mass Change of the Substrates

After all the cultures, mass ratio (final/initial) of each substrate was calculated and plotted in Figure 46. There were no statistically significant differences found in 24 hrs_E, 24 hrs_DE and 24 hrs_E, but statistical difference was detected in 48 hr_E [$F(7,16)=18.72$, $p<0.0001$). Among all the substrates, mass change of MgY samples showed the largest standard deviation, and the statistically significant difference was only found between MgY and the other substrates under 48hrs_E (Figure 46). AZ31 and Mg as well as PU and glass controls after all the cultures showed no significant change in mass when compared with their initial mass.

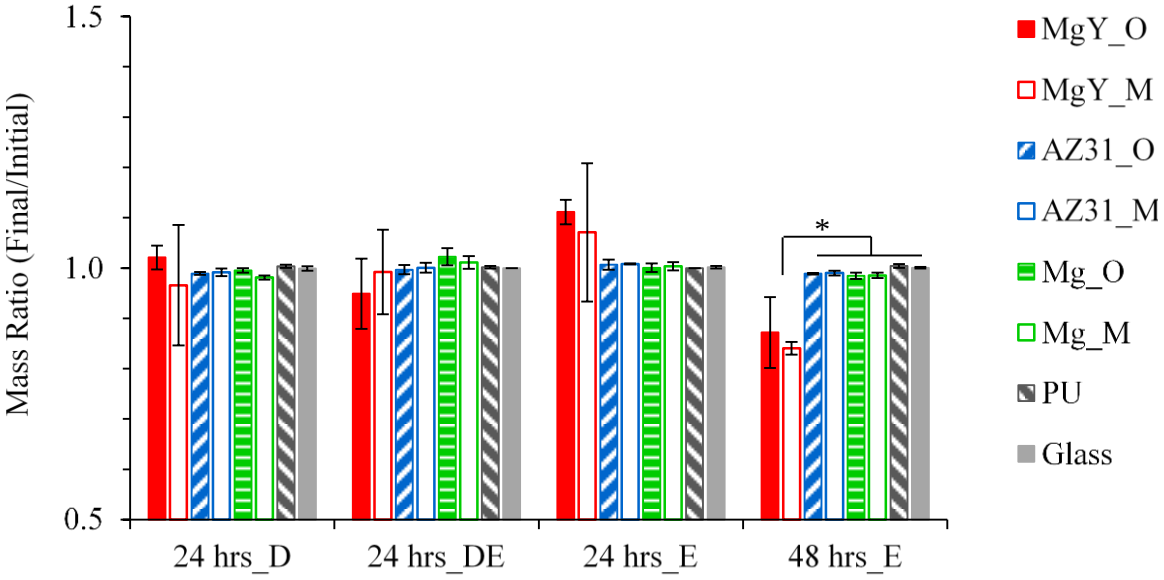

Figure 46 Mass change ratio (final/initial mass) of the samples after cultured with the cells under direct culture (D), direct exposure culture (DE), or exposure culture (E). Data are mean ± standard deviation (N=3); *p<0.05.

When comparing oxidized versus metallic surfaces, no statistically significant difference was detected for each pair of Mg-based substrates. However, MgY_O showed more mass gain in average than MgY_M under 24 hrs_D and 24 hrs_E, and more mass

loss in average under 24 hrs_DE, indicating more aggressive degradation of MgY_O than MgY_M.

3.3.3 The pH of the Collected Media

The pH values of the media collected after each culture are summarized in Figure 47. Statistically significant difference was found in 24 hrs_D [$F(9,20)=279.8$], 24 hrs_DE [$F(9,20)=73.47$], 24 hrs_E [$F(9,20)=48.69$] and 48 hrs_E [$F(9,20)=86.59$], respectively; and all the *p* values were less than 0.0001. The pH of media increased when cultured with the Mg-based substrates. The control groups of PU, glass and cells only did not show any significant pH change as compared with the blank media. Statistically significant difference was detected when comparing the Mg-based substrates with the PU control, glass reference, cells only group, and blank media reference. In 48 hrs_E study, the AZ31 showed statistically lower pH value as compared with that of MgY and Mg (Figure 47).

The differences in pH between surface conditions of oxidized versus metallic in each pair of Mg-based substrates (MgY, AZ31 and Mg) were not statistically significant, i.e., no statistically significant difference was detected between MgY_O and MgY_M, between AZ31_O and AZ31_M, and between Mg_O and Mg_M. The three different culture methods did not have any significant effects on the pH change of the media for each sample group.

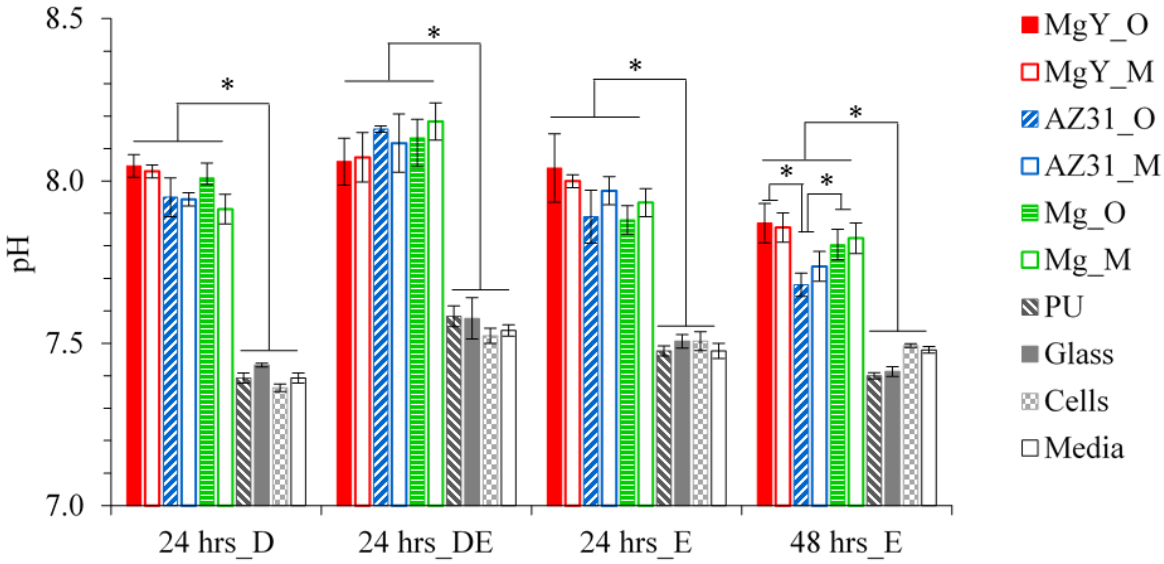

Figure 47 The pH values of the media collected from each well after cultured with the materials of interest under direct culture (D), direct exposure culture (DE), or exposure culture (E) for the prescribed time. Data are mean ± standard deviation (N=3); *p<0.05

3.3.4 Mg^{2+} Ion Concentration in the Collected Media

The Mg^{2+} ion concentration in the media cultured with different samples is summarized in Figure 48. Statistically significant difference was found in 24 hrs_D [F(9,20)=82.90], 24 hrs_DE [F(9,20)=46.19], 24 hrs_E [F(9,20)=35.06) and 48 hrs_E [F(9,20)=53.64], respectively, and all the p values were less than 0.0001. As compared with the blank media, the media cultured with the Mg-based substrates showed an increase in Mg^{2+} ion concentrations, while the media for the PU, glass, and the cells only control groups showed no significant change. Statistically significant difference in Mg^{2+} ion concentrations was detected when comparing the Mg-based substrates with the PU, glass, the cells only and media groups. MgY showed a greater Mg^{2+} ion concentration in average than the other Mg-based substrates after all the culture. Statistically, MgY showed significantly greater Mg^{2+} ion concentration than AZ31 and Mg_M (but not Mg_O) in 24 hrs_D; MgY showed significantly greater Mg^{2+} ion concentration than AZ31 and Mg in 24

hrs_DE; and MgY also showed significantly greater Mg^{2+} ion concentration than AZ31 and Mg in 24 hrs_E and 48 hrs_E. In addition, MgY showed greater Mg^{2+} ion concentration in 24 hrs_E than its counterpart in 48 hrs_E because the media was changed at 24 hours and the degradation rate of MgY decreased in the second 24 hours, i.e., 48 hrs_E.

When comparing oxidized versus metallic surfaces for each pair of Mg-based substrates, no statistically significant difference was detected, although in average MgY_O showed greater Mg^{2+} ion concentration than MgY_M. The three different culture methods did not have any significant effects on the Mg^{2+} ion concentration in the media for each respective sample group.

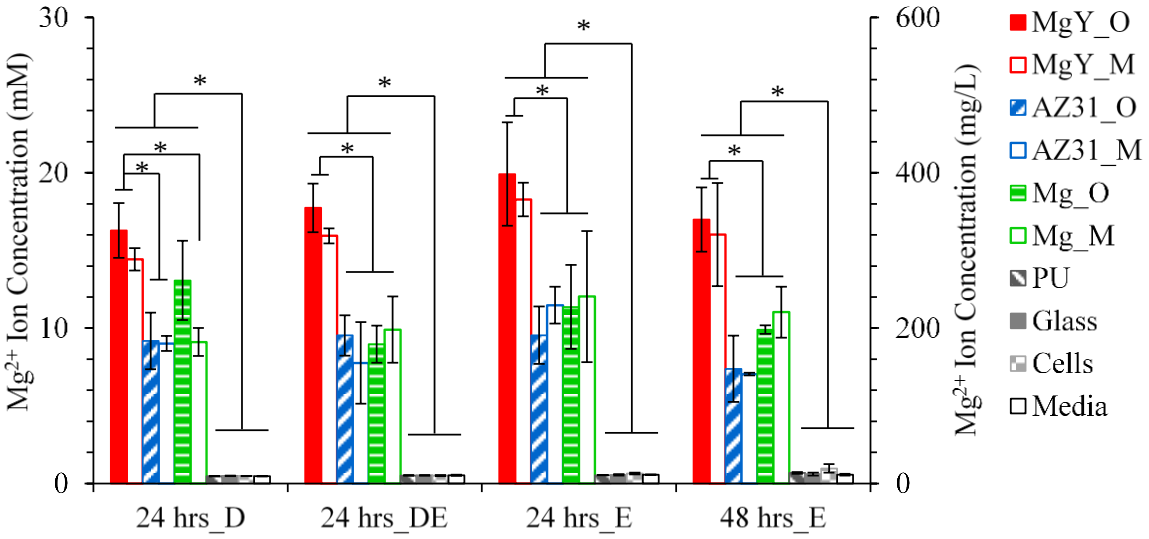

Figure 48 Mg^{2+} ion concentration in the media collected from each well after cultured with the materials of interest under direct culture (D), direct exposure culture (DE), or exposure culture (E). Data are mean ± standard deviation (N=3); *p<0.05.

3.3.5 The Release Rate of Mg^{2+} Ions in Urothelial Cell Culture

The release rate of Mg^{2+} ions for each Mg-based substrate under each culture method was calculated and plotted in Figure 49. The release rate of Mg^{2+} ions was used to estimate the degradation rate of Mg-based substrates in the HUC culture. Statistically

significant difference was confirmed in 24 hrs_D [F(5,12)=38.66], 24 hrs_DE [F(5,12)=53.68], 24 hrs_E [F(5,12)=22.59], and 48 hrs_E [F(5,12)=27.19], respectively; all the *p* values were less than 0.0001. MgY showed significantly higher degradation rate compared with the other Mg-based substrates in every culture method. AZ31 and Mg showed similar degradation rates in every culture method without any statistically significant differences.

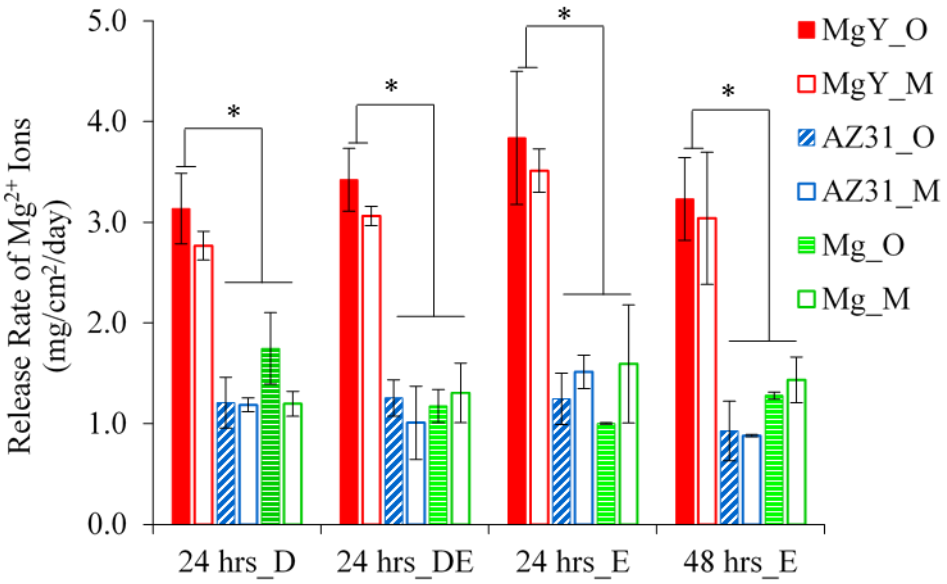

Figure 49 The release rate of Mg^{2+} ions (mg/cm^2/day) for Mg alloys and Mg under direct culture (D), direct exposure culture (DE), or exposure culture (E). The plotted values were calculated based on the measurement of Mg^{2+} ion concentration and sample surface area. Data are mean ± standard deviation (N=3); *p<0.05

MgY_O had a higher degradation rate in average compared with MgY_M in every culture method, but no statistically significant difference was detected between them. The difference in degradation rates for AZ31 and Mg with oxidized versus metallic surface was not statistically significant. In summary, these alloys of different surface conditions showed a degradation rate from rapid to slow following the order of (MgY_O, MgY_M) > (AZ31_O, AZ31_M, Mg_O, Mg_M), which was similar for all three culture methods

(Figure 49). The release rate of Mg2+ ions suggested three different culture methods did not have any significant effects on the degradation rate of each Mg-based substrate in urothelial cell cultures.

4. Discussion

4.1 In Vitro Cell Culture Methodologies for Mg-Based Bioresorbable Ureteral Stents

Adequate cytocompatibility with relevant cells is always a key requirement for any biomaterials used in implanted medical devices. The *in vitro* experiments should closely represent *in vivo* conditions, in order to provide meaningful results. Current ISO standards for *in vitro* cytotoxicity testing are not ideal for evaluating Mg-based bioresorbable materials[102-103]. Several early attempts on developing suitable *in vitro* evaluation methods have been reported recently[102, 104], but no consensus yet in the field of bioresorbable metals.

Standardized testing methods would be beneficial for consistent and comparable evaluation of Mg-based bioresorbable metals for potential clinical translation, but not available yet. For the instance of orthopedic or musculoskeletal applications, it is desirable for the relevant bone cells to directly attach and proliferate on the material surface for new bone growth. Cipriano *et al.* established the direct culture method *in vitro* to examine cell-material interactions at the interface when the cells were seeded directly on the top of Mg alloy substrates, and reported that bone marrow derived mesenchymal stem cells (BMSCs) directly adhered on the surface of four Mg-xZn-0.5Ca (x = 0.5, 1, 2, 4, wt. %) alloys, promising for bone regeneration[102]. For urological device applications, the direct culture method was adapted in this study to determine the possibility for HUCs to attach onto the

surface of Mg alloys directly. However, excessive cell adhesion and proliferation on the surface of ureteral stents may not be necessary or desirable. Some patients experienced undesirable granulation and epithelial tissue ingrowth after implantation of ureteral stents, as reported in literature. Moreover, before insertion of ureteral stents, HUCs are already well established in the ureter lining; after stent implantation, the stent material will be in direct or indirect contact with well-organized human cells in the body. Thus, in this study, direct exposure culture and exposure culture were designed to represent direct contact and indirect contact conditions, respectively. HUCs were cultured to nearly confluence in the well plates, and the Mg-based substrates were placed in either direct contact with the cells or kept at a distance from the cells using the Transwell® insert. Collectively, these culture methodologies captured different *in vivo* scenarios for ureteral stent applications. The results showed that the three different culture methods explored in this study did influence the HUC behaviors for Mg-based substrate groups, which should be considered when designing *in vitro* cell studies for Mg-based biomaterials.

4.2 Cytocompatibility of Mg and Its Alloys for Urological Device Applications

Mg alloys have shown good cytocompatibility with many different cell models. To our knowledge, this is the first study to demonstrate the cytocompatibility of Mg alloys and their degradation products with HUCs for urological device applications. The degradation of Mg alloys created a dynamic environment near its surface; at the cell-material interface, there are the released ions such as Mg^{2+} and OH^-, the dissociated solid particles or degradation products, and the precipitates onto the substrates from the culture. When the

soluble degradation products (e.g. Mg^{2+} and OH^-) of Mg-based substrates reach certain concentration locally, the environment may become unfavorable for the surrounding cells.

The Mg-based substrates elevated the pH of the media to 8.2 maximum; and none of them reached 8.3 (Figure 47). The highest average pH, i.e., 8.2, was found for Mg_M at 24 hrs_DE. It should be noted that the measured pH was the average pH of the whole media in the wells after cultured with the Mg-based substrates. The degradation of Mg-based substrates is continuous in the media and causes continuous release of OH^- ions, which created a concentration gradient. The closer to the Mg-based substrates, the higher the concentration of OH^- ions, i.e., the higher pH, would be. Thus, the pH of the media near the surface of Mg-based substrates should be greater than the average pH of the whole media. The elevated pH was speculated to be the dominant factor responsible for no HUC attachment directly on the Mg-based substrates in 24 hrs_D, and the death of all HUCs underneath the Mg-based substrates in 24 hrs_DE. In addition, the higher pH after cultured with MgY was believed to be the contributing factor for the reduced HUC density in 24 hrs_E and 48 hrs_E.

The Mg-based substrates elevated the Mg^{2+} ion concentration in the media to 20 mM maximum (Figure 48). The highest average Mg^{2+} ion concentration, i.e., 20 mM, was found for MgY_O in 24 hrs_E, possibly due to the combined effects of the faster degradation of MgY in the HUC culture and more exposed surface area than the 24 hrs_D and 24 hrs_DE. When the Mg^{2+} ion concentration in the media increased to 20 mM, the HUC density decreased and the spreading area of HUCs increased (Figure 2). When comparing the Mg-based substrates (Figure 49), the MgY group elevated Mg^{2+} ion

concentration from 15 to 20 mM during all cultures; the AZ31 group had Mg^{2+} ion concentration less than 10 mM for all cultures. Thus, the MgY group should have reduced the HUC density more than the AZ31 group due to the higher Mg^{2+} ion concentration, which was consistent with the observation in 24 hrs_E and 48 hrs_E in average, although not statistically significant. In 24 hrs_D and 24 hrs_DE, however, the difference in HUC density between the MgY and AZ31 group was not statistically significant. The AZ31 group showed lower cell density ratio in 24 hrs_D and 24 hrs_DE than in 24 hrs_E. This would attribute to the difference among the three culture methodologies, where the HUCs in direct culture were closer to the Mg-based substrates than in exposure culture which had the 0.9 mm distance in height between the substrates and the cells. The HUCs might have been exposed to relatively higher pH and Mg^{2+} ion concentration near the substrate surface in 24 hrs_D and 24 hrs_DE, than that of 24 hrs_E. The high pH and Mg^{2+} ion concentration near the sample surface could be the key factors that affected the HUC adhesion density and morphology.

Other differences between *in vitro* and *in vivo* conditions should be taken into account. For the *in vitro* culture of 24 hrs_DE, the HUCs underneath the Mg-based substrates were exposed to unfavorable environment for a long period of time due to the static culture conditions, which led to cell death. In contrast, urine flows in the urinary tract *in vivo*, which can quickly remove the local degradation products of Mg; and, thus, HUCs are exposed to a relatively stable pH and ionic concentration *in vivo*.

4.3 Degradation of Mg and Its Alloys

Mg degrades by reacting with the water present in the physiological environment[25]. The generated degradation products include Mg^{2+} ions, hydroxide ions (OH^-), hydrogen gas (H_2) (Eq.1) and insoluble degradation products, e.g. $Mg(OH)_2$ (Eq.2) :

$$Mg + 2H_2O \rightarrow Mg^{2+} + 2OH^- + H_2\uparrow \quad (1)$$

$$Mg^{2+} + 2OH^- \rightleftharpoons Mg(OH)_2\downarrow \quad (2)$$

The results of this study showed the degradation rate from rapid to slow following the order of (MgY_O, MgY_M) > (AZ31_O, AZ31_M, Mg_O, Mg_M), consistent with the literature report[16]. Lock et al. investigated the similar group of Mg-based substrates in artificial urine solution, and reported sample degradation rates from rapid to slow following the order of MgY_O > MgY_M > Mg_O > (AZ31, Mg_M)[16].

The degradation rate of Mg may be affected by several factors. The composition of physiological fluids is one of the factors that affect the Mg substrate degradation. Li *et al.* reported the comparison of Mg degradation in SBF with high and low chloride ion concentration, which indicated that chloride ions accelerated the degradation of Mg[105]. The surface condition of Mg-based metals may play an important role in Mg degradation behavior. Johnson et al. demonstrated the degradation behavior of MgY alloys in phosphate buffer saline (PBS) and DI water with two different surface conditions (oxidized versus metallic)[101]. They concluded that the thermally oxidized surface of MgY accelerated the degradation in PBS. Specifically, the porous oxide surface of MgY was undermined locally, causing the oxide layer breaking off and leading to more aggressive localized corrosion. However, in the HUC cultures of this study, no statistically significant differences were

detected in the degradation rate of respective Mg-based substrates with oxidized versus metallic surfaces.

Lastly, the difference in elemental compositions of the Mg alloys also contributed to the degradation behaviors. Yttrium (Y), and Aluminum (Al) were widely used as an alloying element in Mg to increase the corrosion resistance as well as the mechanical properties of Mg. Hänzi et al. concluded that Y could reduce the degradation rate of Mg with a stable Y_2O_3 passivation layer on the surface; alternatively, it could also increase the degradation rate if the passivation layer was instable or undermined by aggressive salt ions[106]. In our study, we observed similar phenomena; the mass of MgY increased at 24 hours and then decreased after another 24 hours of culture. This indicated that a passivation layer formed on the surface of MgY, which initially helped to slow down the degradation, and continued deposition of salts and degradation products on the surface increased the sample mass at 24 hours. However, this passivation layer was not dense and water could easily penetrate through, which resulted in further degradation of the sample and mass decrease after 48 hours of culture. Al can reduce the corrosion rate when doped in Mg alloys. An intermetallic compound, $Mg_{17}Al_{12}$, forms in the Mg-Al alloy. The high fraction of the β phase of $Mg_{17}Al_{12}$ could provide good passivation in a wide range of pH and serve as an anodic barrier to decrease the overall alloy degradation[107-108].

In a summary, in an attempt to establish standard *in vitro* methods for testing bioresorbable Mg/Mg alloys for urological device applications, we proposed and explored three different culture methodologies, i.e., direct culture, direct exposure culture, and exposure culture to mimic cell-biomaterial interactions in different scenario, and studied

their effects on the HUC density and morphology. Direct culture is a desirable *in vitro* method when it is important to evaluate direct cell attachment on the biomaterial surfaces. Direct exposure culture is a suitable *in vitro* method to study how the well-established cells in the body interact with newly implanted biomaterials. Exposure culture method is appropriate to evaluate cell-biomaterial interactions in the same environment, where they are not in direct contact with each other and the distance between them can be adjusted to mimic their relative locations *in vivo*. For urological device applications, each culture methodology may be used independently or collectively to mimic *in vivo* situations dependent on where and how the devices are used for specific clinical application. The results showed differences in HUC behaviors with the same Mg-based substrates when different culture methods were used. Cell-biomaterial interactions at direct versus indirect contact were found to be critical to consider when designing the *in vitro* study for evaluating biodegradable metallic materials.

The Mg-based substrates reduced the HUC viability with direct contact at the cell-material interface in direct culture and direct exposure culture. The faster degrading MgY reduced HUC density as compared with the controls, suggesting degradation rate is a key factor affecting cellular response. Mg-based substrates in the HUC culture showed a degradation rate from fast to slow in the order of MgY> (AZ31, Mg). Mg-based biomaterials, especially the slower degrading alloys such as AZ31, should be further studied to determine their potential to be used for bioresorbable urological devices.

Chapter 9 Effects of Loadings on Magnesium Implants during Degradation

1. Introduction

Magnesium (Mg) has great potentials to serve as next-generation bioresorable implants for medical applications due to their excellent mechanical properties and biocompatibility. Current literatures have also vastly reported the biodegradability of Mg-based implants *in vitro*. However, most of them conducted the experiments with Mg-based implants under free load. Thus, the results of these *in vitro* experiments couldn't provide fully reliable information about the implants in the actual *in vivo* conditions, where the implants are constantly undergo loads and forces inside the human body. Mg is susceptible to stress corrosion cracking (SCC), especially when presents in a humidify environment. Animal studies can provide complimentary information about the Mg-based implants under load before clinical trials. However, the load in small animal models, such as rats, couldn't completely translate to the human study due to the significant difference of musculoskeletal structures between the human and small mammals. In addition, animal studies are always costly for researchers and industries, which also involve in sacrifice of animals.

We developed a loading apparatus can conduct the in vitro study with applied load of bioresorbable implants and current permanent implants, i.e., titanium. The results can help to screen and select the most promising candidate implant before clinical trials, which greatly reduce the cost of research and medical resource. Currently, there is no similar device available on the market. We see a great potential of this device in future applications.

2. Design and Methods

2.1 The Design and Development of the Loading Apparatus

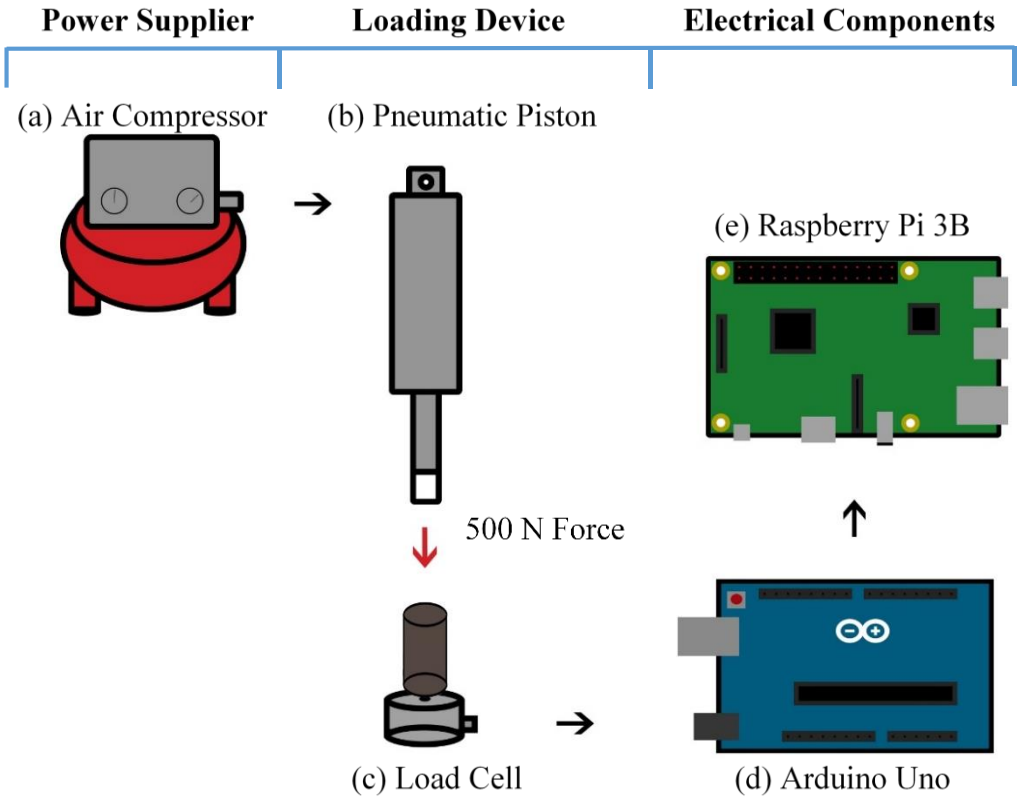

Figure 50: An illustration of the schematic for the loading apparatus, which contains three major components, i.e., power supplier (a), loading device (b, c), electrical components (d, e). Specifically, (a) air compressor sends compressed air to extend the pneumatic piston. (b) The pneumatic piston applies 500 N onto the Mg rod. (c) Load cell that reads up to 200 kg that gathers the load applied to the Mg rod. (d) Arduino Uno powers and gathers force applied from the load cell and transmits it to the Raspberry Pi 3B. (e) Raspberry Pi 3B collects, stores, and streams the data transmitted from the Arduino Uno in real time.

Figure.1 shows the schematic for the loading apparatus. The loading apparatus was designed to select and vary the load applied onto the implant material for testing. It contains three major parts: power supplier (Figure 50a), loading device (Figure 50b, c), electrical components (Figure 50d, e). Specifically, the air compressor (Figure 50a) sends compressed air to extend the pneumatic pistons (Figure 50b), applying a load onto the Mg rods. That force is read by the load cell (Figure 50c) and is transmitted to an Arduino Uno

(Figure 50d). The Arduino Uno sends the data to the Raspberry Pi 3B (Figure 50e) where it is stored and displayed on a monitor at real time.

An implementation of the whole loading apparatus is listed in Figure 51. The air compressor (C2002, Porter Cable, TN, USA), as the power supplier, provides compressed air which ranges from 0 psi to 200 psi to the piston. The loading device contains three pneumatic pistons (4952K354, McMaster-Carr, CA, USA) placed in a frame, which was machined out of stainless steel (McMaster-Carr, CA, USA), and 3D printed out of Poly lactic acid filament (PLA, Makerbot, NY, USA) using a MakerBot Replicator (MakerBot Replicator Desktop 3D Printer, MakerBot, NY, USA). The pistons are made out of stainless steel, have a bore size of one and half inches, and can each output a load up to 1500 Newton's of force by regulating the output pressure of the air compressor. The output force of the pistons is determined as by the following Eqt.1.

$$F = \rho A = \rho \pi d^2 / 4 \qquad (1)$$

Where F is the force exerted, ρ is the gauge pressure, A is the full bore area, and d is the full bore piston diameter. Each piston contains two intake valves (Figure 51b) for air to flow in and to control the extension of the piston. Screws were threaded into tubing and inserted into the one of the two intake valves to help prevent air from leaking. Levels were placed on the frame of the loading device to ensure the pneumatic pistons were perpendicular to the bottom plate, and apply a vertical force onto the Mg rod (Figure 51b). A load cell (TAS606, Sparkfun, CO, USA) is position underneath the middle well. The load cell is capable of reading a maximum of 200 kg.

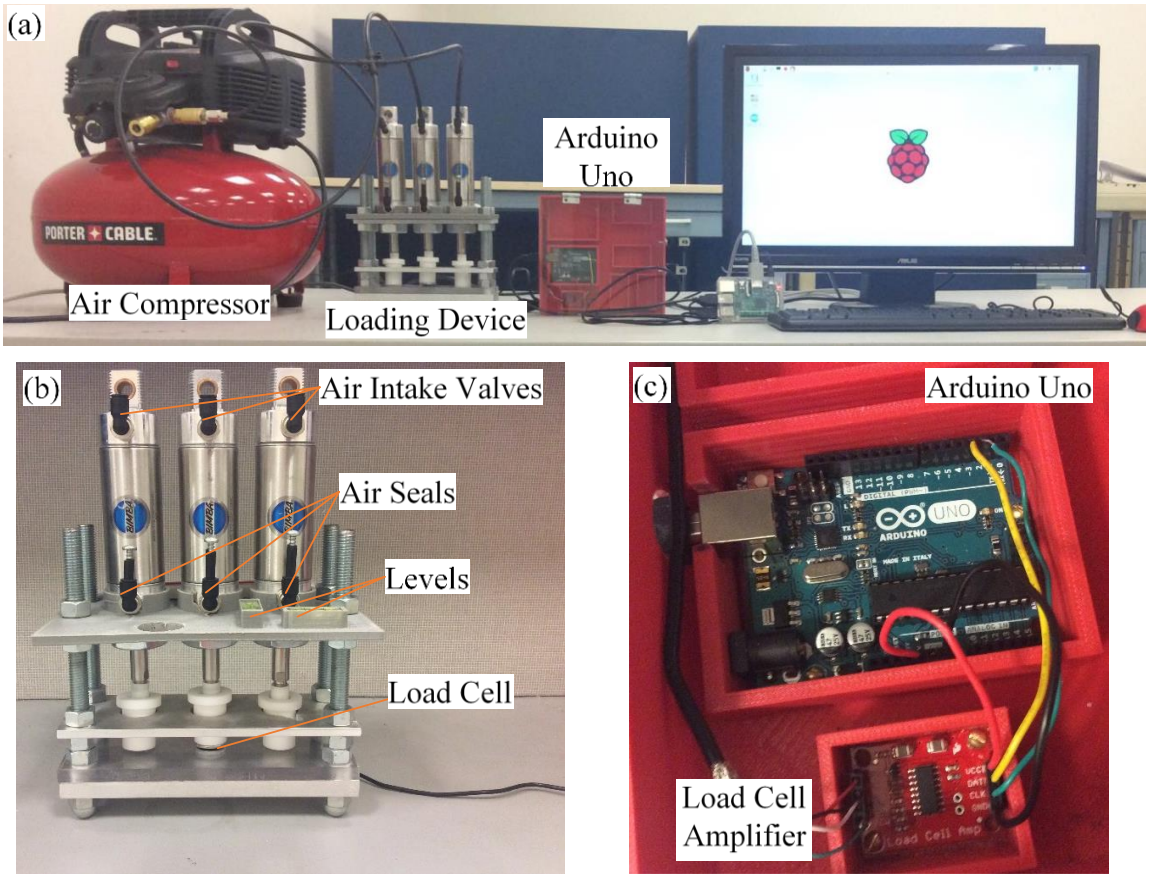

Figure 51 The implementation of the actual loading apparatus. (a) A general overview of the loading apparatus and all of its components. (b) A detail view of the loading device. Air intake valves allow the air sent from the air compressor to extend the pneumatic piston and air seals prevent the incoming air from leaking out of the pistons. Two levels are used to ensure that the pistons are set up to apply a vertical force onto the Mg rod. A load cell is position underneath the middle Teflon well. (c) The electrical components of the apparatus are the microcontroller, Arduino Uno, which gathers and sends data to the Raspberry Pi 3B and the load cell amplifier that amplifies the signal received from the load cell for the Arduino to read accurately.

The electrical components include a load cell amplifier, an Arduino Uno, and a Raspberry Pi. Specifically, the load cell amplifier provides a stronger signal with less noise to the Arduino Uno for accurate data collection (Figure 51c). Arduino Uno (Arduino Uno, Arduino, Turin, Italy) functions as the microcontroller powering both the load cell, and the load cell amplifier (Figure 51c). The Arduino collects the force data received from the load cell amplifier and transmits that to the Raspberry Pi. The Arduino Uno was chosen for its ease of implementation as it can be rapidly applied and modified through its hardware, and

programing. A Raspberry Pi (Raspberry Pi 3B, Raspberry Pi, Cambridge, United Kingdoms) is connected to the Arduino Uno to display the force values on a monitor. Adding the Raspberry Pi 3B allows for streaming and storing of the load applied to the Mg-based implant. The Raspberry Pi 3B was selected as a more cost effective solution to run the programming code and to store the data received from the Arduino Uno instead of using a desktop or laptop. In storing the data and displaying it in real time, the user does not have to be present for the full duration of the study, which can go up to weeks, to monitor the accuracy of the apparatus.

2.2 Degradation of Mg in rSBF with Applied Load

Mg rods (99.95%, GalliumSource, CA, USA) were cut into 15 mm × 6 mm using a handsaw, and then polished using silicon carbide (SiC, Ted Pella Inc., Redding, CA, USA.) paper from 600 grids to 1200 grids. The polished samples were degreased and cleaned using an ultrasonic cleaner (Model 97043-936, VWR, Radnor, PA, USA) in acetone (Sigma Aldrich, St Louis, MO, USA) for 30 min and in 100% ethanol (Sigma Aldrich, St Louis, MO, USA) for 30 min respectively. Before the immersion, all of the Mg samples were weighed using an analytical balance (Ms104S, Mettler Toledo, Columbus, OH, USA), and recorded as the initial mass (M_i).

To avoid the galvanic corrosion caused from the metal to metal contact of the Mg and the piston, the wells and the caps on the pistons were machined out of Teflon. The Mg samples were placed into Teflon wells and immersed in 2.5 mL of revised simulated body fluid (rSBF). Until reaching each immersion time point, a load of 500 N was placed on each Mg rod at room temperature. The Mg controls were also placed in the Teflon wells

respectively and immersed in 2.5 mL of rSBF but without load. The Mg samples were immersed in rSBF for 3 days, 1 week, and 2 weeks. The rSBF media was replenished every other day.

After each immersion period, the rSBF was collected from the wells and the samples were dried in a vacuum (Multipurpose Vacuum Oven, Thermo Scientific, MA, USA) at room temperature. The macroscopic images of the dried Mg samples with or without 500 N were taken using a camera (Model SX500 IS, Cannon). The dried Mg samples were also weighed using an analytical balance to determine the final mass (M_f). The mass change (%) of Mg samples at different time point was then calculated following $(M_f - M_i) / M_i$, i.e., the ratio of difference between final mass (M_f) and initial mass (M_o) to the initial mass (M_o). The pH of the collected rSBF was measured using a pH meter (SB70Pm, SympHony, USA). The Mg^{2+} ion concentrations were quantified using inductive coupled plasma - optical emission spectrometry (ICP-OES; Optima 8000, Perkin Elmer, MA, USA). Briefly, the collected solutions from each well were diluted with DI water by a factor of 1:100 into a total volume of 10 ml. Mg^{2+} ion concentrations were then obtained from calibration curves generated using Mg^{2+} standards (Perkin Elmer) serially diluted to a concentration of 0.5, 1, 2, and 5 mg/L. The characterization process was repeated for each time point. The degradation tests were performed in triplicate for each sample type.

2.3 Statistical Analysis

A one-way analysis of variance (ANOVA) was used to examine the statistical difference among all the different groups. Tukey post-hoc test was used for detecting

statistical differences when comparing between two different groups. All graphs represent average values ± standard deviation. A statistically significant difference was considered at $p < 0.05$.

3. Results

3.1 Surface Morphology and Mass Change of the Mg Samples

The macroscopic images of the Mg under load and Mg controls showed different surface morphologies after 14 days of immersion in rSBF (Figure 52a). Generally, all the Mg samples showed deposition of degradation products after 3 days of immersion. The white degradation products increased as the time increased during the immersion. Mg rods under load, however, had a less degradation products than that of Mg controls, especially at 7 days and 14 days. Figure 52b shows the mass change of the Mg under load and Mg controls after 14 days of immersion in rSBF. Statistically significant difference was found among the Mg-based samples during the 11 days immersion [$F(6,17)=175.7$], $p<0.0001$. All the Mg samples had a significant mass decrease after the immersion. At the 3 days immersion, all the Mg samples had a mass increase due to the deposition of the degradation products. The Mg under load showed a higher mass increase than the Mg controls. Starting at 7 days immersion, all the Mg samples had a significant mass decrease, where the Mg under load showed a significantly higher mass loss than the Mg controls. At 14 days immersion, the mass of Mg controls had no significant change comparing to the previous time point. The mass of Mg under load, however, showed a mass loss which was significantly lower than the Mg controls.

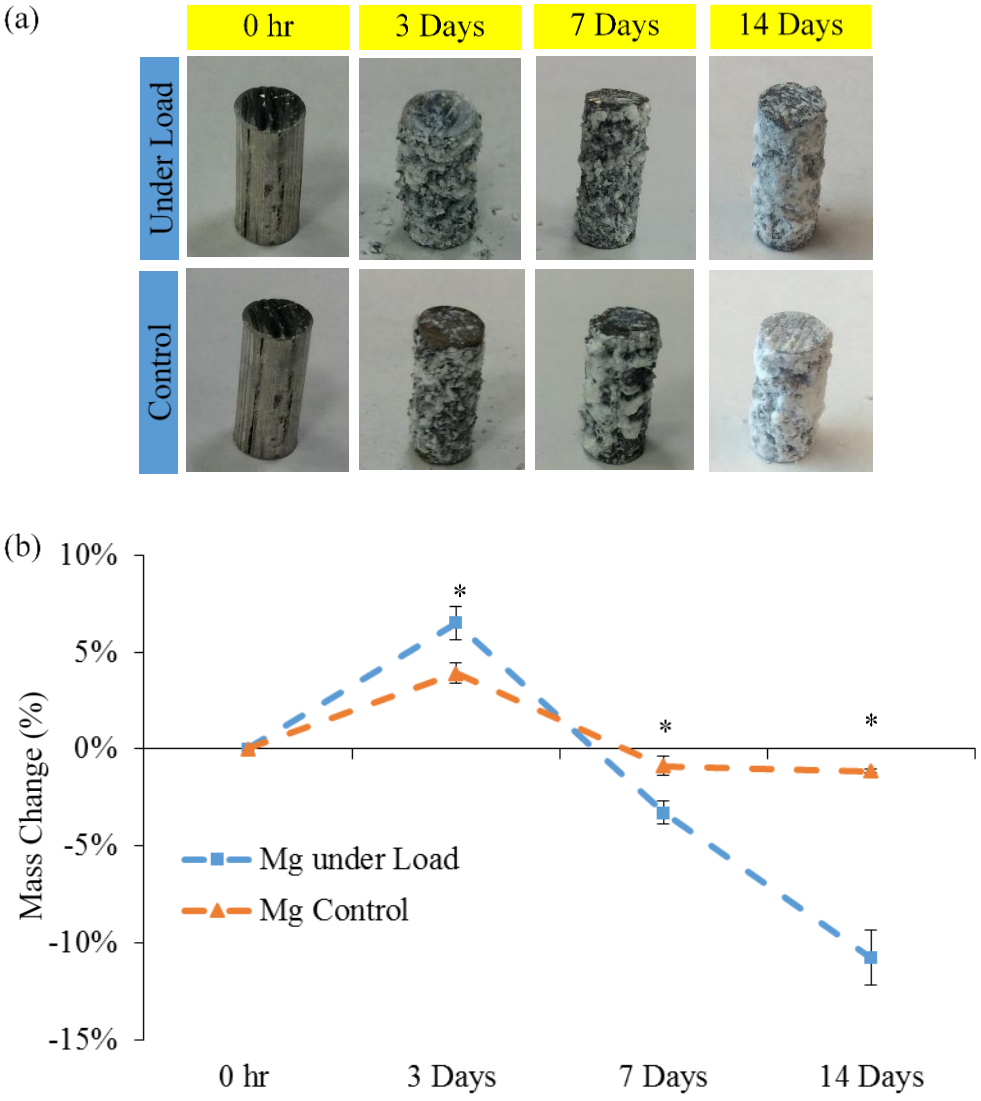

Figure 52 The degradation behaviors of Mg under a compressive load of 500 N comparing to Mg controls during the immersion in rSBF for 14 days. (a) Macroscopic images of both the Mg under load and Mg controls at different time point. (b) The mass change of both the Mg under load and Mg controls in rSBF at different time point. Data are mean ± standard deviation (N=3); *$p<0.05$.

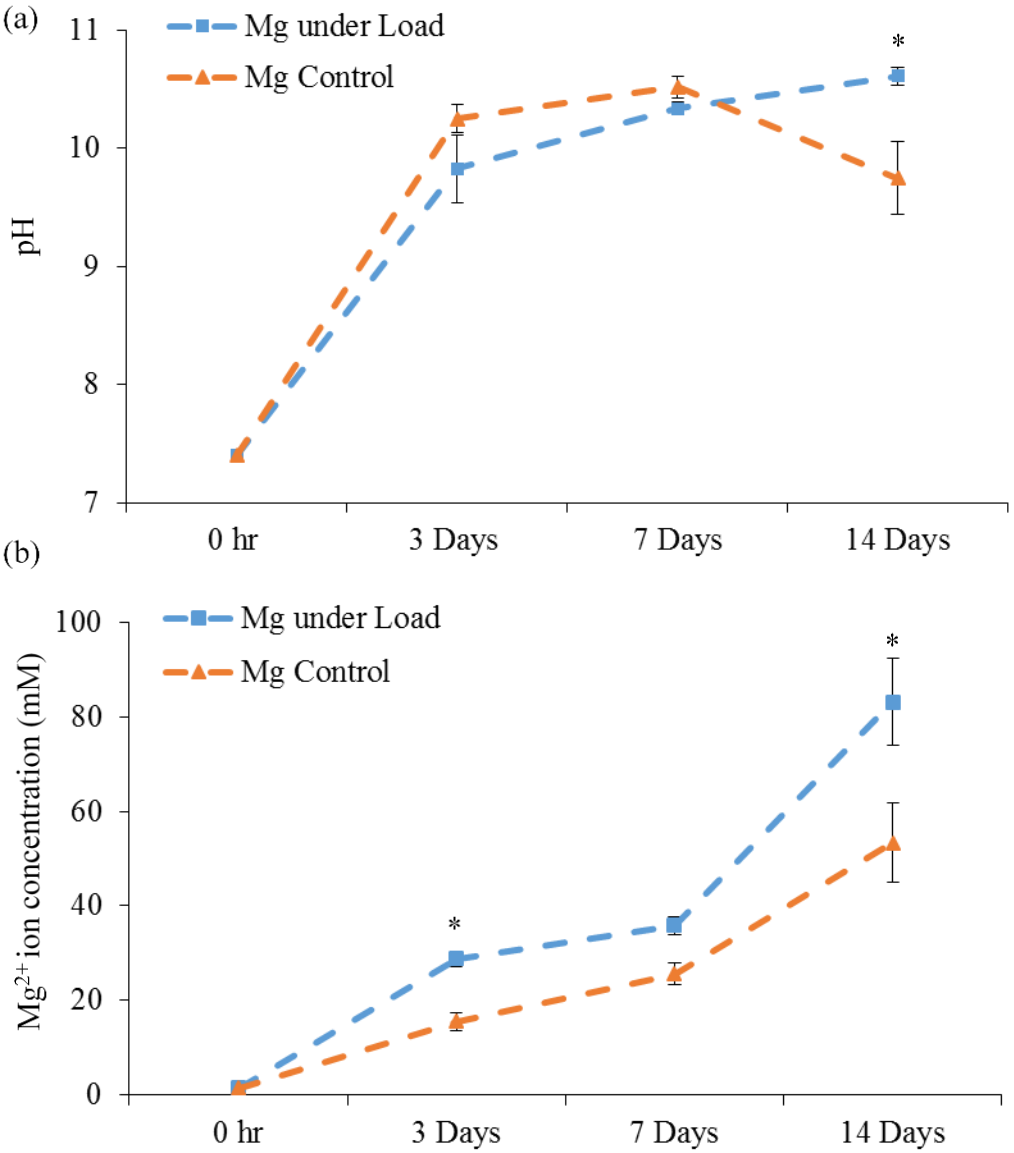

Figure 53 The degradation behaviors of Mg under a compressive load of 500 N comparing to Mg controls during the immersion in rSBF for 14 days. (a) The pH change of rSBF after culture with Mg under load and Mg controls at different time point. (a) The Mg^{2+} ion concentration change of rSBF after culture with Mg under load and Mg controls at different time point. Data are mean ± standard deviation (N=3); *p<0.05.

3.2 Post-media Analysis of the rSBF during Immersion

Figure 53a displays the pH of the rSBF for the Mg under load and Mg controls after 14 days of immersion. Statistically significant difference was found among the Mg-based samples during the 11 days immersion [F(6,17)=10.86], p=0.004. Generally, the pH of Mg-

based samples showed an increase trend as time increased during the immersion. When comparing the Mg under load and Mg controls, the pH of Mg controls was higher than that of Mg under load at 3 days and 7 days immersion. The pH of Mg controls at 14 days, however, showed a lower pH comparing to the previous time point, which was possible because the continuous deposition of degradation products increased the corrosion resistance of Mg samples. At 14 days immersion, the pH of Mg controls was significantly lower than that of Mg under load. The Mg^{2+} ion concentration of the rSBF for the Mg under load and Mg controls showed a significant increase during the 14 days of immersion. Statistically significant difference was found among the Mg-based samples during the 11 days immersion $F(6,17)=55.82]$, $p<0.0001$. The Mg^{2+} ion concentrations of Mg-based samples showed an increase trend as time increased during the immersion. The Mg under load showed a higher Mg^{2+} ion concentration in average than that of Mg controls at all-time points during the immersion. Statistical difference was found at 3 days immersion and 14 days immersion.

4. Discussion

The goal of the loading apparatus is to simulate more realistic body conditions through the use of applying a load onto the medical implant material. Although the device succeeded in its goal, there are still ways of improving the design. Some of these improvements are increasing the accuracy of the load applied onto medical implant material, and downsizing the machine. The current technique of applying a load through compressed air through a pneumatic piston is successful, but the accuracy will vary due to air leaks in the system. The current control system is an open loop and does not contain

any feedback to self-correct the output load. Thus the user must manually read the output values and adjust the air tanks valve accordingly. A solution to this would be the implementation of pistons that are controlled via electrical signals. One piston type of interest would be hydraulic pistons as they are small, and able to output the large forces that would be required for testing various medical implant material. By using these electrical powered pistons, a feedback loop can be created through various means, such as electrical components that read the output force of the electrical powered pistons, and in doing so the machine could self-correct itself to the desired load output without the need of the user. The switch to electrical powered pistons would eliminate the need of the air tank, and greatly decrease the overall size of the machine. After downsizing the machine the next step would be to implement more natural body conditions. One of these additions would be placing the device inside an incubator to simulate the natural body temperature and *in vitro* conditions. However, to achieve this the device must first be small enough to fit inside the incubator, have enough power to last the duration of the study, and be unaffected by the heat from the incubator.

Reference

1. Iskandar, M. E.; Aslani, A.; Tian, Q.; Liu, H., Nanostructured calcium phosphate coatings on magnesium alloys: characterization and cytocompatibility with mesenchymal stem cells. *Journal of materials science. Materials in medicine* **2015,** *26* (5), 189.
2. Witte, F., The history of biodegradable magnesium implants: a review. *Acta biomaterialia* **2010,** *6* (5), 1680-92.
3. Tian, Q.; Liu, H., Electrophoretic deposition and characterization of nanocomposites and nanoparticles on magnesium substrates. *Nanotechnology* **2015,** *26* (17), 175102.
4. Zreiqat, H.; Howlett, C. R.; Zannettino, A.; Evans, P.; Schulze-Tanzil, G.; Knabe, C.; Shakibaei, M., Mechanisms of magnesium-stimulated adhesion of osteoblastic cells to commonly used orthopaedic implants. *J Biomed Mater Res* **2002,** *62* (2), 175-184.
5. Tian, Q.; Deo, M.; Rivera-Castaneda, L.; Liu, H., Cytocompatibility of Magnesium Alloys with Human Urothelial Cells: A Comparison of Three Culture Methodologies. *ACS Biomaterials Science & Engineering* **2016**.
6. Pariente, J. L.; Bordenave, L.; Bareille, R.; Rouais, F.; Courtes, C.; Daude, G.; le Guillou, M.; Baquey, C., First use of cultured human urothelial cells for biocompatibility assessment: Application to urinary catheters. *J Biomed Mater Res* **1998,** *40* (1), 31-39.
7. Pariente, J. L.; Conort, P., Biomaterials used in contact with the urinary tract for urine drainage: catheters and ureteric stents. *Prog Urol* **2005,** *15* (5), 897-906.
8. Joshi, H. B.; Stainthorpe, A.; MacDonagh, R. P.; Keeley, F. X., Jr.; Timoney, A. G.; Barry, M. J., Indwelling ureteral stents: evaluation of symptoms, quality of life and utility. *The Journal of urology* **2003,** *169* (3), 1065-9; discussion 1069.
9. Bithelis, G.; Bouropoulos, N.; Liatsikos, E. N.; Perimenis, P.; Koutsoukos, P. G.; Barbalias, G. A., Assessment of encrustations on polyurethane ureteral stents. *J Endourol* **2004,** *18* (6), 550-556.
10. Tenke, P.; Riedl, C. R.; Jones, G. L.; Williams, G. J.; Stickler, D.; Nagy, E., Bacterial biofilm formation on urologic devices and heparin coating as preventive strategy. *International journal of antimicrobial agents* **2004,** *23 Suppl 1*, S67-74.
11. Chew, B. H.; Hadaschik, B. A.; Paterson, R. F.; Lange, D.; Williams, J. C.; Evan, A. P.; Lingeman, J. E.; McAteer, J. A., Biodegradable Ureteral Stents. **2008,** *1049*, 164-172.
12. Chew, B. H.; Lange, D.; Paterson, R. F.; Hendlin, K.; Monga, M.; Clinkscales, K. W.; Shalaby, S. W.; Hadaschik, B. A., Next generation biodegradable ureteral stent in a yucatan pig model. *The Journal of urology* **2010,** *183* (2), 765-71.
13. Petas, A.; Vuopio-Varkila, J.; Siitonen, A.; Valimaa, T.; Talja, M.; Taari, K., Bacterial adherence to self-reinforced polyglycolic acid and self-reinforced polylactic acid 96 urological spiral stents in vitro. *Biomaterials* **1998,** *19* (7-9), 677-681.
14. Witte, F.; Hort, N.; Vogt, C.; Cohen, S.; Kainer, K. U.; Willumeit, R.; Feyerabend, F., Degradable biomaterials based on magnesium corrosion. *Current Opinion in Solid State and Materials Science* **2008,** *12* (5-6), 63-72.
15. Saris, N. E.; Mervaala, E.; Karppanen, H.; Khawaja, J. A.; Lewenstam, A., Magnesium. An update on physiological, clinical and analytical aspects. *Clinica chimica acta; international journal of clinical chemistry* **2000,** *294* (1-2), 1-26.
16. Lock, J. Y.; Wyatt, E.; Upadhyayula, S.; Whall, A.; Nunez, V.; Vullev, V. I.; Liu, H., Degradation and antibacterial properties of magnesium alloys in artificial urine for potential resorbable ureteral stent applications. *Journal of biomedical materials research. Part A* **2014,** *102* (3), 781-92.

17. Robinson, D. A.; Griffith, R. W.; Shechtman, D.; Evans, R. B.; Conzemius, M. G., In vitro antibacterial properties of magnesium metal against Escherichia coli, Pseudomonas aeruginosa and Staphylococcus aureus. *Acta biomaterialia* **2010,** *6* (5), 1869-77.
18. Staiger, M. P.; Pietak, A. M.; Huadmai, J.; Dias, G., Magnesium and its alloys as orthopedic biomaterials: a review. *Biomaterials* **2006,** *27* (9), 1728-34.
19. Johnson, I.; Perchy, D.; Liu, H., In vitro evaluation of the surface effects on magnesium-yttrium alloy degradation and mesenchymal stem cell adhesion. *Journal of biomedical materials research. Part A* **2012,** *100* (2), 477-85.
20. Waizy, H.; Seitz, J. M.; Reifenrath, J.; Weizbauer, A.; Bach, F. W.; Meyer-Lindenberg, A.; Denkena, B.; Windhagen, H., Biodegradable magnesium implants for orthopedic applications. *Journal of Materials Science* **2013,** *48* (1), 39-50.
21. Castiglioni, S.; Cazzaniga, A.; Albisetti, W.; Maier, J. A., Magnesium and osteoporosis: current state of knowledge and future research directions. *Nutrients* **2013,** *5* (8), 3022-33.
22. Iskandar, M. E.; Aslani, A.; Liu, H., The effects of nanostructured hydroxyapatite coating on the biodegradation and cytocompatibility of magnesium implants. *Journal of biomedical materials research. Part A* **2013,** *101* (8), 2340-54.
23. Song, G. L.; Atrens, A., Corrosion mechanisms of magnesium alloys. *Advanced engineering materials* **1999,** (1), 11-33.
24. Song, G., Control of biodegradation of biocompatable magnesium alloys. *Corros Sci* **2007,** *49* (4), 1696-1701.
25. Song, A. A., Understanding Magnesium corrosion. *Adv. Eng. Mat* **2003,** *5* (12), 837-858.
26. Pariente, J. L.; Kim, B. S.; Atala, A., In vitro biocompatibility assessment of naturally derived and synthetic biomaterials using normal human urothelial cells. *J Biomed Mater Res* **2001,** *55* (1), 33-39.
27. Ibrahim, B.; Leveteau, J.; Guiet-Bara, A.; Bara, M., Influence of magnesium salts on the membrane potential of human endothelial placental vessel cells. *Magnes Res* **1995,** *8* (3), 233-6.
28. Knedler, A.; Ham, R. G., Optimized medium for clonal growth of human microvascular endothelial cells with minimal serum. *In Vitro Cell Dev Biol* **1987,** *23* (7), 481-91.
29. Liu, H., The effects of surface and biomolecules on magnesium degradation and mesenchymal stem cell adhesion. *Journal of biomedical materials research. Part A* **2011,** *99* (2), 249-60.
30. Zheng, Y. F.; Gu, X. N.; Witte, F., Biodegradable metals. *Materials Science and Engineering: R: Reports* **2014,** *77*, 1-34.
31. Trimble, V., Crc Handbook of Chemistry and Physics - Weast,Rc. *Scientist* **1987,** *1* (25), 19-19.
32. Sawai, J.; Kojima, H.; Igarashi, H.; Hashimoto, A.; Shoji, S.; Sawaki, T.; Hakoda, A.; Kawada, E.; Kokugan, T.; Shimizu, M., Antibacterial characteristics of magnesium oxide powder. *World Journal of Microbiology and Biotechnology* **2000,** *16* (2), 187-194.
33. Dong, C.; Cairney, J.; Sun, Q.; Maddan, O. L.; He, G.; Deng, Y., Investigation of Mg(OH)2 nanoparticles as an antibacterial agent. *Journal of Nanoparticle Research* **2009,** *12* (6), 2101-2109.
34. Fruhwirth, O.; Herzog, G. W.; Hollerer, I.; Rachetti, A., Dissolution and hydration kinetics of MgO. *Surface Technology* **1985,** *24* (3), 301-317.
35. Mueller, W. D.; de Mele, M. F.; Nascimento, M. L.; Zeddies, M., Degradation of magnesium and its alloys: dependence on the composition of the synthetic biological media. *Journal of biomedical materials research. Part A* **2009,** *90* (2), 487-95.
36. Willumeit, R.; Fischer, J.; Feyerabend, F.; Hort, N.; Bismayer, U.; Heidrich, S.; Mihailova, B., Chemical surface alteration of biodegradable magnesium exposed to corrosion media. *Acta biomaterialia* **2011,** *7* (6), 2704-15.

37. Mejias, J. A.; Berry, A. J.; Refson, K.; Fraser, D. G., The kinetics and mechanism of MgO dissolution. *Chem Phys Lett* **1999,** *314* (5-6), 558-563.
38. Guan, R. G.; Cipriano, A. F.; Zhao, Z. Y.; Lock, J.; Tie, D.; Zhao, T.; Cui, T.; Liu, H., Development and evaluation of a magnesium-zinc-strontium alloy for biomedical applications--alloy processing, microstructure, mechanical properties, and biodegradation. *Mater Sci Eng C Mater Biol Appl* **2013,** *33* (7), 3661-9.
39. Prasad, A. S., Zinc in human health: effect of zinc on immune cells. *Mol Med* **2008,** *14* (5-6), 353-7.
40. Meunier, P. J.; Roux, C.; Seeman, E.; Ortolani, S.; Badurski, J. E.; Spector, T. D.; Cannata, J.; Balogh, A.; Lemmel, E. M.; Pors-Nielsen, S.; Rizzoli, R.; Genant, H. K.; Reginster, J. Y., The effects of strontium ranelate on the risk of vertebral fracture in women with postmenopausal osteoporosis. *N Engl J Med* **2004,** *350* (5), 459-68.
41. Liu, H. N., Biodegradable Metals and Responsive Biosensors for Musculoskeletal Applications. *Nanotechnology Enabled in Situ Sensors for Monitoring Health* **2011**, 115-137.
42. Surgeons, A. A. o. O., The burden of musculoskeletal diseases in the United States: Prevalence, societal and economic cost. *Rosemont, IL* **2008**.
43. Kalfas, I. H., Principles of bone healing. *Neurosurgical focus* **2001,** *10* (4), E1.
44. Palmer, R. H.; Hulse, D. A.; Hyman, W. A.; Palmer, D. R., Principles of bone healing and biomechanics of external skeletal fixation. *The Veterinary clinics of North America. Small animal practice* **1992,** *22* (1), 45-68.
45. Betz, R. R., Limitations of autograft and allograft: new synthetic solutions. *Orthopedics* **2002,** *25* (5), S561.
46. Tian, Q.; Rivera-Castaneda, L.; Liu, H., Optimization of nano-hydroxyapatite/poly (lactic-co-glycolic acid) coatings on magnesium substrates using one-step electrophoretic deposition. *Materials Letters* **2017,** *186*, 12-16.
47. Webster, T. J.; Ahn, E. S., Nanostructured biomaterials for tissue engineering bone. *Advances in biochemical engineering/biotechnology* **2007,** *103*, 275-308.
48. Liu, H. N.; Webster, T. J., Ceramic/polymer nanocomposites with tunable drug delivery capability at specific disease sites. *Journal of Biomedical Materials Research Part A* **2010,** *93A* (3), 1180-1192.
49. Liu, H. N.; Yazici, H.; Ergun, C.; Webster, T. J.; Bermek, H., An in vitro evaluation of the Ca/P ratio for the cytocompatibility of nano-to-micron particulate calcium phosphates for bone regeneration. *Acta biomaterialia* **2008,** *4* (5), 1472-1479.
50. Webster, T. J.; Siegel, R. W.; Bizios, R., Osteoblast adhesion on nanophase ceramics. *Biomaterials* **1999,** *20* (13), 1221-1227.
51. Correia, R. N.; Magalhaes, M. C. F.; Marques, P. A. A. P.; Senos, A. M. R., Wet synthesis and characterization of modified hydroxyapatite powders. *J Mater Sci-Mater M* **1996,** *7* (8), 501-505.
52. Tian, Q. M.; Liu, H. N., Electrophoretic Deposition and Characterization of Biocomposites on Magnesium for Orthopedic Applications. *Advanced Materials Research* **2014,** *922*, 761-766.
53. Johnson, I.; Akari, K.; Liu, H., Nanostructured hydroxyapatite/poly(lactic-co-glycolic acid) composite coating for controlling magnesium degradation in simulated body fluid. *Nanotechnology* **2013,** *24* (37), 375103.
54. Webster, T. J.; Ergun, C.; Doremus, R. H.; Siegel, R. W.; Bizios, R., Enhanced functions of osteoblasts on nanophase ceramics. *Biomaterials* **2000,** *21* (17), 1803-1810.
55. Mobasherpour, I.; Heshajin, M. S.; Kazemzadeh, A.; Zakeri, M., Synthesis of nanocrystalline hydroxyapatite by using precipitation method. *Journal of Alloys and Compounds* **2007,** *430* (1-2), 330-333.

56. Kumar, R.; Prakash, K. H.; Cheang, P.; Khor, K. A., Temperature driven morphological changes of chemically precipitated hydroxyapatite nanoparticles. *Langmuir* **2004,** *20* (13), 5196-5200.
57. Albrektsson, T.; Johansson, C., Osteoinduction, osteoconduction and osseointegration. *European spine journal : official publication of the European Spine Society, the European Spinal Deformity Society, and the European Section of the Cervical Spine Research Society* **2001,** *10 Suppl 2*, S96-101.
58. Mura-Galelli, M. J.; Voegel, J. C.; Behr, S.; Bres, E. F.; Schaaf, P., Adsorption/desorption of human serum albumin on hydroxyapatite: a critical analysis of the Langmuir model. *Proceedings of the National Academy of Sciences of the United States of America* **1991,** *88* (13), 5557-61.
59. Wassell, D. T. H.; Hall, R. C.; Embery, G., Adsorption of Bovine Serum-Albumin onto Hydroxyapatite. *Biomaterials* **1995,** *16* (9), 697-702.
60. Woo, K. M.; Seo, J.; Zhang, R.; Ma, P. X., Suppression of apoptosis by enhanced protein adsorption on polymer/hydroxyapatite composite scaffolds. *Biomaterials* **2007,** *28* (16), 2622-30.
61. Shi, Z.; Huang, X.; Cai, Y.; Tang, R.; Yang, D., Size effect of hydroxyapatite nanoparticles on proliferation and apoptosis of osteoblast-like cells. *Acta biomaterialia* **2009,** *5* (1), 338-45.
62. Liu, Y.; Wang, G.; Cai, Y.; Ji, H.; Zhou, G.; Zhao, X.; Tang, R.; Zhang, M., In vitro effects of nanophase hydroxyapatite particles on proliferation and osteogenic differentiation of bone marrow-derived mesenchymal stem cells. *Journal of biomedical materials research. Part A* **2009,** *90* (4), 1083-91.
63. Guo, X.; Gough, J. E.; Xiao, P.; Liu, J.; Shen, Z., Fabrication of nanostructured hydroxyapatite and analysis of human osteoblastic cellular response. *Journal of biomedical materials research. Part A* **2007,** *82* (4), 1022-32.
64. Cai, Y.; Liu, Y.; Yan, W.; Hu, Q.; Tao, J.; Zhang, M.; Shi, Z.; Tang, R., Role of hydroxyapatite nanoparticle size in bone cell proliferation. *Journal of Materials Chemistry* **2007,** *17* (36), 3780.
65. Zhao, X.; Ng, S.; Heng, B. C.; Guo, J.; Ma, L.; Tan, T. T.; Ng, K. W.; Loo, S. C., Cytotoxicity of hydroxyapatite nanoparticles is shape and cell dependent. *Archives of toxicology* **2013,** *87* (6), 1037-52.
66. Zhao, Y.; Zhang, Y.; Ning, F.; Guo, D.; Xu, Z., Synthesis and cellular biocompatibility of two kinds of HAP with different nanocrystal morphology. *Journal of biomedical materials research. Part B, Applied biomaterials* **2007,** *83* (1), 121-6.
67. Liu, H.; Webster, T. J., Ceramic/polymer nanocomposites with tunable drug delivery capability at specific disease sites. *Journal of Biomedical Materials Research Part A* **2010,** *93* (3), 1180-1192.
68. Liu, H.; Yazici, H.; Ergun, C.; Webster, T. J.; Bermek, H., An in vitro evaluation of the Ca/P ratio for the cytocompatibility of nano-to-micron particulate calcium phosphates for bone regeneration. *Acta biomaterialia* **2008,** *4* (5), 1472-9.
69. Wang, H.; Li, Y.; Zuo, Y.; Li, J.; Ma, S.; Cheng, L., Biocompatibility and osteogenesis of biomimetic nano-hydroxyapatite/polyamide composite scaffolds for bone tissue engineering. *Biomaterials* **2007,** *28* (22), 3338-3348.
70. Fu, Q.; Rahaman, M. N.; Dogan, F.; Bal, B. S., Freeze-cast hydroxyapatite scaffolds for bone tissue engineering applications. *Biomedical materials* **2008,** *3* (2), 025005.
71. Jun, I.-K.; Song, J.-H.; Choi, W.-Y.; Koh, Y.-H.; Kim, H.-E.; Kim, H.-W., Porous Hydroxyapatite Scaffolds Coated With Bioactive Apatite-Wollastonite Glass-Ceramics. *J Am Ceram Soc* **2007,** *90* (9), 2703-2708.

72. Poinern, G. E.; Brundavanam, R. K.; Mondinos, N.; Jiang, Z. T., Synthesis and characterisation of nanohydroxyapatite using an ultrasound assisted method. *Ultrasonics sonochemistry* **2009,** *16* (4), 469-74.
73. Shi, Z. L.; Huang, X.; Cai, Y. R.; Tang, R. K.; Yang, D. S., Size effect of hydroxyapatite nanoparticles on proliferation and apoptosis of osteoblast-like cells. *Acta biomaterialia* **2009,** *5* (1), 338-345.
74. Liu, Y. K.; Wang, G. C.; Cai, Y. R.; Ji, H. J.; Zhou, G. S.; Zhao, X. L.; Tang, R. K.; Zhang, M., In vitro effects of nanophase hydroxyapatite particles on proliferation and osteogenic differentiation of bone marrow-derived mesenchymal stem cells. *Journal of Biomedical Materials Research Part A* **2009,** *90A* (4), 1083-1091.
75. Zhou, H.; Lee, J., Nanoscale hydroxyapatite particles for bone tissue engineering. *Acta biomaterialia* **2011,** *7* (7), 2769-81.
76. Zheng, X. B.; Huang, M. H.; Ding, C. X., Bond strength of plasma-sprayed hydroxyapatite/Ti composite coatings. *Biomaterials* **2000,** *21* (8), 841-849.
77. Lock, J.; Nguyen, T. Y.; Liu, H. N., Nanophase hydroxyapatite and poly(lactide-co-glycolide) composites promote human mesenchymal stem cell adhesion and osteogenic differentiation in vitro. *J Mater Sci-Mater M* **2012,** *23* (10), 2543-2552.
78. Tian, Q.; Rivera-Castaneda, L.; Dunn, Z. S.; Liu, H., Bioceramics for Orthopaedic Device Applications: Hydroxyapatite. In *Nanobioceramics for Healthcare Applications*, 2017; pp 49-77.
79. Zhang, S., *Hydroxyapatite Coatings for Biomedical Applications*. CRC Press: 2013.
80. Iqbal, N.; Nazir, R.; Asif, A.; Chaudhry, A. A.; Akram, M.; Fan, G. Y.; Akram, A.; Amin, R.; Park, S. H.; Hussain, R., Electrophoretic deposition of PVA coated hydroxyapatite on 316L stainless steel. *Current Applied Physics* **2012,** *12* (3), 755-759.
81. Vijayaraghavan, T. V.; Bensalem, A., Electrodeposition of apatite coating on pure titanium and titanium alloys. *J Mater Sci Lett* **1994,** *13* (24), 1782-1785.
82. Gentile, P.; Chiono, V.; Carmagnola, I.; Hatton, P. V., An Overview of Poly(lactic-co-glycolic) Acid (PLGA)-Based Biomaterials for Bone Tissue Engineering. *Int J Mol Sci* **2014,** *15* (3), 3640-3659.
83. Johnson, I.; Tian, Q.; Liu, H. In *Nanostructured ceramic and ceramic-polymer composites as dual functional interface for bioresorbable metallic implants*, MRS Proceedings, Cambridge University Press: 2014; pp 39-45.
84. Lock, J.; Nguyen, T. Y.; Liu, H., Nanophase hydroxyapatite and poly(lactide-co-glycolide) composites promote human mesenchymal stem cell adhesion and osteogenic differentiation in vitro. *Journal of materials science. Materials in medicine* **2012,** *23* (10), 2543-52.
85. Shen, H.; Hu, X.; Yang, F.; Bei, J.; Wang, S., An injectable scaffold: rhBMP-2-loaded poly(lactide-co-glycolide)/hydroxyapatite composite microspheres. *Acta biomaterialia* **2010,** *6* (2), 455-65.
86. Liu, H.; Webster, T. J., Mechanical properties of dispersed ceramic nanoparticles in polymer composites for orthopedic applications. *International journal of nanomedicine* **2010,** *5*, 299.
87. Jevtic, M.; Radulovic, A.; Ignjatovic, N.; Mitric, M.; Uskokovic, D., Controlled assembly of poly(D,L-lactide-co-glycolide)/hydroxyapatite core-shell nanospheres under ultrasonic irradiation. *Acta biomaterialia* **2009,** *5* (1), 208-18.
88. Everett, D. H.; Stageman, J. F., Preparation and stability of novel polymer colloids in a range of simple liquids. *Faraday Discussions of the Chemical Society* **1978,** *65*, 230.
89. Besra, L.; Liu, M., A review on fundamentals and applications of electrophoretic deposition (EPD). *Progress in Materials Science* **2007,** *52* (1), 1-61.

90. N, P. S. P. S., Electrophoretic deposition: Mechanisms, Kinetics and Application to ceamics. *J. Am. Ceram. Soc,* **1996,** *79* (8), 1987-2002.
91. Boccaccini, A. R.; Keim, S.; Ma, R.; Li, Y.; Zhitomirsky, I., Electrophoretic deposition of biomaterials. *Journal of the Royal Society, Interface / the Royal Society* **2010,** *7 Suppl 5*, S581-613.
92. Zongtao Z, M. F. D., T.D. Xiao, Nanostructured Hydroxyapatite coatings for improved adhesion and corrosion resistance for medical implants. *Mat. Res. Soc. Symp* **2002,** *703*.
93. Han, Y., Fu, T., Lu, J. and Xu, K, Characterization and stability of hydroxyapatite coatings prepared by an electrodeposition and alkaline-treatment process. *J. Biomed. Mater. Res.,* **2001,** *54* (1), 96–101.
94. Sato, N.; Kawachi, M.; Noto, K.; Yoshimoto, N.; Yoshizawa, M., Effect of particle size reduction on crack formation in electrophoretically deposited YBCO films. *Physica C: Superconductivity* **2001,** *357–360, Part 2* (0), 1019-1022.
95. Gonghou Wang, P. S., and Patrick S. Nicholson, Surface Chemistry and Rheology of Electrostatically (Ionically) Stabilized Alumina Suspensions in Polar Organic Media. *J. Am. Ceram. Soc,* **2004,** *82* (4), 849-856.
96. Uchikoshi, T.; Ozawa, K.; Hatton, B. D.; Sakka, Y., Dense, bubble-free ceramic deposits from aqueous suspensions by electrophoretic deposition. *Journal of Materials Research* **2001,** *16* (02), 321-324.
97. Shirazi, R. N.; Aldabbagh, F.; Erxleben, A.; Rochev, Y.; McHugh, P., Nanomechanical properties of poly(lactic-co-glycolic) acid film during degradation. *Acta biomaterialia* **2014,** *10* (11), 4695-703.
98. Kaya, C., Electrophoretic deposition of carbon nanotube-reinforced hydroxyapatite bioactive layers on Ti–6Al–4V alloys for biomedical applications. *Ceramics International* **2008,** *34* (8), 1843-1847.
99. Duan, B.; Yuan, X.; Zhu, Y.; Zhang, Y.; Li, X.; Zhang, Y.; Yao, K., A nanofibrous composite membrane of PLGA–chitosan/PVA prepared by electrospinning. *European Polymer Journal* **2006,** *42* (9), 2013-2022.
100. Mohan, L.; Durgalakshmi, D.; Geetha, M.; Sankara Narayanan, T. S. N.; Asokamani, R., Electrophoretic deposition of nanocomposite (HAp+TiO2) on titanium alloy for biomedical applications. *Ceramics International* **2012,** *38* (4), 3435-3443.
101. Johnson, I.; Liu, H. N., A Study on Factors Affecting the Degradation of Magnesium and a Magnesium-Yttrium Alloy for Biomedical Applications. *Plos One* **2013,** *8* (6).
102. Cipriano, A. F.; Sallee, A.; Guan, R. G.; Zhao, Z. Y.; Tayoba, M.; Sanchez, J.; Liu, H., Investigation of magnesium-zinc-calcium alloys and bone marrow derived mesenchymal stem cell response in direct culture. *Acta biomaterialia* **2015,** *12*, 298-321.
103. Wang, J.; Witte, F.; Xi, T.; Zheng, Y.; Yang, K.; Yang, Y.; Zhao, D.; Meng, J.; Li, Y.; Li, W.; Chan, K.; Qin, L., Recommendation for modifying current cytotoxicity testing standards for biodegradable magnesium-based materials. *Acta biomaterialia* **2015,** *21*, 237-49.
104. Jung, O.; Smeets, R.; Porchetta, D.; Kopp, A.; Ptock, C.; Muller, U.; Heiland, M.; Schwade, M.; Behr, B.; Kroger, N.; Kluwe, L.; Hanken, H.; Hartjen, P., Optimized in vitro procedure for assessing the cytocompatibility of magnesium-based biomaterials. *Acta biomaterialia* **2015,** *23*, 354-63.
105. Li, L.; Gao, J.; Wang, Y., Evaluation of cyto-toxicity and corrosion behavior of alkali-heat-treated magnesium in simulated body fluid. *Surface and Coatings Technology* **2004,** *185* (1), 92-98.
106. Hanzi, A. C.; Gunde, P.; Schinhammer, M.; Uggowitzer, P. J., On the biodegradation performance of an Mg-Y-RE alloy with various surface conditions in simulated body fluid. *Acta biomaterialia* **2009,** *5* (1), 162-71.

107. Song, G.; Atrens, A.; Dargusch, M., Influence of microstructure on the corrosion of diecast AZ91D. *Corros Sci* **1998,** *41* (2), 249-273.
108. Cheng, Y.-l.; Qin, T.-w.; Wang, H.-m.; Zhang, Z., Comparison of corrosion behaviors of AZ31, AZ91, AM60 and ZK60 magnesium alloys. *Transactions of Nonferrous Metals Society of China* **2009,** *19* (3), 517-524.